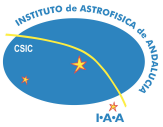

UNIVERSIDAD DE GRANADA

Tesis doctoral

Octubre 2016

From circumstellar disks to planetary systems: Observation and modeling of protoplanetary disks

[PhD THESIS]

Enrique Macías Quevedo

Instituto de Astrofísica de Andalucía (CSIC)

Memoria de Tesis

presentada en la Universidad de Granada

para optar al grado de Doctor en Física

Directores de tesis:

Guillem Anglada Pons

Mayra Carolina Osorio Gutiérrez

Editor: Universidad de Granada. Tesis Doctorales
Autor: Enrique Macías Quevedo
ISBN: 978-84-9163-030-2
URI: http://hdl.handle.net/10481/44570

La demencia, la madre de la ciencia.

La Demencia,
afición del C. B. Estudiantes

Agradecimientos

La finalización de esta tesis es en realidad la culminación de un largo trayecto. Es difícil marcar el inicio y fácil olvidarse de toda la gente que ha contribuido, por poco que sea, para que esta tesis pueda ser hoy una realidad. A todas estas personas quiero darles las gracias.

A Guillem y Mayra, por introducirme en el mundo de la astrofísica y confiar en mí cuando solo era un estudiante de verano en el IAA. Gracias por todos los conocimientos que me habéis aportado durante estos años. Moltes gràcies Guillem. Muchas gracias Mayra.

A todas las personas que me han ido acogiendo y divulgando parte de su conocimiento. Muchas gracias en particular a Carlos Carrasco, Itziar de Gregorio, Susana Lizano, Nuria Calvet y José Francisco Gómez. Lo que sé hoy es en gran parte también gracias a vosotros. A Paola D'Alessio, que a pesar de no estar entre nosotros, ha contribuido enormemente a que esta tesis sea lo que es.

A la gente que he ido conociendo durante estos años y que harán que me lleve unos grandes recuerdos de esta época. A Roberto Galván y Josep Maria Masqué, muchas gracias por acogerme durante mis viajes. A los IFIs y no tan IFIs del IAA, que son muchos y no caben, y a todo el IAA en general. A mis compañeros de despacho, Juanma y Ana Karla, gracias por compartir tantos momentos, deadlines, pizzas, dardos... A los *Brazos fantasía*, por sacarme de paseo de vez en cuando. A Sandra y Jesús, por tantos buenos momentos, risas, vídeos y tantas tantas geniales estupideces. Y a la gente que ya conocía pero que también han contribuido desde la distancia a que haya podido disfrutar estos 4 años. Gràcies *Friends*, no canvieu mai.

A Natalia, por no dejarme volverme loco estos últimos meses, por hacerlo todo más fácil, por los paralelogramas, y en definitiva por ser como eres.

A mi hermana, por marcarme el camino siendo la primera doctora Macías. A mi hermano, por no dejarme ser el único, y porque pase lo que pase "todo es culpa de papá". Y sobretodo a mis padres, por estar siempre ahí, por hacerme la persona que soy hoy, y por confiar en mí más que nadie.

Resumen

En esta tesis se presentan los resultados de un estudio con alta resolución angular de las primeras etapas de formación planetaria en discos de acreción en torno a estrellas jóvenes. Reportamos observaciones en longitudes de onda milimétricas y centimétricas de tres discos de transición alrededor de estrellas con masas entre ~ 0.4 y $\sim 2\ M_{\odot}$ y edades entre ~ 1 y ~ 10 millones de años. Estas observaciones, obtenidas con los radiointerferómetros Very Large Array (VLA) y Atacama Large Millimeter/Submillimeter Array (ALMA), nos han permitido estudiar la emisión térmica de los granos de polvo de mayor tamaño, así como la emisión libre-libre emitida por gas ionizado en el disco y sus alrededores. Además, hemos complementado estas observaciones con la modelización de la emisión térmica de polvo utilizando para ello códigos de transporte radiativo para discos de acreción irradiados por una estrella central, que calculan de manera autoconsistente su distribución de temperatura y densidad, así como la emisión resultante.

En primer lugar presentamos un estudio del disco en torno a la estrella de masa intermedia HD 169142. Hemos llevado a cabo observaciones con el VLA a 7 mm, 9 mm y 3 cm, las cuales trazan la emisión térmica de los granos de polvo de tamaño milimétrico y centimétrico en el disco protoplanetario, así como la emisión libre-libre de gas ionizado. Nuestras imágenes muestran un sistema de al menos tres huecos anulares en el disco de polvo, cada uno con un ancho de $\sim 0\farcs20$ (~ 30 ua a 145 pc), con radios externos de $\sim 0\farcs20$, $\sim 0\farcs48$, y $\sim 0\farcs83$ (~ 30, ~ 70, y ~ 120 ua, respectivamente). Además, detectamos un anillo de emisión brillante y grumoso con un radio de ~ 32 ua y un ancho de ~ 15 ua. Interpretamos que este anillo está trazando el borde de la cavidad interna del disco. Al contrario que en otros casos, los radios de esta estructura de anillos y huecos anulares detectados a 7 y 9 mm son similares a los radios observados en imágenes de luz polarizada en el infrarrojo cercano, las cuales trazan la luz dispersada por los granos de polvo pequeños (tamaños de micras). Asimismo, modelamos la distribución espectral de energía y las imágenes a 7 mm para restringir la estructura física del disco. A partir de este modelaje inferimos la presencia de un pequeño disco residual (con un radio de ~ 0.6 ua) dentro de la cavidad central, indicando que el disco alrededor de HD 169142 es en realidad un disco de pretransición.

El anillo de emisión en el disco de HD 169142 presenta un alto grado de subestructura, posiblemente producida por interacciones dinámicas entre el disco y múltiples planetas en formación. Especulamos que la acumulación de material debida a estas interacciones podría haber vuelto el anillo gravitacionalmente inestable, fragmentándose en grumos de material que podrían acabar formando nuevos planetas. Basándonos en los resultados de nuestras observaciones y modelo, sugerimos que los dos huecos anulares en el disco de HD 169142 más cercanos a la estrella central podrían haber sido creados por la interacción dinámica entre el disco y planetas en formación, mientras que el hueco anular más externo y poco profundo podría estar asociado con el crecimiento de los granos de polvo y su acumulación cerca del frente de condensación de la molécula de CO.

Nuestras observaciones de HD 169142 con mayor resolución angular también nos han permitido detectar una componente de emisión a 7 mm y 9 mm dentro del hueco más interno, con su pico de emisión a una distancia proyectada de $\sim$ 4 ua hacia el oeste de la estrella central. Su densidad de flujo e índice espectral indican que la mayor parte de la emisión es producida por gas ionizado, el cual podría estar asociado con una fotoionización inhomogénea del disco interno, con un objeto independiente, o con un jet ionizado. Favorecemos este último escenario y especulamos que este jet podría estar significativamente fotoionizado por la radiación de altas energías emitida por la estrella central.

Por otro lado, reportamos el descubrimiento de un disco protoplanetario enano alrededor de la estrella XZ Tau B que muestra todas las características de un disco de transición clásico pero a una escala de tamaño mucho menor. El disco ha sido observado con ALMA con una resolución angular extremadamente alta a longitudes de onda milimétricas. Mientras que el radio de los discos de transición clásicos está en torno a $\sim$ 100 ua, el disco alrededor de XZ Tau B presenta un radio de tan solo $\sim$ 3.4 ua, con una cavidad central de $\sim$ 1.3 ua de radio. Hemos modelado la emisión de polvo del disco y hemos demostrado que su masa es probablemente lo suficientemente alta como para formar un sistema planetario compacto como los detectados en las observaciones de exoplanetas. Debido al pequeño tamaño del disco, su evolución dinámica se espera que sea mucho más rápida que en los discos clásicos. Esto abre la posibilidad de poder seguir observando la evolución del sistema en escalas de tiempo muy cortas (del orden de meses).

Finalmente, hemos llevado a cabo observaciones del disco de transición de GM Aur utilizando varias configuraciones del VLA a 7 mm, 3 cm y 5 cm. Nuestras observaciones nos han permitido obtener imágenes y separar, por primera vez, los componentes principales de los discos en este estado evolutivo: el disco de polvo, el radiojet ionizado perpendicular a este y el viento de fotoevaporación originado en la superficie del disco. La tasa de pérdida de masa estimada a partir de la densidad de flujo a 3 cm del radiojet es consistente con la razón entre tasas de eyección y acreción de material típicamente encontradas en objetos más jóvenes ($\sim 10\%$), lo cual sugiere que los discos de transición son capaces de producir eyecciones colimadas de material siguiendo, aparentemente, los mismos procesos físicos que las protoestrellas más jóvenes. Nuestros resultados indican que la radiación en el ultravioleta extremo (EUV; 13.6–100 eV) es el mecanismo de ionización principal del viento de fotoevaporación trazado por la emisión libre-libre observada a longitudes de onda centimétricas. La tasa de fotones EUV inferida a partir de esta emisión sería insuficiente para producir la tasas de pérdida de masa necesaria para dispersar el disco en la escala de tiempo impuesta por las observacoines ($\lesssim$ 10 millones de años). Por lo tanto, concluimos que otros mecanismos adicionales, como la fotoevaporación por rayos X (la cual puede producir un viento más denso pero solo parcialmente ionizado), serán necesarios.

Summary

In this thesis we present the results of a high angular resolution study of the first stages of planetary formation in circumstellar accretion disks around young stars. We report mm and cm observations toward three different transitional disks around stars with masses between ~ 0.4 and ~ 2 $M_{\odot}$ and ages between ~ 1 and ~ 10 Myr. These observations, obtained with the Very Large Array (VLA) and the Atacama Large Millimeter/Submillimeter Array (ALMA), have allowed us to study the thermal continuum emission of the large dust grains as well as the free-free emission from ionized gas in the disk and its surroundings. In addition, we have complemented these observations with the modeling of the dust thermal emission using self-consistent radiative transfer codes for accretion disks irradiated by its central star that calculate their temperature and density distribution, as well as the predicted dust emission.

In the first place, we present a study of the disk around the intermediate-mass star HD 169142. We report VLA observations at 7 mm, 9 mm, and 3 cm that trace the thermal emission of large dust grains (mm-cm sized) in the protoplanetary disk and the free-free emission of ionized gas. Our images have revealed the presence of a system of at least three gaps in the disk of dust, each $\sim 0\farcs20$ in width (~ 30 au at 145 pc), with outer radii of $\sim 0\farcs20$, $\sim 0\farcs48$, and $\sim 0\farcs83$ (~ 30, ~ 70, and ~ 120 au, respectively). A bright and narrow clumpy ring of enhanced emission is observed at a radius of $\sim$32 au, with a width of ~ 15 au. We interpret this ring to be tracing the rim of the inner gap. Unlike other sources, the radii of this structure of rings and gaps detected at 7 and 9 mm coincide with those obtained from previous near-infrared polarimetric images, which trace scattered light from small (micron sized) dust grains. We model the broad-band spectral energy distribution and the 7 mm images to constrain the disk physical structure. From this modeling we infer the presence of a small residual disk (~ 0.6 au in radius) inside the central cavity, indicating that the HD 169142 disk is a pre-transitional disk.

The emission ring of the HD 169142 disk presents a high degree of substructure, which could be produced by dynamical interactions between the disk and multiple forming planets. We speculate that the ring could have become gravitationally unstable due to a pile-up of material produced by this dynamical interaction. As a consequence, the ring might be fragmenting into clumps that would end up forming

new planets. Based on our observational and modeling results, we suggest that the two closest and most prominent gaps in the disk of HD 169142 could be created by dynamical interactions between the disk and forming planets, while the outer and shallower gap might be associated with dust growth and trapping close to the CO molecule snowline.

Our highest angular resolution observations toward HD 169142 have also allowed us to detect a component of emission at 7 mm and 9 mm inside the innermost gap, with its peak of emission located at a projected distance of $\sim$ 4 au toward the west from the central star. Its flux density and spectral index indicate that most of its emission is produced by ionized gas, which could be associated with an inhomogeneous photoionization of the inner disk, with an independent object, or with an (asymmetric) ionized jet. We favor the latter scenario and speculate that this jet might be significantly photoionized by the high energy radiation emitted from the central star.

On the other hand, we report the discovery of a dwarf protoplanetary disk around the star XZ Tau B that shows all the features of a classical transitional disk but on a much smaller scale. The disk has been imaged with ALMA with extremely high angular resolution at mm wavelengths. While classical transitional disks have radii of $\sim$ 100 au, the disk around XZ Tau B presents a radius of only $\sim$3.4 au, with a central cavity of $\sim$1.3 au in radius. We have modeled the dust emission of the disk, showing that the mass of the disk could be large enough to form a compact planetary system like the ones detected in the exoplanet surveys. Due to the very small size of the disk, the dynamical evolution of the system is expected to be much faster than in classical larger disks. This opens up the possibility of monitoring the evolution of the system in very short (a few months) timescales.

Finally, we performed multi-configuration VLA observations at 7 mm, 3 cm, and 5 cm toward the transitional disk of GM Aur. Our radio continuum observations have allowed us to image and spatially resolve, for the first time, the three main components at work in this stage of the disk evolution: the disk of dust, the ionized radio jet perpendicular to it, and the photoevaporative wind arising from the disk. The mass loss rate inferred from the flux density of the radio jet at 3 cm is consistent with the ratio between ejection and accretion rates typically found in younger objects ($\sim$ 10%), suggesting that transitional disks can power collimated ejections of material

apparently following the same physical mechanisms as much younger protostars. Our results indicate that extreme-UV (EUV; 13.6–100 eV) radiation is the main ionizing mechanism of the photoevaporative wind traced by the free-free emission observed at cm wavelengths. The EUV photon luminosity inferred from this free-free emission is too low to produce the mass loss rates needed to disperse the disk in the timescales imposed by observations ($\lesssim$ 10 Myr). Therefore, we conclude that other additional mechanisms, such as X-ray-driven photoevaporation (which can launch a denser but only partially ionized wind), are required.

Index

1

Introduction

With nearly 3500 exoplanets discovered, and almost 5000 more candidates identified, planetary systems are now known to be ubiquitous around low-mass stars. The possible existence of exoplanetary systems was anticipated by the study of the star-formation process. Over the 1980's, a broad consensus was reached on the fact that circumstellar accretion disks are the likely progenitors of planetary systems, and that these disks form naturally and quite commonly during the early phases of stellar evolution (e.g., Strom 1985; Anglada 1989). The presence of circumstellar material was initially inferred from the observation of infrared excesses attributed to thermal emission of warm dust (Mendoza 1966; Cohen & Kuhi 1979) and from more detailed analysis of the observed spectral energy distributions (SEDs) of young stars (Kenyon & Hartmann 1987; Strom et al. 1989). Radio observations aimed to search for the origin of collimated bipolar outflows (Torrelles et al. 1983) revealed compact, unresolved structures around young stellar objects (YSOs), both in molecular transitions and in the millimeter continuum, that were interpreted as unresolved circumstellar disks of gas and dust (Sargent & Beckwith 1991; Rodríguez et al. 1992; Lizano & Torrelles 1995 and references therein). Later on, the Hubble Space Telescope (HST) provided silhouette images that spatially resolved the shape of these disks (Burrows et al. 1996). Additionally, more sensitive mm and submm interferometers, such as the Submillimeter Array (SMA) and CARMA, started to produce resolved images of these disks (Andrews et al. 2011; Isella, Pérez & Carpenter 2012). Finally, the advent

of the Atacama Large Millimeter/submillimeter Array (ALMA) and the Jansky Very Large Array (JVLA) observatories has been recently producing an increasing sample of detailed images of these disks that start to reveal the details of the planetary formation process (ALMA Partnership et al. 2015a; Carrasco-González et al. 2016).

Nowadays it has become clear that the formation of planetary systems takes place during the stellar formation itself, from the dust and gas orbiting around the star in the protoplanetary disks. However, the process that leads to this formation is still not well understood. Studying the physical and chemical conditions of circumstellar disks is, thus, key to understand the planetary formation process.

Circumstellar accretion disks are formed during the first stages of star formation. Even though rotating disks have been detected around massive stars ($M_\star \gtrsim 8\ M_\odot$; Patel et al. 2005; Carrasco-González et al. 2012), it seems unlikely that planetary systems can survive the extreme conditions around this type of stars. We will focus here on protoplanetary disks around low-mass stars, which are the precursors of planetary systems.

1.1 Low-mass star formation

Interstellar molecular clouds, which are composed of gas and dust, can fragment and collapse, forming a dense central object or protostar surrounded by an infalling envelope. Due to the conservation of angular momentum, a slight initial rotation of the cloud results in a rotating flattened envelope near the central object. Because of this rotation, the collapsing material will not fall directly onto the star, but will form a rotating disk in the equatorial plane. Throughout the evolution of the protostar, the envelope and the disk will become more tenuous, resulting eventually in the formation of a planetary system surrounding a main-sequence star. During this evolution, the emission from optical to mm wavelengths of the young stellar object (YSO) will change significantly. From the slope of their spectral energy distribution (SED) between ~ 2 μm and 10-25 μm ($\alpha_{\rm IR} = d\log(\lambda F_\lambda)/d\log\lambda$), low-mass YSOs have been classified in four different classes that correspond to four different evolutionary states (see Fig. 1.1; Adams, Lada & Shu 1987; Andre, Ward-Thompson & Barsony 1993):

- **Class 0:** These sources show almost no emission at optical and near-infrarred (near-IR) wavelengths. Their SED resembles a black body at a very low tem-

perature, emitting mainly at far-IR and (sub)mm wavelengths. The emission comes from a cold envelope $\sim 10^4$ au in size surrounding the protostar. This envelope is optically thick at optical and near-IR wavelengths, which difficults the detection of the central protostar at short wavelengths. This stage corresponds to the youngest objects with ages $\lesssim 10^4$ years.

- **Class I:** These sources are characterized by a positive value of $\alpha_{\rm IR}$. The SED of this class of objects is wider than a blackbody, but the emission has moved to shorter wavelengths in comparison to Class 0 YSOs. The emission is still mainly observed at far-IR wavelengths, but with a significant contribution from warmer material that emits at near and mid-IR wavelengths. These YSOs are still embedded in an envelope but are very bright due to the important contribution of the accretion luminosity. A circumstellar accretion disk has already formed around the central protostar. The accretion disk, however, might be significantly influenced and perturbed by the envelope. The age of these objects is between $\sim 10^4$ and $\sim 10^5$ years.

- **Class II:** These sources present negative values of $\alpha_{\rm IR}$, although still showing a slight excess of emission above the expected stellar emission. Their SED is still considerably wider than a blackbody. This indicates that the amount of dust surrounding the central star, which is considered to be in the pre-main sequence (PMS) phase, has decreased significantly. The envelope around these sources is thought to have almost disappeared. Therefore, the dust in the system is now mainly part of a circumstellar protoplanetary disk, which is optically thick at optical, near, and mid-IR wavelengths. During this stage the protoplanetary disk evolves mainly through viscous evolution. The planetary formation process is also thought to start during this phase. The accretion luminosity is now much lower than in previous evolutionary stages, and therefore the main source of energy is now the stellar emission. Except for YSOs with edge-on disks, the central PMS star is now visible at optical wavelengths. The age of these systems ranges approximately between 10^6 and 10^7 years. The extensively studied YSOs known as classical T Tauri stars belong to this class.

- **Class III:** These sources present a very negative value of $\alpha_{\rm IR}$. The shape of their SED is very similar to that of a blackbody at the temperature of the star. The low excess of emission at IR wavelengths corresponds to the circumstellar disk, which is now optically thin to the radiation from the star. Disks in this phase are thought to bear recently formed planets, as well as residual dust pebbles and planetesimals. The amount of gas in the disk is now very small, so the central star is no longer accreting material. The more evolved disks aorund this class of objects, which show almost no gas, are also known as debris disks. The central star in Class III YSOs may still be in the pre-main sequence (e.g. weak-lined T Tauri stars) or may have just entered the main sequence.

During the earliest stages of star formation (Class 0), an accretion-driven collimated ejection of partially ionized material (i.e. a jet) is formed along the rotation axis of the system. The driving mechanism of these ejections of material is not well understood yet, but they are thought to be centrifugally launched at very close distances from the star ($\lesssim 1$ au), and then collimated through magnetic fields (Cabrit 2007). Jets are thought to play a crucial role during the star formation process since they remove the excess of angular momentum from the disk, which in turn allows the material to accrete onto the star. The ionized jets produce thermal free-free radiation, which can be studied at cm wavelengths. Observations of jets in young protostars (Class 0 – Class I objects) indicate that the mass loss rate in the jet is $\sim 10\%$ of the mass accretion rate onto the star (Cabrit 2007). Therefore, jets in more evolved objects (Class II), which present lower mass accretion rates, are expected to be weaker and more difficult to detect. Nevertheless, recent observations have been able to show the presence of radio jets in this lass of objects, which suggests that jets could still have an impact on the planetary formation process (e.g., Rodríguez et al. 2014; Macías et al. 2016; see Chapters 3 and 5).

As mentioned above, planets are thought to form in Class II YSOs (see §1.4). Protoplanetary disks spend most of ther lifetimes in these stages, where they can evolve mainly through viscous evolution (Lynden-Bell & Pringle 1974; Hartmann, Herczeg & Calvet 2016). A kinematic viscosity, which is thought to be produced by magnetohydrodynamic (MHD) turbulence, can drive a constant inward flow of matter toward the inner regions of the disk producing accretion onto the central star.

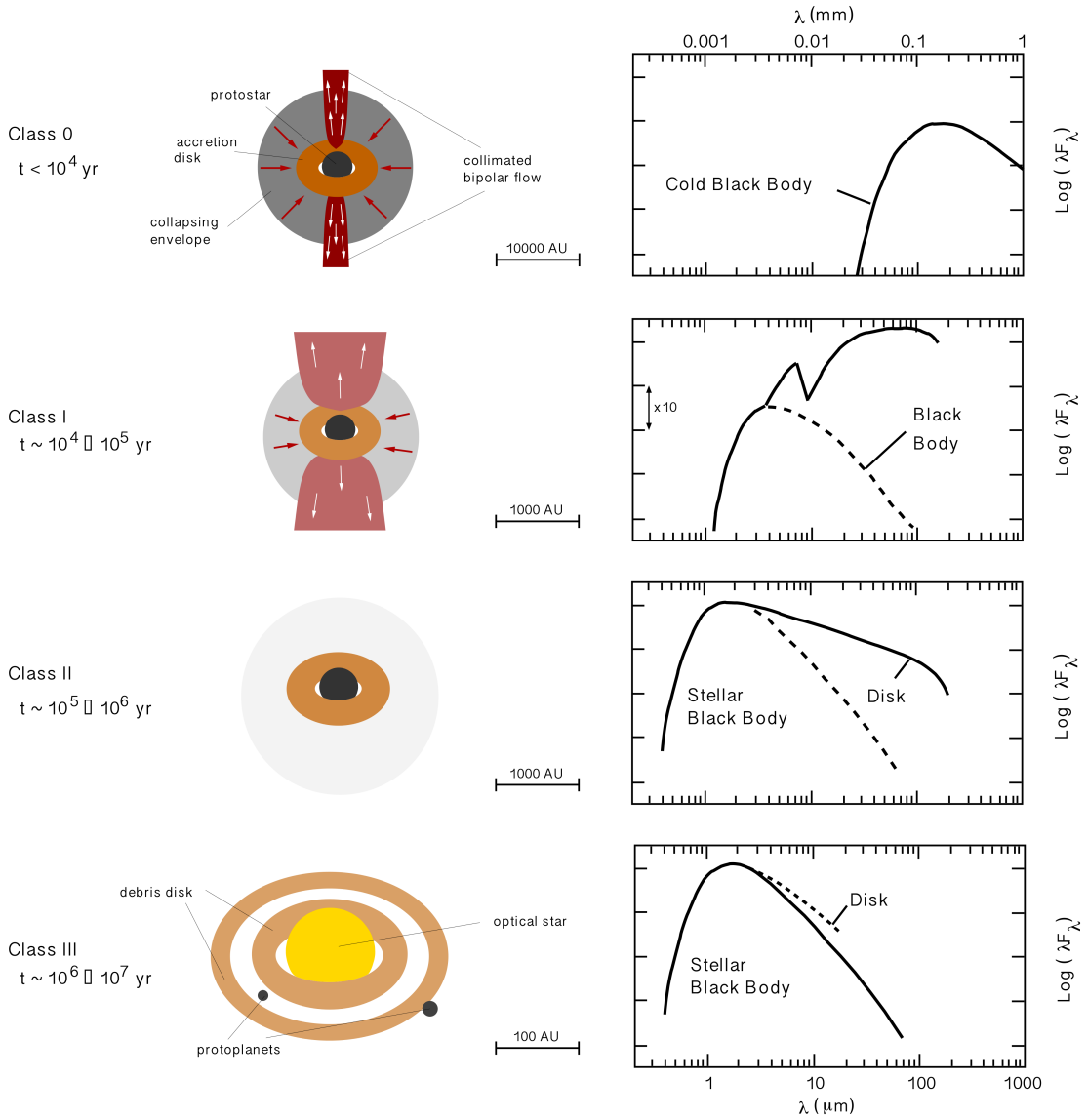

Figure 1.1 Classification of low-mass young stellar objects based on the overall shape of their SEDs. Each class is thought to represent a different evolutionary stage of the YSO, constituting what it is nowadays the standard picture of low-mass star formation.

As the disk evolves, its density and accretion rate steadily decrease. However, other physical processes, such as dust evolution (grain growth, settling, and migration) and photoevaporation, can also play an important role. Determining how these processes affect the evolution of protoplanetary disks will be key to understand the initial conditions and overall process of planetary formation.

1.2 Dust evolution

In the standard scenario for planet formation, or core accretion scenario (e.g. Wuchterl, Guillot & Lissauer 2000), planetary cores are formed through the growth and aggregation of dust grains, from sub-micron sizes to pebbles and even km-sized planetesimals. Observations indicate that dust grains in the interstellar medium have sizes ranging from 0.005 μm to 0.25–1 μm, with a size distribution similar to a power law with an exponent of -3.5 ($n(a) \propto a^{-3.5}$; Mathis, Rumpl & Nordsieck 1977). Models show that dust grains can start growing in cores and protostellar envelopes up to sizes of several microns (Ormel et al. 2009). Nevertheless, grain growth is expected to be much more efficient in protoplanetary disks, where higher densities are found. In addition, IR observations of dust spectral features have also allowed to infer the compositon of dust grains. There is still some uncertainty on the abundance of each component, but dust grains are thought to be composed mainly of different silicates (such as olivine, pyroxene, forsterite and enstatite), amorphous graphites, and water ice (Draine & Lee 1984; McClure et al. 2013).

The opacity of the dust changes significantly as the grains grow in size (D'Alessio 1996). In general, the dust opacity of a particular grain is higher at a wavelength similar to its size. Therefore, mm and cm observations of the dust thermal continuum emission of protoplanetary disks are well suited to trace the emission from the large (mm-cm sized) dust grains in the disk, which could trace the locations of planetesimal formation (Birnstiel, Dullemond & Pinilla 2013). At these wavelengths the disk will probably be optically thin, so one can trace the dust grains in the mid-plane of the disk, where most of the dust is located and planet formation is thought to occur. Furthermore, at these wavelengths the dust opacity of the disk can be approximated as a power law, $\kappa_\nu \propto \nu^\beta$. The slope of the dust opacity, β, depends mainly on the maximum size of the dust grain population, with values $0 < \beta < 1$ for mm–cm grains

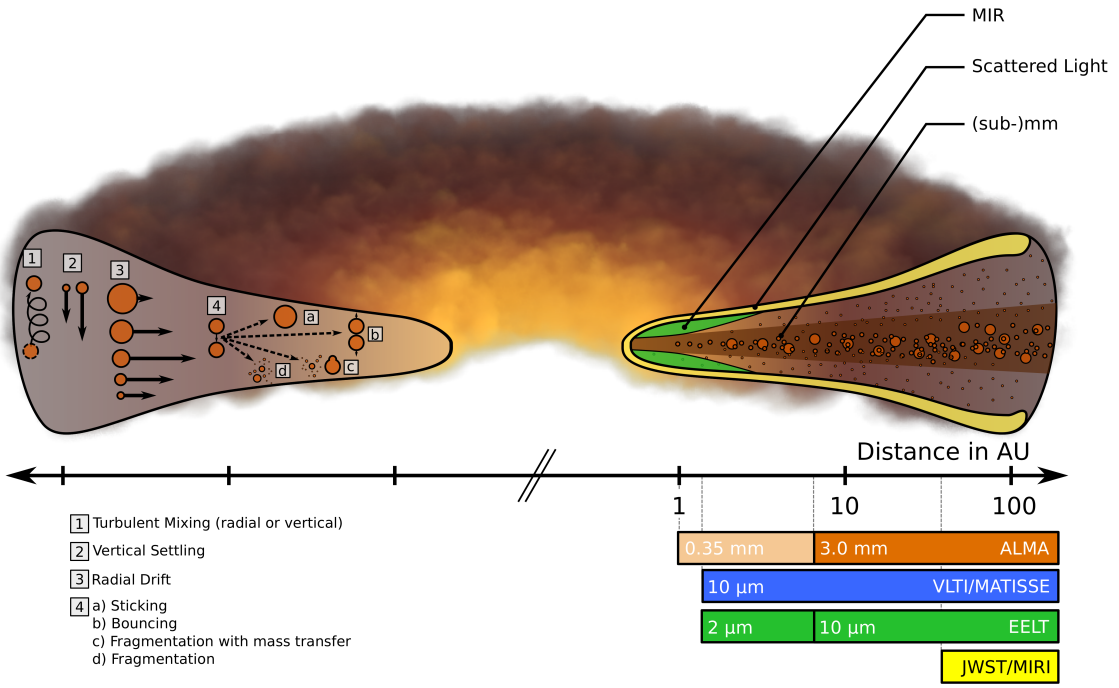

Figure 1.2 Scheme showing the dust grain transport and collision processes in a protoplanetary disk, as well as the regions of the disk to which different observations are sensitive. The horizontal bars on the bottom right indicate the angular resolution that can be achieved with different new or upcoming observatories at different wavelengths, assuming a typical distance for the closest star forming regions. Figure from Testi et al. (2014).

and steeper slopes for smaller grains (Miyake & Nakagawa 1993; Draine 2006). The spectral index of the dust emission will be $2 + \beta$, so by measuring the spectral index from mm and cm observations one can study the size distribution of the dust grains throughout the disk.

However, in order to analyze and interpret these observations we also need to understand the micro-physical processes by which dust grains can be affected. During the evolution of the disk and, in particular, during the last stages (Class II-III objects), several transport and growth processes control the evolution of dust grains. A scheme of these processes is shown in Fig. 1.2.

1.2.1 Grain growth

Grain growth occurs mainly through collisions of smaller dust grains. Depending on the relative velocity of the grains, their size and their composition, the collision can produce different outcomes (Testi et al. 2014, and references therein):

- **Sticking:** If the relative motion between the two particles is not too high, both grains can stick to each other and form a larger particle. Small grains can stick at higher velocities than larger grains. As a result, the early stages of grain growth are dominated by this mechanism, growing very efficiently up to sizes ~ 1 mm.

- **Bouncing:** If the colliding dust particles are too big (~ 1 mm), the efficiency of direct sticking decreases, resulting in bounces between the dust grains. As a consequence, there is a maximum grain size that can be formed through sticking of smaller particles. This size is known as the *bouncing barrier*.

- **Fragmentation:** If the collision velocity between two relatively large particles is too high, the two grains will not bounce but they will fragment, producing smaller dust particles. This mechanism has been found to be important to explain the presence of small dust grains in protoplanetary disks, since grain sticking is so efficient that without fragmentation most disks should be formed just by large dust grains (Birnstiel, Dullemond & Brauer 2009), contrary to what is observed.

- **Growth by mass transfer:** If a small and a large dust grains collide with a relative velocity close to the fragmentation velocity, the collision can result in a significant mass transfer from the small to the large particle. This mechanism is able to overcome the *bouncing barrier*, allowing grains to grow up to planetesimal sizes.

Therefore, small dust grains can grow efficiently up to sizes of ~ 1 mm through direct sticking. Afterwards, mass transfer allows dust grains to keep growing up to planetesimal sizes. During the whole process, fragmentation is able to replenish the population of small grains in the disk (Birnstiel, Dullemond & Brauer 2009). We note, however, that the maximum collision velocity between two particles, and

therefore the maximum size reachable through direct sticking, depends strongly on the composition and porosity of grains. In particular, icy grains or dust grains with icy mantles have been recently shown to require much higher velocities to fragment (Gundlach et al. 2011). This has been proposed to significantly enhance the dust grain growth at distances from the star larger than the water condensation front or snow line (see §1.5.3). Therefore, giant planets will more easily form beyond the water snow line.

1.2.2 Dust transport and migration

The two main physical processes that regulate the dust transport in protoplanetary disks are turbulence and drag forces. The gas in protoplanetary disks is significantly turbulent (Shakura & Sunyaev 1973), and therefore dust grains can be mixed because of this turbulent stirring. This mixing tends to homogenize the dust grain distribution and, hence, produce a constant dust-to-gas ratio throughout the disk.

Drag forces, on the other hand, are produced because of the relative motion between gas and dust particles, which produces a friction force. Because of the thermal pressure, the orbital motion of the gas can differ from a Keplerian rotation. As a consequence, solid particles can suffer a drag force that will accelerate or decelerate them and will tend to move the solid particles toward the pressure maximum of the gas. The force exerted on the dust particle will depend on its size. Since small particles (sub-micron sizes) are significantly influenced by the gas thermal pressure, they are coupled to the gas without suffering any significant drag force. Large particles (mm–cm sizes), on the other hand, can be strongly affected by drag forces, unless they grow up to ∼km sizes, at which point the drag force is not capable of producing a significant acceleration on the particle (Whipple 1972; Weidenschilling 1977). Therefore, the balance between turbulent mixing, which affects to all the dust particles, and drag forces, that affect mainly to large particles, will determine the size distribution of the dust grains throughout the disk.

In a protoplanetary disk, higher pressures are found in the midplane. Therefore, large dust grains will suffer a drag force that will settle them on the midplane, while small grains will be distributed throughout the disk height (Dubrulle, Morfill & Sterzik 1995; Fromang & Nelson 2009). This settling process is thought to lead to

a rapid growth of dust grains in the midplane. As the disk evolves and dust grains grow and settle on the midplane, the dust-to-gas ratio in the atmosphere will decrease, and a thin layer of a higher dust-to-gas ratio and larger dust grains or pebbles will be formed in the disk midplane. The effects of dust settling in the overall SED of protoplanetary disks have been studied in detail and have been able to explain the observed SEDs of disks around low and intermediate-mass stars (Dullemond & Dominik 2004; D'Alessio et al. 2006).

Drag forces can also have important implications in the radial direction (Whipple 1972; Weidenschilling 1977). To a first approximation, protoplanetary disks are axisymmetric, so they present a radial pressure gradient increasing toward the inner regions, closer to the star. Because of this thermal pressure, the gas in the disks orbits at slightly sub-Keplerian velocities. Therefore, large dust particles rotating around the star at Keplerian velocities suffer a drag force that will result in an inward spiral motion, i.e. a radial drift or migration. Small grains, on the other hand, will not be significantly affected by this drift, so they will be distributed throughout the disk with approximately the same distribution as the gas. This is consistent with recent observations of several protoplanetary disks, where scattered light (which trace the small dust grains in the disk atmosphere) or molecular line observations show sizes of hundreds of au, while (sub)-mm observations (which trace the mm–cm sized grains in the disk midplane) show much more compact disk sizes of tens of au (e.g., HD 163296: Grady et al. 2000; de Gregorio-Monsalvo et al. 2013; see Fig. 1.3; HD 100546: Ardila et al. 2007; Pineda et al. 2014). Additionally, radio interferometric observations of protoplanetary disks show more compact emission at cm wavelengths than at (sub)mm wavelengths, indicating that the larger the dust grains are, the closer to the central star they are because of radial migration (Pérez et al. 2012, 2015; Carrasco-González et al. 2016).

However, models predict very short drift timescales, which implies that mm–cm sized particles should migrate inward and even fall into the star within a small fraction of the expected protoplanetary disk life times (Brauer, Dullemond & Henning 2008; Birnstiel, Dullemond & Brauer 2009). This has been called the *drift barrier*, since it prevents dust grains to grow up to sizes $\gtrsim$ 1 m (Birnstiel, Dullemond & Brauer 2010). In order to stop particles from drifting inwards and overcome this problem, it has been proposed that dust particles could get trapped in pressure maxima within the disk,

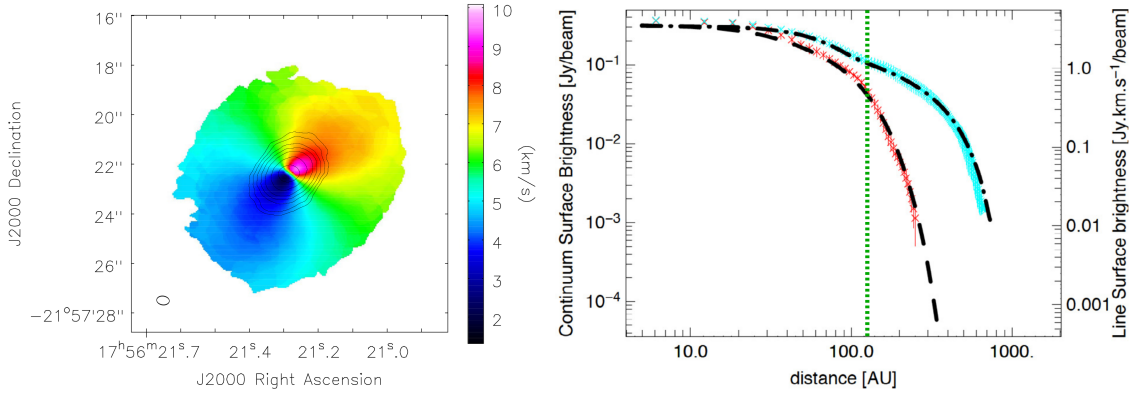

Figure 1.3 Left: Image of the dust and molecular line emission of the protoplanetary disk around the intermediate-mass star HD 163296. Colors represent the CO(3-2) intensity weighted mean velocity (first-order moment), while contours show the dust continuum emission at 0.85 mm. Right: Surface brightness profiles of the dust continuum (red) and CO(3-2) (blue) emission. The black dashed and dash-dotted lines represent the profiles obtained from the models fitted to the observations. Note that the gas emission is significantly more extended than the dust emission. Figure adapted from de Gregorio-Monsalvo et al. (2013).

where the radial pressure gradient is locally reversed and particles can be dragged toward the pressure maxima. Low-mass companions or planets can dynamically interact with the disk and create spiral density waves, vortexes and gaps (Papaloizou et al. 2007; Baruteau et al. 2014 and references therein). Spiral waves and vortexes represent high-pressure azimuthal asymmetries with spiral and lopsided (or horseshoe) morphologies, respectively, whereas gaps present axisymmetric pressure maxima at their outer edges. Models have shown that these structures could efficiently trap large dust grains (Zhu et al. 2012; Pinilla et al. 2012; Birnstiel, Dullemond & Pinilla 2013; Zhu & Stone 2014; see Fig. 1.4). These dust traps should be detectable in the mm and submm observations of disks with ongoing planetary formation, since large dust grains emit efficiently at these wavelengths. In fact, very similar structures have been detected in several protoplanetary disks, and they are usually interpreted as signs of planetary formation within the disk (e.g., van der Marel et al. 2013; Pérez et al. 2014; see Fig. 1.5 and §1.4). Nevertheless, this mechanism requires that a planet has already been formed in the disk, so another mechanism is needed to overcome the *drift barrier* and form a planet that could then create these dust traps. Recently,

magneto-rotational instabilities in magnetized disks (Bai & Stone 2014; Flock et al. 2015) and condensation fronts of volatiles in the disk (Ros & Johansen 2013; Zhang et al. 2015) have been proposed as possible mechanisms to create dust traps. We explain in more detail these processes in §1.5.

1.3 Disk dispersal and photoevaporation

Class III YSOs present almost no gas in their circumstellar disks. Observations show that the gas dispersal in disks occurs over timescales of 1–10 Myr, indicating that it is quite an efficient process(Hartmann 2009). Gas removal from disks is expected to have important implications for planetary formation. First, it sets an upper limit on the timescale of gas giant planet formation by limiting over time the amount of gas available for their formation. In addition, it could also set a lower limit on this timescale, since recent models show that planetesimal formation requires dust-to-gas ratios in the disk significantly higher than in the interstellar medium (Drążkowska & Dullemond 2014). Finally, gas removal could also stall dust and planet migration, as well as modify the chemical composition of the disk (Alexander et al. 2014).

During the early stages of protoplanetary disk evolution, viscous accretion is commonly thought to dominate disk evolution (Shakura & Sunyaev 1973; Lynden-Bell & Pringle 1974). However, the timescale of viscous evolution is estimated to be $\gtrsim 10$ Myr in the outer regions of protoplanetary disks (Hartmann et al. 1998). Therefore, viscous evolution is not able to disperse the disk in the timescales of 1–10 Myr indicated by observations, so other mechanisms are needed to drive disk dispersal during the last stages of disk evolution.

MHD-driven disk winds (Bai 2013) and jets (Cabrit 2007) can extract mass and angular momentum from the disk, although mainly at early times. Binary companions or stellar encounters can tidally interact with the disk and even remove most of the mass. In addition, disks can also be externally evaporated due to the radiation and winds from close massive stars (e.g., Orion proplyds, Henney & O'Dell 1999; Mann et al. 2014). However, these processes are rare and can only remove a significant fraction of the disk material in a small number of disks. On the other hand, planets can also shape the protoplanetary disks, opening cavities and gaps (see §1.4), but the fraction of the initial disk mass that is converted into planets is small, as

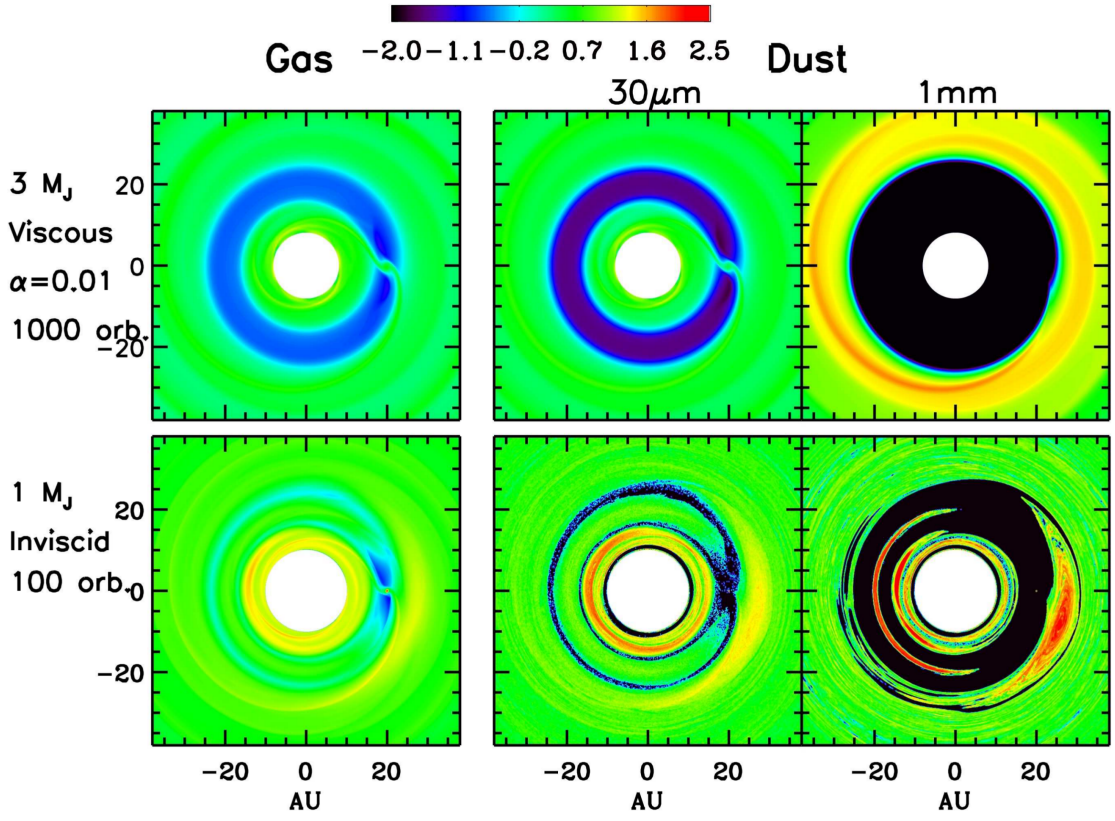

Figure 1.4 Disk surface density of the gas (left panels) and dust grains of different sizes (right panels) obtained from hydrodynamical simulations. The upper panels include a 3 M_J planet in a viscous disk, while the lower panels have a 1 M_J planet in an inviscid disk. The planets open a gap and create a vortex and asymmetric features in the gas and dust surface densities of the disk. The larger dust grains (1 mm) are trapped at the outer edge of the gap and in the vortex, whereas the smaller dust grains can cross the gap and fill the inner regions of the disk more efficiently. Figure from Espaillat et al. (2014), adapted from Zhu et al. (2012) and Zhu & Stone (2014).

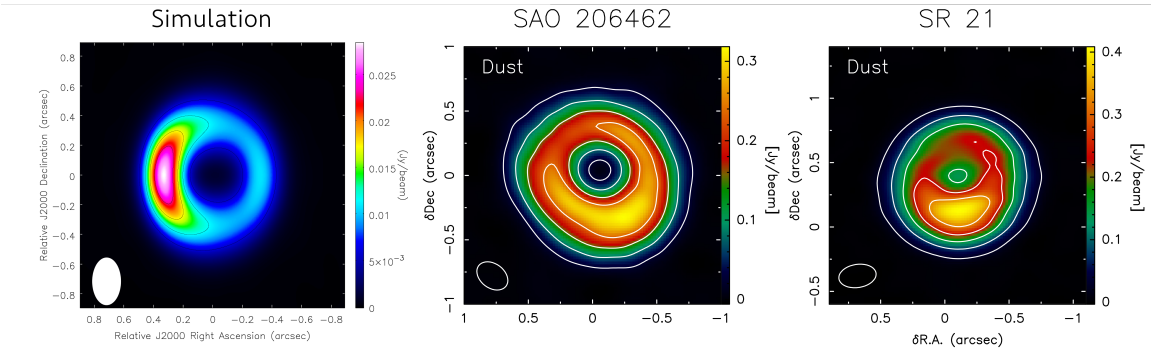

Figure 1.5 Left panel: Simulated image of an azimuthally asymmetric dust trap as would be observed by ALMA at 0.87 mm (Birnstiel, Dullemond & Pinilla 2013). Two right panels: ALMA observations of the dust emission at 0.45 mm of the disks around the pre-main sequence stars SAO 206462 and SR 21 (Pérez et al. 2014).

indicated by observations of exoplanetary systems.

Finally, another dispersal mechanism that is usually proposed is photoevaporation, which is generally considered the dominant mechanism for gas removal (Alexander et al. 2014). High energy radiation emitted at the stellar chromosphere of the central star can heat and photoionize the surface of the disk (Font et al. 2004; Gorti, Dullemond & Hollenbach 2009; Owen et al. 2010). If the thermal energy of this heated gas is higher than the gravitational binding energy, the gas can escape and a pressure-driven photoevaporative wind is launched.

There are three main ranges of wavelengths that can contribute to the disk photoevaporation: far-UV (FUV; 6–13.6 eV), extreme-UV (EUV; 13.6–100 eV) and X-rays (0.1–10 keV). Each of these types of radiation heats the disk surface in a different way and, therefore, creates different mass-loss rates and profiles. FUV photons can dissociate H_2 and other molecules (Gorti, Dullemond & Hollenbach 2009), but they do not have enough energy to ionize the gas. This type of high-energy radiation may play an important role at early stages of disk evolution, when a high excess of FUV emission is created in the accretion shock (EUV and X-rays will be absorbed by accretion flows and the envelope of the star and will not reach the disk surface). Nevertheless, during the last stages of disk evolution EUV and X-ray radiation are thought to dominate the heating of the gas (Alexander et al. 2014).

EUV photons are highly absorbed by the hydrogen atoms and, thus, create a fully

photoionized surface that can be treated as a bounded H II region at $T \sim 10^4$ K (Font et al. 2004). On the other hand, X-rays are absorbed by heavy elements, ejecting electrons that can then collisionally ionize and heat the rest of the gas. Therefore, X-rays can penetrate much deeper into the disk creating a partially ionized region at $T \sim 10^3$–10^4 K (Gorti, Dullemond & Hollenbach 2009). As a consequence, the photoevaporative wind in the EUV case would be fully ionized (Font et al. 2004), while in the X-rays case the wind would be denser (i.e. producing a higher mass-loss rate) but only partially ionized (Gorti, Dullemond & Hollenbach 2009; Owen et al. 2010). Current models predict that X-ray-driven photoevaporation will dominate in most of the Class II systems, producing mass-loss rates between $\sim 10^{-10}$–10^{-8} $M_\odot$ yr^{-1}. These rates might be higher than the mass accretion rates estimated from observations in several systems, indicating that photoevaporation could efficiently disperse the gas of the disk. In particular, Owen, Clarke & Ercolano (2012) proposed that once the mass loss rate in the photoevaporative wind overcomes the mass accretion rate in the disk, a hole or gap could be created. This would result in a direct irradiation of the disk at the edge of the gap, which would significantly increase the mass loss rate of the X-ray-driven wind and lead to a rapid dispersal of the disk, in a process called *thermal sweeping*. Nevertheless, it remains unclear whether this process is consistent with current observations (Espaillat et al. 2014).

Evidence for the presence of photoevaporative winds has been found in different protoplanetary disks, mostly through optical and mid-IR forbidden line emission (such as [O I] 6300 Å and [Ne II] 12.81 μm; Pascucci & Sterzik 2009; Sacco et al. 2012), but estimates of the mass loss rates in these winds cannot be obtained from these observations. Most observations are sensitive only to the ionized component in the wind. Therefore, the observational results can be reproduced either by a fully ionized EUV-driven wind or a partially ionized X-ray-driven wind with mass-loss rates that differ by up to 1 or 2 orders of magnitude. More theoretical and observational studies are still needed to determine the timescale and impact of photoevaporation in the evolution of protoplanetary disks.

1.4 Transitional disks

In this work we will define transitional disks as accretion disks around YSOs whose dust distribution presents inner cavities or gaps, typically of tens of au in size. These objects are thought to be in a transition phase from full disks that extend inward up to very close distances from the star (i.e., disks around Class II objects), to more tenuous or even dissipated disks (i.e., disks around Class III objects). Transitional disks were first identified by Strom et al. (1989) as disks showing small near and mid-IR excesses of emission above the stellar emission, although still showing significant far-IR excesses. The far-IR emission of protoplanetary disks is dominated by the outer regions of the disk, which are colder but also more massive than the inner regions. On the other hand, the near and mid-IR emission is dominated by optically thick emission of the denser and warmer regions, located closer to the star. The small near and mid-IR emission in the disk SED indicates that the dust distribution in transitional disks presents an inner cavity or hole, where the disk is almost devoid of warm dust grains. Because of this, Strom et al. (1989) proposed that this type of disks could represent disks that were in transition from full optically thick disks to more tenuous, perhaps post-planet-building, disks. Transitional disks, thus, appear as excelent laboratories to study the first stages of planetary formation.

The infrared spectrographs on board *ISO* and *Spitzer Space Telescope* (Infrared Spectrograph; IRS), made it possible to perform several detailed studies of the SED of protoplanetary disks, identifying an increasing number of transitional disks (D'Alessio et al. 2005; Calvet et al. 2005). These studies also lead to the discovery of a subfamily of transitional disks that exhibit the characteristic small mid-IR excess of emission, although still showing a relatively high excess of emission at near-IR wavelengths. These objects were interpreted as disks with a residual inner optically thick disk that can still emit at near-IR wavelengths, separated from the outer disk by an annular gap devoid of dust (Espaillat et al. 2007). These objects were called pre-transitional disks, since they were proposed to represent an intermediate evolutionary stage between full disks and transitional disks (see Fig. 1.6).

Recently, mm and submm interferometric observations (e.g., Hughes et al. 2007; Andrews et al. 2011; Pérez et al. 2014; Osorio et al. 2014, see Chapter 2), as well as near-IR interferometric and polarimetric observations (e.g., Quanz et al. 2011; Thal-

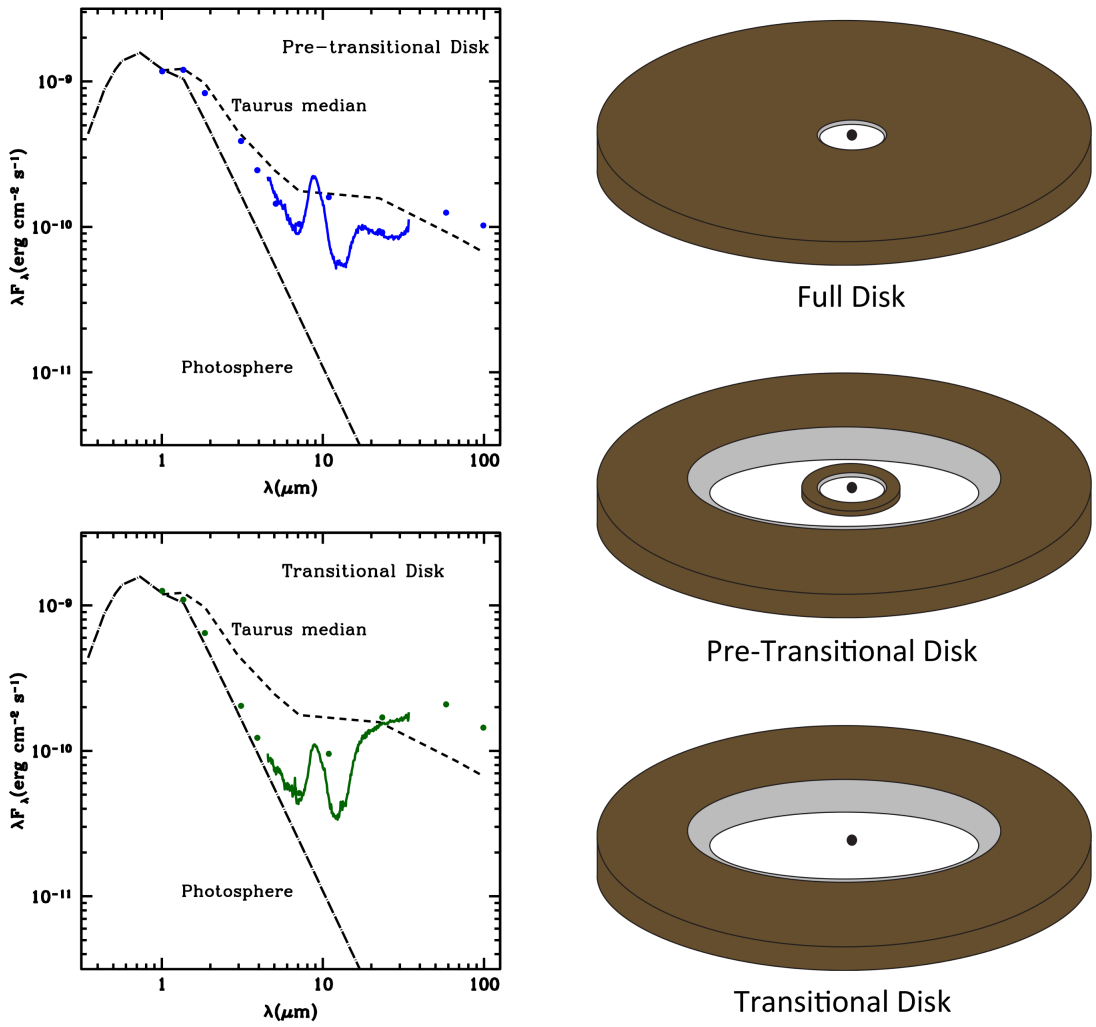

Figure 1.6 Left: Scaled SEDs (dots and solid lines) of a pre-transitional disk (top; LkCa15; Espaillat et al. 2007) and a transitional disk (bottom; GM Aur; Calvet et al. 2005), compared to the median SED of YSOs with disks in Taurus (short-dashed line), which should represent the expected emission for a full disk (D'Alessio et al. 1999). The dot-long-dashed line represents the stellar photosphere emission. As can be seen, a transitional disk has a deficit of emission in comparison to the median Taurus SED from $\sim$ 1 μm up to wavelengths $\gtrsim$ 20 μm, with its near-IR emission being very similar to the stellar photospheric emission. A pre-transitional disk, on the other hand, shows a deficit of emission at mid-IR wavelengths (5–30 μm) but similar near-IR emission (1–5 μm) to the Taurus median SED. Right: Schemes of a full (top), a pre-transitional (middle), and a transitional (bottom, top-right) disk. Figure adapted from Espaillat et al. (2014).

mann et al. 2015), have started to image and angularly resolve cavities of tens of au in size in a number of transitional disks, confirming that the inner regions of these disks are devoid of dust. Submm and mm observations are sensitive mainly to the large dust grains (mm-cm sized) located in the disk midplane, while IR polarimetric observations trace the scattered light emission from the small grains ($\lesssim 1$ μm) located in the uppermost layers of the disk (see Fig. 1.2). High angular resolution observations of transitional disks at (sub)mm wavelengths can show a ring-like structure that traces the rim of the inner cavity. For disks with high inclination angles (close to edge-on), however, the emission shows a double peak morphology along the major axis of the disk produced by a limb-brightening of the inner edge of the disk (Andrews et al. 2011; see Fig. 1.7). In addition, in a number of cases mm and submm observations of transitional disks show azimuthal asymmetries close to the outer edge of the cavity or gap (See Fig. 1.5 and 1.7, Andrews et al. 2011; van der Marel et al. 2013; Pérez et al. 2014). These asymmetries are interpreted as accumulations of large dust grains in vortexes or pressure maxima in the disk (Birnstiel, Dullemond & Pinilla 2013; see §1.2).

Nevertheless, near-IR polarimetric observations can reveal disks with morphologies different to those observed at mm and submm wavelengths. Based on the morphology of the observed scattered light emission, transitional disks can be classified in three different categories (Espaillat et al. 2014): (i) disks presenting no cavities or gaps in scattered light and showing a smooth radial surface brightness profile; (ii) disks without inner cavities or gaps in scattered light, but showing a flat slope in the inner regions of the disk and then a steep decline in the outer regions; (iii) disks with a clear inner cavitiy or gap in the scattered light emission. The radius of this cavity is usually similar or smaller than the radius of the cavity revealed by (sub)mm observations.

Therefore, even though large dust grains in transitional disks are significantly depleted in the inner cavities or gaps, a relatively large amount of submicron sized grains may still be present inside the cavity. This indicates that the spatial distribution of small and large dust grains in transitional disks might be significantly different (Grady et al. 2000; de Gregorio-Monsalvo et al. 2013). These differences could be due to an evolutionary effect of the dust grain size distribution, or could represent different types of disks with different origins for their inner cavities or gaps.

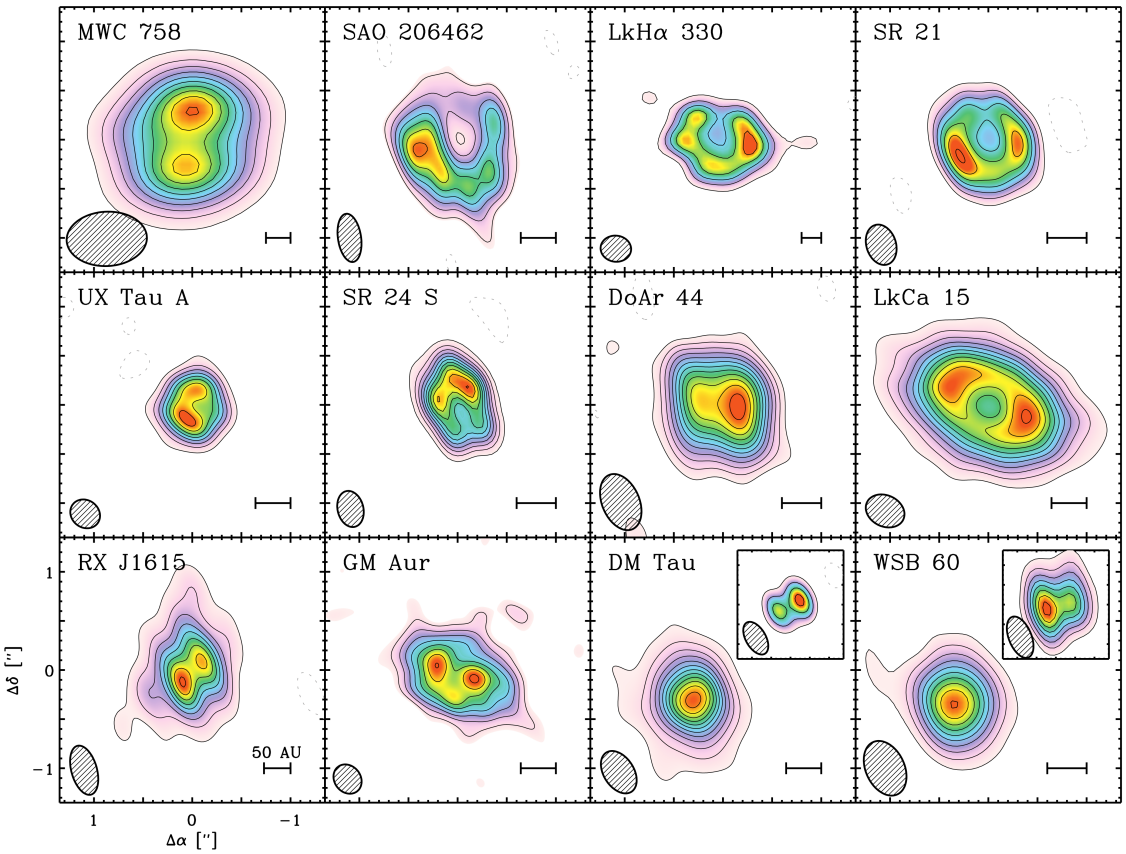

Figure 1.7 Images of the 0.88 mm dust emission of a sample of transitional disks obtained with the Submillimeter Array (SMA). Low-inclination objects show a ring-like structure (e.g., SR 21, LkHα 330), whereas disks with high inclinations show a characteristic double peak morphology (e.g, MWC 758, GM Aur). Figure from (Andrews et al. 2011).

The gas distribution in transitional disks can also present morphologies different from that of the dust. Several transitional disks have relatively high mass accretion rates ($\sim 10^{-8}$ $M_{\odot}$ yr^{-1}), which suggests the presence of gas inside the dust cavity either in a residual inner disk or flowing through the cavity. Additionally, molecular line observations have revealed that some transitional disks present gas inside the cavity with relatively low depletion factors (e.g. van der Marel et al. 2015), although some other disks show cavities in the gas distribution with similar radii than the cavities in the dust distribution (e.g., Brittain et al. 2014; van der Marel et al. 2016; Brittain et al. 2014).

1.4.1 Clearing mechanisms

Since the first identifications of transitional disks, several mechanisms have been proposed to clear their inner cavities and gaps in the dust distribution. Here we list the three most popular mechanisms:

- **Grain growth:** Some studies have proposed that grain growth may produce a dip in the IR SED due to the lower emissivity at these wavelengths of the large dust particles (Dullemond & Dominik 2005). Since grains are expected to grow faster in the denser, inner regions of the disk, a region of lower IR emission could be created. However, Birnstiel, Andrews & Ercolano (2012) showed that dust fragmentation will replenish the inner regions of the disk with small grains that will increase again the IR emission (see §1.2). In addition, large dust grains emit efficiently at mm–cm wavelengths, so grain growth cannot explain the cavities observed by interferometric observations at these wavelengths. Therefore, grain growth alone cannot be the responsible for the creation of cavities and gaps in transitional disks.

- **Photoevaporation:** As explained in §1.3, high energy radiation emitted by the central star can heat and photoionize the surface of the disk. When the thermal energy of this heated gas is higher than the gravitational binding energy, a photoevaporative wind is formed (Font et al. 2004; Gorti, Dullemond & Hollenbach 2009; Owen et al. 2010). This wind should be able to stop the re-supply of material to the inner regions of the disk when the mass accretion

rate in the disk is lower than the mass loss rate in the wind. At this point, the inner regions of the disk can accrete onto the star and create an inner cavity. Some transitional disks with low mass accretion rates and relatively small cavities seem to be consistent with a photoevaporative origin for their cavities (e.g., TW Hya: Pascucci & Sterzik 2009). However, most transitional disks are difficult to explain with photoevaporation, since they show relatively high mass accretion rates and, thus, photoevaporation could not have stopped the re-supply of material to the inner regions of the disk. Photoevaporation is also unsuccesful in reproducing the several azimuthal asymmetries that have been observed in transitional disks at mm and submm wavelengths (Andrews et al. 2011; van der Marel et al. 2013). Furthermore, there exist protoplanetary disks with very low mass accretion rates that do not show signs of cavities or gaps, which suggests that photoevaporation models might be overestimating the mass loss rates produced by the winds (Ingleby et al. 2012).

- **Dynamical clearing by companions or planets:** Tidal interactiones between the disk and low-mass companions, such as stars, brown dwarfs or planets, can result in the creation of cavities and gaps in the disk (Baruteau et al. 2014). In fact, in some transitional disks, young planets have been detected inside the observed cavities (e.g., LkCa15, Sallum et al. 2015). This mechanism can succesfully explain most of the observational constraints. Planets can still allow the gas to flow through the cavity, hence maintaining significant accretion rates onto the star as has been observed in most transitional disks (Espaillat et al. 2014). In addition, the dynamical interactions with the low-mass companions or planets can also produce azimuthal asymmetries like spiral density waves and vortexes. These asymmetries can trap the large dust grains (see §1.2) in the disk producing features like the ones observed at mm and submm wavelengths (Birnstiel, Dullemond & Pinilla 2013). Finally, dynamical clearing can also trap large dust grains at the outer edges of cavities or gaps much more efficiently than small dust grains, letting most of the latter through (Zhu et al. 2012; see §1.2). This process, also called *dust filtration*, would therefore result in a more rapid formation of a cavity in the large dust grain distribution than in the small grain and gas distribution. This would naturally explain the observed

differences in the spatial distribution of gas, small, and large dust grains as an evolutionary process that depends on the mass of the planet (Zhu et al. 2012).

Therefore, even though photoevaporation may have an important impact in some transitional disks, dynamical interactions with companions is the clearing mechanism that can more succesfully reproduce the observational signatures of transitional disks (Espaillat et al. 2014). Nevertheless, the sample of observed transitional disks is still relatively small, and it is possible that, due to an observational bias, most of the transitional disks that have been studied belong to a family of denser disks that can form giant gas planets capable of opening the observed cavities (Owen & Clarke 2012). More observations are needed to completely understand the impact of each of these processes in the evolution of protoplanetary disks.

1.5 Multiple gaps and ringed substructure in protoplanetary disks

Recently, observations obtained using the ALMA, with the highest sensitivity and angular resolution ever achieved at (sub)mm wavelengths, have revealed the presence of multiple gaps and rings in the protoplanetary disks around the two solar-type stars HL Tau (see Fig. 1.8; ALMA Partnership et al. 2015a) and TW Hya (see Fig. 1.9; Andrews et al. 2016). Interestingly, these two objects are thought to be in two different evolutionary stages, with a difference in their ages of a factor of ~ 10. While HL Tau is a ~ 1 Myr Class I YSO, still surrounded by a relatively tenuous envelope, TW Hya is known to be in a relatively advanced stage, with an age of ~ 10 Myr and signs of considerable grain growth up to $\sim$cm sizes. Additionally, the disk around TW Hya is a transitional disk with a small inner cavity or gap ~ 2 au in radius (Calvet et al. 2002; Hughes et al. 2007; Andrews et al. 2016).

Despite this difference in age, the ringed substructure detected in the HL Tau and TW Hya disks has significant simmilarities, which suggests that at least some gaps might have a similar origin. In both cases, the emission shows a number of gaps $\sim$ 1–5 au in width, some of them surrounded by rings of enhanced emission. These gaps are significantly different to the inner cavities or gaps observed in transitional disks, which are typically much wider (tens of au) and deeper. This type of ringed

substructure could also be present in other transitional disks, but previous (sub)mm observations lacked the sensitivity and angular resolution necessary to resolve them. These recent ALMA observations toward HL Tau and TW Hya have triggered several theoretical studies aimed at explaining the formation of these ringed substructures. The proposed mechanisms to reproduce the observed gaps can be broadly summarized in three categories: dynamical interactions with planets, turbulence driven by magnetorotational instability (MRI) in magnetized disks, and grain accumulation and growth close to condensation fronts of volatiles in the disk.

1.5.1 Dynamical interactions by planets

Dynamical interactions between the disk and a forming planet can create gaps in the density distribution of the disk and trap large dust grains at the outer edges of the gaps (Baruteau et al. 2014; Zhu & Stone 2014). This is in fact the same mechanism that was proposed to produce the inner cavities of transitional disks (see §1.4).A number of studies have shown that relatively low-mass planets (tens of $M_{\oplus}$) are already able to open narrow gaps as the ones observed (Dong, Zhu & Whitney 2015; Picogna & Kley 2015).

These interactions could be the underlying mechanism responsible for the creation of some of the closer gaps to the star, but it is unclear whether planets can be formed at distances as long as $\sim$ 40–70 au, where the surface densities in the disk are significantly lower. As a comparison, the dwarf planet Pluto in our solar system is located at an average distance of 39.5 au but its mass is only $\sim 0.002\ M_{\oplus}$, which would not be enough to open gaps as the ones observed in the disks around HL Tau and TW Hya. Furthermore, the young age of HL Tau ($\lesssim$ 1–2 Myr) makes it even more unlikely that a planet has already been formed in the protoplanetary disk, specially at long distances from the star where dust grain growth processes are slower.

Therefore, even though dynamical interactions with planets could explain some of the gaps in TW Hya, particularly the innermost cavity (although photoevaporation has also been proposed as an alternative mechanism, Pascucci et al. 2012), it is unlikely that this process can explain most of the gaps and ringed substructure observed in the HL Tau and TW Hya disks.

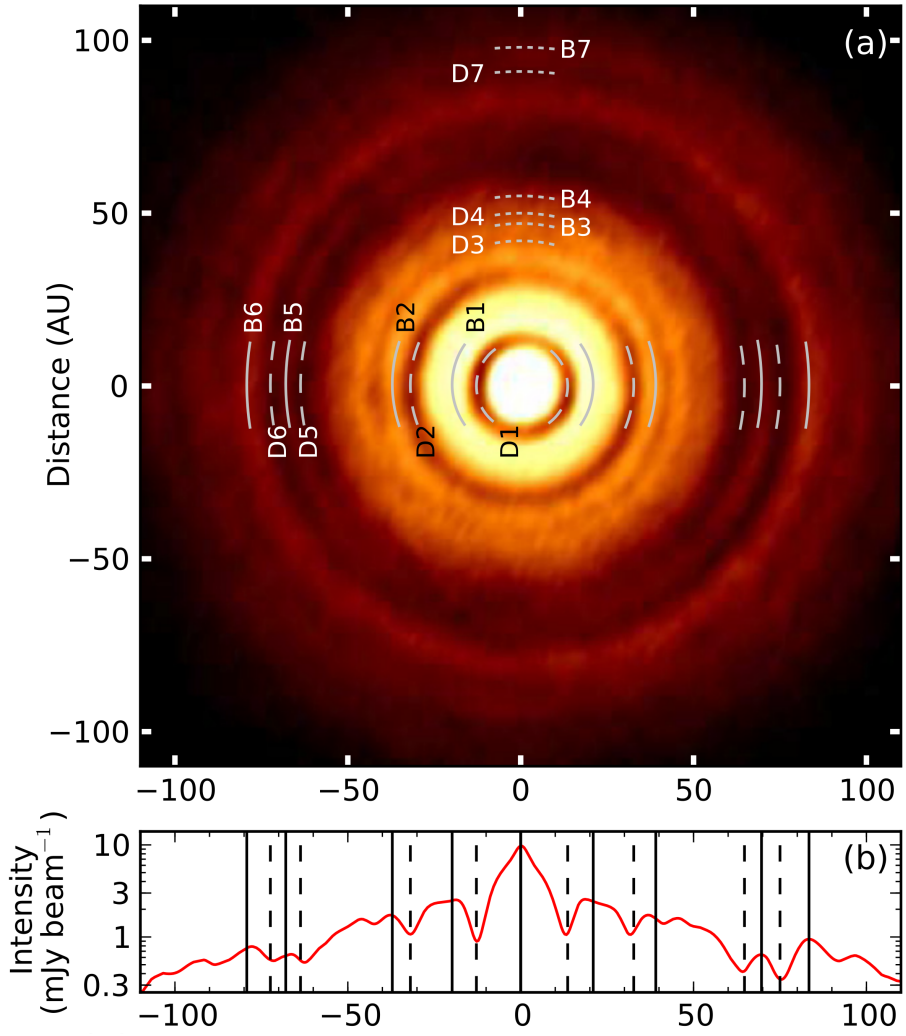

Figure 1.8 (a): Deprojected image of the dust thermal emission at 1.0 mm of the protoplanetary disk around HL Tau. The angular resolution is 39 × 19 mas (PA= −21°). The rings and gaps found in the disk are indicated in the image. (b): Radial intensity profile of the 1.0 mm image of the HL Tau disk obtained from a slice throughout the disk at a PA= 138°. The vertical lines indicate the positions of the most prominent rings (solid lines) and gaps (dashed lines). Figure adapted from ALMA Partnership et al. (2015a).

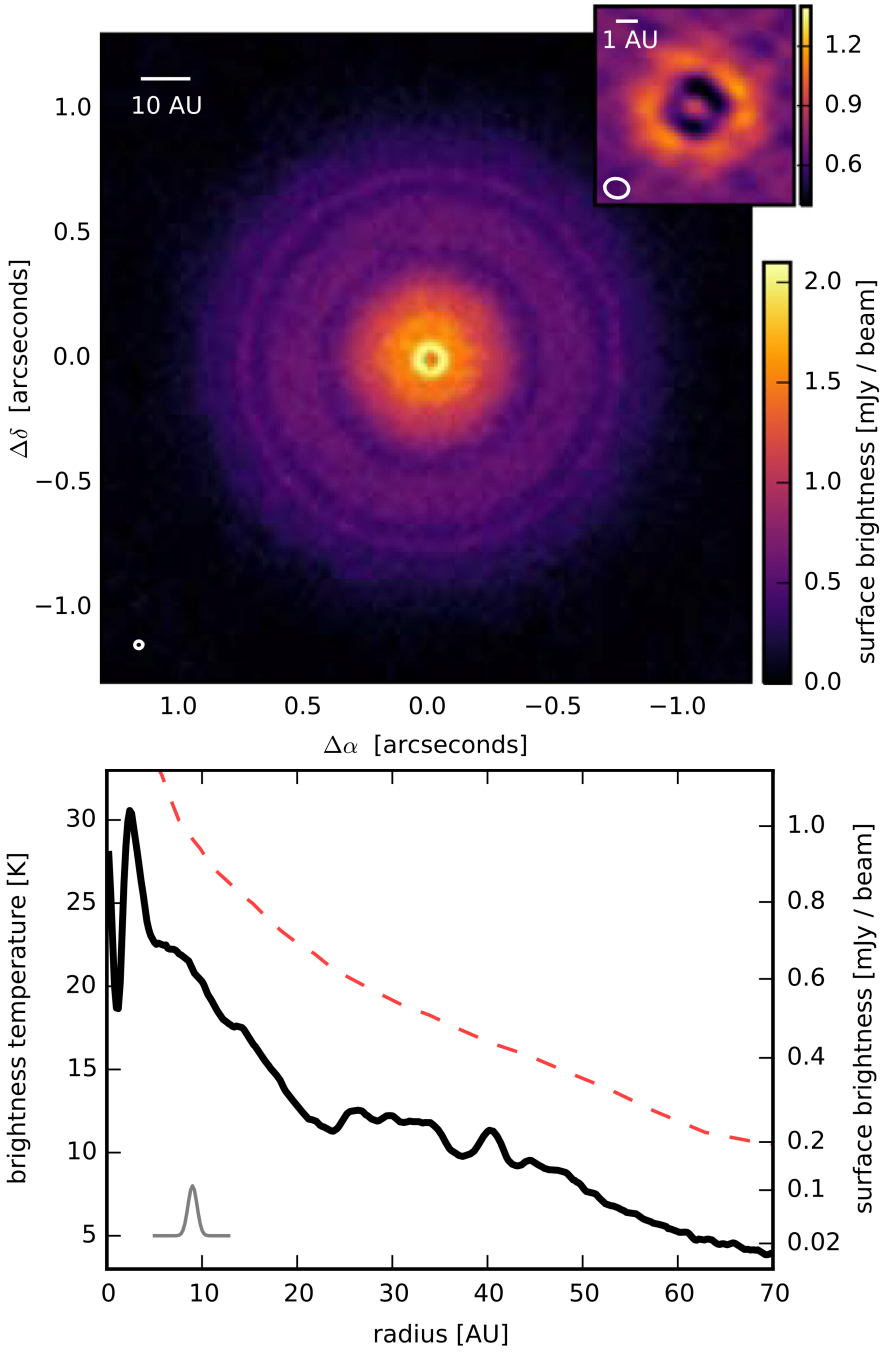

Figure 1.9 Top: ALMA image of the dust thermal emission at 0.87 mm of the transitional disk of TW Hya. The synthesized beam is 30 × 30 mas. The inset shown in the top right shows a 0.″2 wide zoom of the central region of the disk using a higher angular resolution (24 × 18 mas). Bottom: Azimuthally averaged radial intensity profile of the 0.87 mm image of the TW Hya disk. The red line shows the midplane temperature estimated from a model disk, whereas the gray curve shown in the bottom left represents the synthesized beam profile. Figure adapted from (Andrews et al. 2016).

1.5.2 MRI-driven turbulence in magnetized disks

Turbulence driven by magnetorotational instability (MRI) in magnetized protoplanetary disks can produce radial pressure variations, also known as zonal flows. Local simulations show that these pressure maxima can appear throughout the disk, separated a few au and with amplitudes up to $\sim$ 30%–50% above the unperturbed pressure gradient (Bai & Stone 2014; Suzuki & Inutsuka 2014). However, it is unclear whether these zonal flows can produce gaps in the dust distribution as deep as most of the observed gaps in the HL Tau and TW Hya disks. Additionally, the current observational estimates of magnetic fields and turbulence in disks are very limited (Hughes et al. 2011), so the real impact of zonal flows is still not completely understood.

On the other hand, MRI can also create ring and gap features at the outer edge of the so-called dead zones (Flock et al. 2015). Dead zones are regions in the disk with low-ionization, which supresses the MRI turbulence (Blaes & Balbus 1994; Turner, Carballido & Sano 2010). At the edges of these regions, the transition from (or to) a highly ionized zone reactivates the MRI, which can produce an increase of the accretion flows in the disk and, therefore, an enhancement of the surface density. Flock et al. (2015) carried out MHD simulations of a generic disk around a low-mas star and showed that a large gap can be formed at the outer edge of the dead zone, followed by an axisymmetric ring of enhanced surface density at outer radii. These structures are similar to the zonal flows, but in this case the gap can be much wider and deeper, depending on the physical properties of the disk. The pressure bump at the enhanced density ring is strong enough to efficiently trap the large dust grains, creating at (sub)mm wavelengths a detectable bright ring at a radius of $\sim$ 60 au, following a gap of $\sim$ 10 au in width at a radius of $\sim$ 50 au from the star. Furthermore, the enhanced density of the bright ring could be high enough to even induce the formation of azimuthal vortexes (Flock et al. 2015), although the HL Tau and TW Hya observations do not show these features.

Thus, MRI in magnetized disks seems to be a promising mechanism to explain at least some of the ringed disk substructure detected in HL Tau and TW Hya at mm and submm wavelengths. Nevertheless, it is still difficult to directly compare models and observations due to the incomplete information of the distribution of the magnetic field in protoplanetary disks. More observations are needed to determine whether

magnetized disks can create this ringed substructure and reproduce the (sub)mm observations.

1.5.3 Grain accumulation and growth close to condensation fronts

Volatiles are molecules that can be either in gas or solid phase inside the protoplanetary disks. Some of the most abundant volatiles in disks, as revealed by the composition of comets in the solar system, are water, CO, CO_2 or NH_3 (Mumma & Charnley 2011). The regions in the disk where volatiles freeze out of the gas phase onto the surface of dust grains are known as condensation fronts. At radii smaller than that of the condensation front the volatiles will be in the gas phase, while at larger radii, where the temperature is lower, the volatiles will be in the solid phase. The location of these fronts in the disk will depend on the properties of each particular volatile, as well as on the temperature and density distribution of the disk. Temperature in protoplanetary disks is usually higher in the atmosphere, where the disk is irradiated by the star, and lower in the midplane. Therefore, the condensation front of a particular volatile will not be at a unique radius, but it will actually be a surface that extends up to larger radii in the disk atmosphere than in the midplane. The radius of the condensation front in the midplane is usually defined as snow line, and it will often be the point of the condensation front that is closest to the central star [1].

Condensation fronts of volatiles in the disk can have a significant impact on the dust grain evolution. In particular, grain growth is expected to be more efficient close these snow lines thanks to the increased sticking efficiency of ice-coated grains (Gundlach et al. 2011). Furthermore, the continuous recondensation of volatiles diffusing across the snow line has been predicted to enhance the dust particle growth as well (Ros & Johansen 2013). Additionally, dust grains migrating toward the inner regions of the disk will cross the snow line and release volatiles from their icy mantles. This release of volatiles near their snow lines could increase the local surface density of the gas, which will in turn result in a pressure bump (Ros & Johansen 2013). The change in size of the grains produced close to the snow lines has been also suggested to produce a reduction in the depth of the active layers of the disk, where MRI is

[1] When viscous heating is taken into account, the minimum temperature is reached slightly above the midplane in the inner regions of the disk.

able to generate turbulence. As a consequence, a local pressure maximum could be formed at the snow lines of volatiles in the disk (Kretke & Lin 2007). Large dust grains could be trapped in these pressure bumps, producing a ring of enhanced dust surface density followed by a depletion of large dust grains at inner radii. This dust trapping, together with the enhanced dust grain growth at these radii, could create a ringed substructure in the mm and submm emission similar to the one observed in HL Tau and TW Hya (Zhang et al. 2015; Andrews et al. 2016).

On the other hand, sintering has also been proposed as a mechanism to explain emission rings close to snow lines in the disk (Okuzumi et al. 2016). Sintering is the process of bonding or fusing dust grains by creating a joint or neck between the particles. This process can occur at temperatures slightly below the sublimation temperature of volatiles. The resulting sintered dust aggregates are thought to be less sticky, and therefore can more easily fragment into smaller particles. This could result in an accumulation of smaller dust grains due to the fact that they are less affected by radial drift. Okuzumi et al. (2016) proposed that these accumulations would produce rings of enhanced surface density that would be optically thick at (sub)mm wavelengths and hence appear as bright rings of emission.

In fact, the most prominent gaps in HL Tau and TW Hya (except for the inner gap in TW Hya), seem to be located at the position of the snow lines of some of the most abundant volatiles in protoplanetary disks (Zhang et al. 2015; Andrews et al. 2016). This strongly suggests that the origin of at least some of the gaps is related to the presence of these snow lines. However, the temperature distribution in the mid-plane cannot be easily measured, so it is usually estimated with models that are subject to uncertainties related to model assumptions such as dust grain properties or vertical gas and dust density distributions. In addition, it is unclear whether snow lines of volatiles apart from water, CO and CO_2, which are thought to be the most abundant, can have a substantial impact in order to reproduce the observed ringed substructure.

1.6 Motivation and methodology

The main goal of this thesis is to study the initial conditions and overall process that leads to the formation of a planetary system. Planets are formed in circumstellar accretion disks around pre-main sequence stars. Forming planets can interact with the disk creating gaps or cavities. Therefore, transitional protoplanetary disks, which are disks with inner cavities or gaps, appear as great laboratories to study planetary formation. These cavities have been imaged at near-IR and (sub)mm wavelengths in a number of cases. We are at the point where structures with multiple gaps are starting to be discovered in protoplanetary disks. In particular, in this thesis we aim to contribute to understand, among others, the following topics:

- How are large dust grains distributed in transitional disks?
- Do all cavities and gaps in protoplanetary disks have the same nature and origin?
- What are the physical properties (mass, dust settling, etc.) of transitional disks?
- Exoplanetary systems show a diversity of architectures. Is there a similar diversity in their precursors, the protoplanetary disks? Is there a lower limit to the size and mass of a protoplanetary disk in order to form a planetary system?
- Do transitional disks still present collimated outflows?
- Does photoevaporation have a significant impact on the dispersal of protoplanetary disks?

In order to do this we have observed three different transitional disks at cm and mm wavelengths. We have used the Karl G. Jansky Very Large Array (VLA) and the Atacama Large Millimeter/Submillimeter Array (ALMA) to obtain images with very high sensitivity and angular resolution. At mm wavelengths we have mainly studied the dust thermal emission of the disks, which is dominated by the large dust grains (mm-cm sized).

On the other hand, the observations at cm wavelengths reveal a combination of the thermal emission from dust and the free-free emission from ionized gas. This

ionization can be produced by high energy radiation from the star or by shocks in an accretion-driven jet. Thus, these observations have allowed us to study the impact of jets and photoevaporative winds in the observed transitional disks.

Additionally, we have modeled the dust emission of the disk using self-consistent radiative transfer codes initially developed by D'Alessio et al. (1998; 1999; 2001; 2006). These codes calculate self-consistently the radial and vertical temperature and density distributions of irradiated accretion disks, taking into account the settling of large dust grains, the viscous heating and the irradiation from the star. The codes provide the broadband (from optical to cm wavelengths) SED of the disk and the directly irradiated walls of the gaps, as well as images at specific wavelengths. We have introduced small modifications to the code to improve the calculation of the emission of the cavity wall at mm wavelengths, where the disk can be optically thin, and to improve the calculation of the disk properties at the innermost regions of the disk.

The thesis is structured as follows:

- In chapter 2 we study through VLA observations of relatively high angular resolution and modeling the disk around the intermediate-mass star HD 169142. The disk shows an inner gap, a bright ring of emission, and an outer gap, with similar radii as the polarized near-IR images. Our detailed modeling provides us with the physical parameters of the disk.

- In chapter 3 we report the results of a follow-up multiwavelength study with the highest angular resolution of the VLA toward HD 169142. These high angular resolution observations have revealed the presence of a central free-free emission component within the inner gap, as well as a new third gap in the disk at a distance $\sim$ 100 au.

- In chapter 4 we report the discovery of a dwarf pre-transitional disk around XZ Tau B. We present ALMA observations at 1.3 mm, revealing the presence of a very small disk $\sim$ 3.4 au in radius with a central cavity of radius $\sim$ 1.3 au. We carried out a detailed modeling of the dust emission, showing that the disk could be ongoing planetary formation.

- In chapter 5 we present multiwavelength VLA observations of the transitional

disk around GM Aur. We study the dust and free-free emission of the object, revealing the presence of an accretion-driven jet and a photoevaporative wind arising from the surface of the disk.

- Finally, in chapter 6 we summarize our results and outline the future work.

1.7 List of publications

The work presented in this thesis has originated the following publications:

- *"Imaging the Inner and Outer Gaps of the Pre-Transitional Disk of HD 169142 at 7 mm"*
  Osorio, M., Anglada, G., Carrasco-González, C., Torrelles, J. M., **Macías, E.**, Rodríguez, L. F., Gómez, J. F., D'Alessio, P., Calvet, N., Nagel, E., Dent, W. R. F., Quanz, S. P., Reggiani, M., & Mayen-Gijon, J. M. 2014, The Astrophysical Journal Letters, 791, L36

- *"A Dwarf Transitional Protoplanetary Disk around XZ Tau B"*
  Osorio, M., **Macías, E.**, Anglada, G., Carrasco-González, C., Galván-Madrid, R., Zapata, L., Calvet, N., Gómez, J. F., Nagel, E., Rodríguez, L. F., Torrelles, J. M., & Zhu, Z. 2016, The Astrophysical Journal Letters, 825, L10

- *"Imaging the Photoevaporating Disk and Radio Jet of GM Aur"*
  Macías, E., Anglada, G., Osorio, M., Calvet, N., Torrelles, J. M., Gómez, J. F., Espaillat, C., Lizano, S., Rodríguez, L. F., Carrasco-González, C., & Zapata, L. 2016, The Astrophysical Journal, 829, 1

- *"Multiple Gaps and a Clumpy Ring in the Pre-Transitional Disk of HD 169142"*
  Macías, E. et al., in preparation

Other publications related to this thesis are:

- *"An Ionized Outflow from AB Aur, a Herbig Ae Star with a Transitional Disk"*
  Rodríguez, L. F., Zapata, L. A., Dzib, S. A., Ortiz-León, G. N., Loinard, L., **Macías, E.**, & Anglada, G. 2014, The Astrophysical Journal Letters, 793, L21

- *"High-Resolution Observations of the Outer Disk around T Chamaleontis: the View from ALMA"*
  Huélamo, N., de Gregorio-Monsalvo, I., **Macías, E.**, Pinte, C., Ireland, M., Tuthill, P., & Lacour, S. 2015, Astronomy & Astrophysics, 575, L5

- *"The VLA View of the HL Tau Disk: Disk Mass, Grain Evolution, and Early Planet Formation"*
  Carrasco-González, C., Henning, T., Chandler, C. J., Linz, H., Pérez, L., Rodríguez, L. F., Galván-Madrid, R., Anglada, G., Birnstiel, T., van Boekel, R., Flock, M., Klahr, H., **Macías, E.**, Menten, K., Osorio, M., Testi, L., Torrelles, J. M., & Zhu, Z. 2016, The Astrophysical Journal Letters, 821, L16

2

Imaging and modeling of the pre-transitional disk of HD 169142

2.1 Introduction

The early stages of planet formation are expected to be identified by signatures of dust evolution in the protoplanetary disks. An outstanding signature is the large (several tens au in diameter) central cavities almost devoid of dust that characterize the so-called transitional disks (Calvet et al. 2005). Some of these transitional disks, dubbed pre-transitional disks, show an important near-IR excess that is interpreted as produced by a residual inner disk inside the cavity (Espaillat et al. 2008).

As discussed in Chapter 1, a number of processes have been proposed to explain the origin of these cavities. Photoevaporative winds can remove material from the inner disk (e.g., Alexander et al. 2006; Suzuki et al. 2010); grain-growth can diminish the dust opacity, decreasing its continuum emission (Dullemond & Dominik 2005); finally, dynamical clearing due to tidal interactions with low-mass companions, either very young brown dwarfs or giant planets on long-period orbits, can produce annular gaps and cavities in the disk (Papaloizou et al. 2007; Zhu et al. 2011). Andrews et al. (2011) favored the last of these mechanisms in their analysis of a sample of 12 such disks. Therefore, transitional and pre-transitional disks are excellent places to search for the youngest planets.

The existence of central cavities (first suggested by Strom et al. 1989) was confirmed from the modeling of the spectral energy distributions (SEDs) and the analysis of Spitzer spectra (e.g., D'Alessio et al. 2006). However, in recent years, it has been possible to image several of these cavities through mm and submm interferometric observations (Brown et al. 2009; Andrews et al. 2011; Isella et al. 2013; Casassus et al. 2013), as well as by high angular resolution polarimetric imaging at infrared wavelengths (e.g., Quanz et al. 2011; Hashimoto et al. 2012; Garufi et al. 2013; Avenhaus et al. 2014).

The disk surrounding the Herbig Ae/Be star HD 169142 ($M_* \simeq 2\ M_\odot$, $d = 145$ pc [1]; Manoj et al. 2006 and references therein) is one of the best targets to study the planetary formation process. Near-infrared polarization images as well as millimeter continuum and CO observations reveal that the disk is nearly face-on, extending up to ∼240 au (e.g., Kuhn et al. 2001; Raman et al. 2006). Its SED characteristics and its relatively strong 7 mm emission suggest that dust has evolved to form big grains (Dent et al. 2006), a prerequisite to planet formation.

Modeling of the SED of HD 169142 suggested the presence of a disk inner cavity with an estimated radius of ∼40 au (Grady et al. 2007) or ∼20 au (Meeus et al. 2010; Honda et al. 2012; Maaskant et al. 2013). These results are supported by recent H-band polarized light images obtained with NACO/VLT (Quanz et al. 2013) that reveal a bright emission ring with a radius of ∼25 au, which is interpreted as the rim of the inner cavity. Additionally, these images reveal the presence of a ∼40-70 au annular gap. However, with these data alone it cannot be unambiguously established whether this gap in polarized emission corresponds to a real gap in surface density, possibly induced by one (or several) forming planet(s), or if it is an illumination effect.

We present Very Large Array (VLA) observations towards HD 169142 that reveal, for the first time, the structure of the dust thermal emission of the disk at radii from

[1] While writting this dissertation, the first data release of the Gaia mission (14-09-2016) provided an improved value of 117 ± 4 pc for the distance to the star HD 169142 (Gaia Collaboration et al. 2016). This is about 20% smaller than the value of 145 pc adopted in the present work. We note that this would result in a linear reduction in the same percentage of the sizes and radii provided here. The effect on the parameters obtained from the modeling is more difficult to estimate since the change in the distance will also affect the adopted stellar properties. Nevertheless, some parameters of the model would actually have opposite effects that could cancel each other. Therefore, we do not expect a significant impact on the results of our model presented in this chapter or in our main conclusions.

Table 2.1. Summary of VLA Observations[a]

Observation Date	Project Code	Array Conf.	Band	Frequency Range (GHz)	Mean Wavelength (mm)	rms Noise[b] (μJy beam^{-1})	Synthesized Beam[b] Size ($''\times''$)	Synthesized Beam[b] PA ($^\circ$)
2012-May-03	12A-439	CnB	Q	42-44	7.0	28	0.51×0.47	50
2012-May-03	12A-439	CnB	C	4.5-6.5	55	12	4.28×3.76	48
2012-Nov-12	12A-439	A	Q	42-44	7.0	25	0.11×0.05	−4
2012-Nov-12	12A-439	A	C	4.5-6.5	55	12	0.85×0.39	−1
2013-Sep-28	13B-260	B	Q	40-48	6.8	17	0.37×0.17	6
2013-Sep-28	13B-260	B	X	8-10	33	13	1.76×0.77	8

[a]Phase center was at α(J2000)=$18^{\rm h}24^{\rm m}29.7790^{\rm s}$, δ(J2000)=$-29^\circ46'49.547''$.

[b]For naturally weighted maps.

∼10 to ∼100 au.

2.2 Observations

Observations were carried out with the Karl G. Jansky VLA of the National Radio Astronomy Observatory (NRAO). We observed the continuum emission in the Q (∼7 mm), C (∼5.5 cm) and X (∼3.3 cm) bands in three different array configurations (CnB, A, and B) (see Table 1). Calibration of the complex gain of the antennas was performed by observing J1820-2528 every 2 minutes. We estimate that the uncertainty in the absolute positions in Q band is $\sim 0.1''$. The flux scale was set by observing 3C286.

Data were calibrated with the CASA (Common Astronomy Software Applications; version 4.1.0) package. For each data set, we ran the VLA Calibration Pipeline provided by the NRAO (version 1.2.0). After inspection of the calibrated data, we performed additional data flagging and re-ran the pipeline when needed.

We produced deconvolved images from each configuration data set, as well as an image combining data from all configurations. All images were obtained with the multi-scale, multi-frequency CLEAN algorithm (Rau & Cornwell 2011) and implemented in the task *clean* of CASA.

2.3 Results

We did not detect any significant emission at C (∼5.5 cm) or at X (∼3.3 cm) bands, with 3-σ upper limits of 36 and 39 μJy beam^{-1}, respectively (Table 1). By extrapolating the X-band upper limit with a spectral index of +0.6, a value typical of free-free emission from thermal radio jets (e.g., Anglada 1996), we expect a free-free contribution at 7 mm of < 0.09 mJy, $< 5\%$ of the observed flux density. Thus, the 7 mm emission reliably traces the thermal dust emission of the disk with negligible free-free contamination.

In Figure 2.1 we show VLA images at 7 mm wavelength of the disk surrounding HD 169142. The source is marginally resolved in the CnB configuration image (Fig. 2.1a), showing that the emission is asymmetric, with the western side being brighter than the eastern side. The source, with a total flux density of 1.8±0.3 mJy, is well resolved in the sensitive (8 GHz bandwidth) B configuration image (Fig. 2.1b) showing a ring of emission of radius $\sim 0.18''$-$0.20''$ ($\sim$ 25-30 au). The width of the ring appears unresolved, even in the E-W direction where the angular resolution is better. The decrease in intensity observed towards the northern and southern edges of the ring is an observational effect, since in these directions the north-south elongated beam intersects a smaller fraction of the ring area.

The center of the emission ring in the B configuration image is located at α(J2000) = $18^{\rm h}24^{\rm m}29.776^{\rm s}$, δ(J2000) = $-29°46'49.87''$, which falls $0.04''$ west and $0.03''$ north of the nominal position of the star HD 169142 in the Tycho-2 catalog, after correction for proper motions to the epoch of the observation. Therefore, the VLA observations indirectly provide an accurate position for the star. In the A configuration images, the emission ring is only marginally detected, after setting a maximum uvrange of ∼1000 kλ. An image obtained from the CnB and A configuration data is presented in Osorio et al. (2014).

The image in Figure 2.1c was obtained by combining the interferometric visibilities from the CnB, B, and A configurations. To correct for residual differences in absolute positions due to phase errors and proper motions, the data from the A and B configurations were aligned (within $<0.05''$) by matching the centers of the rings fitted to the individual images before being combined. For the CnB data, obtained with a larger beam, a precise alignment was considered unnecessary. The final image

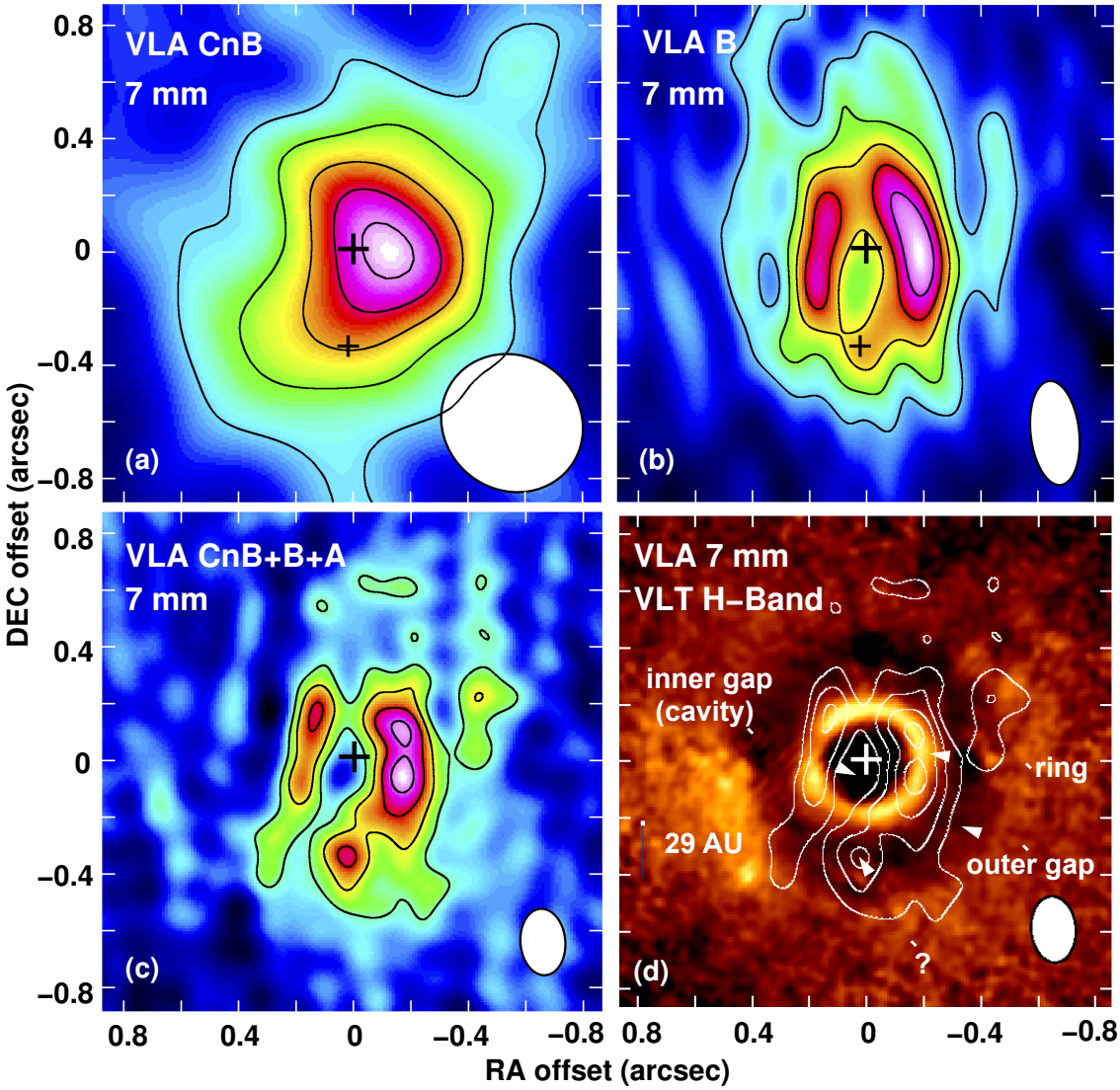

Figure 2.1 VLA images of the 7 mm dust thermal emission in several array configurations. Panels *(a)* and *(b)* show, respectively, the CnB and B configuration images. Panel *(c)* shows the image obtained by combining the CnB, B, and A configuration visibilities with a uvrange <1500 kλ (rms=18 μJy beam^{-1}; beam=0.23″ × 0.16″, PA=5°). Panel *(d)* shows an overlay of the image shown in panel *(c)* (contours) and the VLT/NACO H-band (1.6 μm) polarized light image from Quanz et al. (2013) (color-scale). Saturated pixels in the central region of the H-band image have been masked out. In all panels, contour levels are −3, 3, 5, 7, 9, and 11 times the rms. Synthesized beams are plotted in the lower-right corners. The apparent decrease of the 7 mm emission in the north and south edges of the source is most probably a consequence of the elongated beam. The larger cross marks the position of the HD 169142 star and the smaller one that of the protoplanet candidate.

shows the same general structure as the one seen with the B-array data alone, but with better detail.

2.3.1 The emission ring and the inner cavity/gap

One of the outstanding features of the HD 169142 disk images is the ring of enhanced emission of radius ∼25-30 au. We interpret this ring as the rim of an inner cavity or gap possibly created in the disk by a planet or a substellar companion. Figure 2.1d shows an overlay of the VLA image from Figure 2.1c and the H-band polarized light image of Quanz et al. (2013). The cavity is suggested by the decrease of emission near the inner edge of the ring in the IR image, but it cannot be traced towards the center because the central pixels are saturated. Nevertheless, this inner cavity is clearly seen in the 7 mm images (Figs. 2.1b, c, d), confirming HD 169142 as a transitional or pre-transitional disk. Interestingly, the size of the cavity in the IR image, which traces scattered light from small (micron-sized) dust grains, coincides with that in the 7 mm image, which traces larger (mm/cm-sized) dust grains. This is in contrast with other sources where the size of the cavity changes with the observed wavelength (see Garufi et al. 2013 and references therein).

The 7 mm emission ring appears significantly asymmetric (in the B-configuration image, the flux densities of the western and eastern halves of the ring are 630±105 mJy and 361±78 mJy, respectively, without overlapping of the quoted 99% confidence intervals). This azimuthal asymmetry is reminiscent of the lopsided rings that are expected to be produced at long wavelengths as a consequence of azimuthal accumulation (trapping) of large dust grains, as predicted by theoretical models (e.g., Birnstiel et al. 2013) and revealed by ALMA observations of more extreme asymmetries in sources such as Oph IRS 48 (van der Marel et al. 2013) and HD 142527 (Casassus et al. 2013). In near-IR scattered light the emission ring of HD 169142 is more symmetric but shows a dip at PA $\simeq 80^\circ$ (Quanz et al. 2013), and perhaps a second dip at PA $\simeq 150^\circ$ (Fig. 2.1c), both in the eastern side, where the 7 mm emission is weaker.

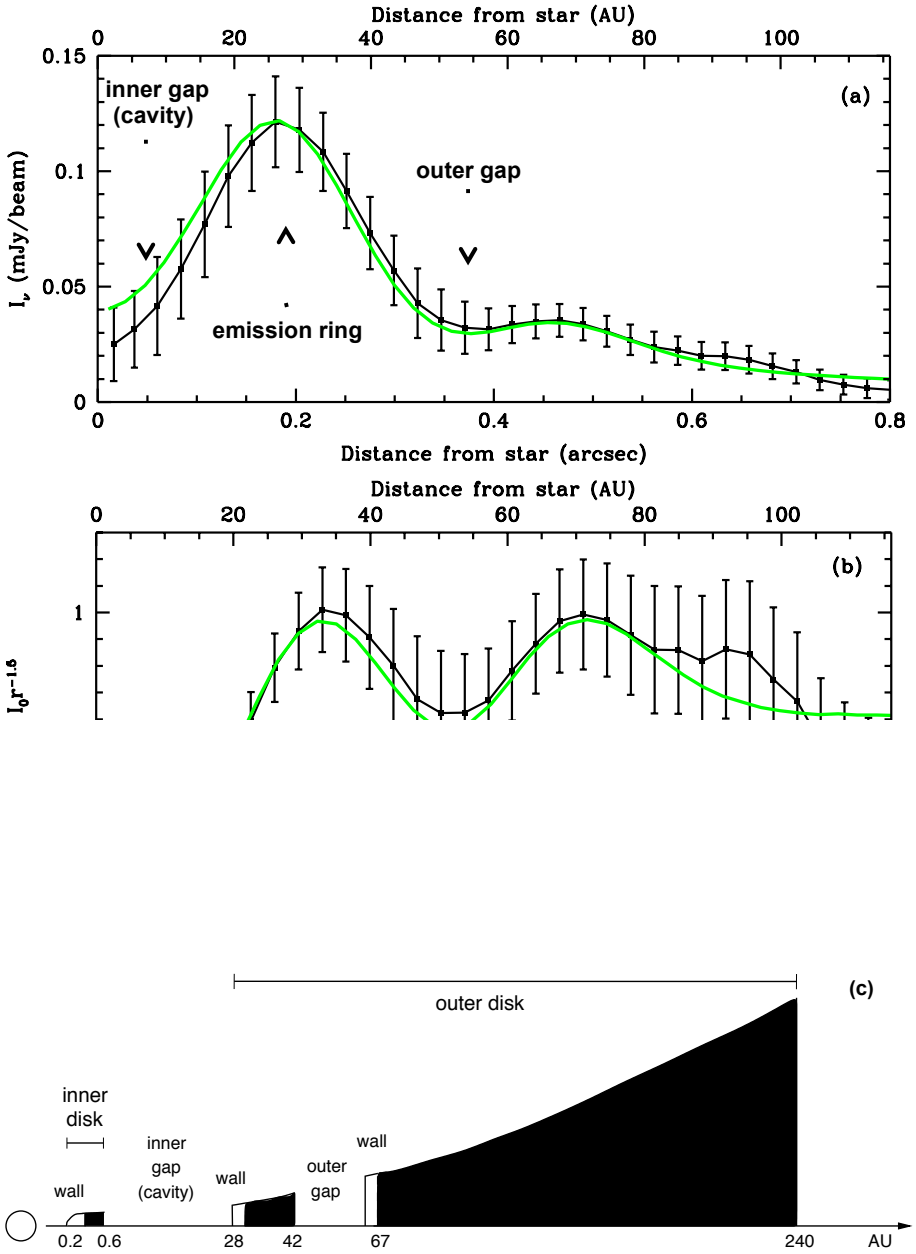

Figure 2.2 (a) Observed (dots and black solid line with error bars) and model (green solid line) azimuthally averaged intensity profile of the images shown in Fig. 2.1c and in Fig. 2.3b, respectively. Error bars in the observed profile are obtained from the rms of the pixels in the annuli corrected by the number of uncorrelated pixels. (b) Same as (a), but normalized by a power-law fit. (c) Sketch of the disk structure above the mid-plane.

2.3.2 The outer annular gap

Quanz et al. (2013) reported the presence of an annular gap in the IR polarized light of the disk of HD 169142 in the range of radii ∼40-70 au. This gap in scattered light may be due to a real decrease in the disk surface density, which could be induced by a protoplanet, or may be due to shadowing or other illumination effect that decreases the polarized light. Our 7 mm observations, tracing optically thin thermal emission of the large dust grains, could provide a better determination of the real nature of this gap. However, the 7 mm emission is weak at $\gtrsim$40 au from the center. To improve the signal to noise ratio at large radii, we have calculated the radial intensity profile, shown in Figure 2.2a, averaging the emission over concentric rings in Figure 2.1c. To highlight the outer gap and its radial location, Figure 2.2b shows the same profile but normalized by a power-law fit to compensate for the radial intensity decrease. In the azimuthal averaging we have excluded PAs near $\sim 180°$, where there is a knot of emission that may be an independent component (see below). The radial intensity profile shows that the outer gap, as well as the inner cavity and the bright ring, are found at the same radii as the corresponding features in the IR profile (Fig. 2 in Quanz et al. 2013), suggesting that they represent the true dust distribution.

An additional interesting feature observed in our 7 mm VLA images is the knot of emission located $\sim 0.34''$ (∼50 au) to the south (PA $\simeq 175°$) of the central star. This emission appears smeared out in the B configuration image (Fig. 2.1b) but is better defined in the image that combines all configurations (Fig. 2.1c). This compact source falls in the middle of the outer annular gap, and we speculate that it could trace circumplanetary dust emission associated with the protoplanet responsible for creating this gap. We estimate for this knot a flux density of ∼100 μJy above the background (∼5-σ). Assuming a temperature of ∼50 K and a 7 mm opacity of 2×10^{-3} cm^{-2} g^{-1}, as suggested by the SED modeling (section 4), we obtain a total (dust+gas) mass of 0.6 M_J. This mass estimate is uncertain, since in the proximity of gaps the size of dust grains and the dust-to-gas ratio are expected to change with time and planet mass (Pinilla, Benisty & Birnstiel 2012). If the 7 mm source is associated with a protoplanet, its expected orbital period (∼186 yr) would produce proper motions detectable in a few years, providing an unambiguous way to test this hypothesis.

2.4 Disk model

HD 169142 has been observed from ultraviolet to radio wavelengths. Figure 2.3a shows the photometric data points compiled from the literature and from this paper. Our model includes the contribution of the central star (whose adopted parameters are given in Table 2) and the disk. As suggested by the observations (Quanz et al. 2013; this paper) the disk has a central cavity of radius ∼30 au and a gap spanning ∼40-70 au. We find that a central hot component is required to fit the 2-10 μm range of the SED. A central dust component was also inferred from the modeling of Honda et al. (2012) and Maaskant et al. (2013), who postulate the presence of a central dust halo. However, we find that the emission can be naturally explained by a small residual inner disk and its hot wall (located where dust reaches its sublimation temperature). With this residual inner dust, the disk of HD 169142 should be classified as pre-transitional (as defined by Espaillat et al. 2008), implying that the observed central cavity is actually a gap between the inner and outer parts of the disk (see sketch in Fig. 2.2c).

The contribution of the disk is obtained using the irradiated α-accretion disk models with dust settling developed by D'Alessio et al. (1999, 2001, 2006). In these models, the radial and vertical physical structure of the disk, and the emerging intensity are self-consistently calculated. Since HD 169142 is a very well studied object, most of the parameters of the model are determined by previous observations; other are pretty well constrained, and only small fine-tuning adjustments were required (see Table 2 and references therein). The main free parameters of the model are the viscosity and the dust properties. A low value of the viscosity parameter is required to account for both the low mass accretion rate and the high surface densities (suggested by the relatively strong mm/submm flux densities), as in α-disks the viscosity parameter is proportional to the mass accretion rate and inversely proportional to the surface density.

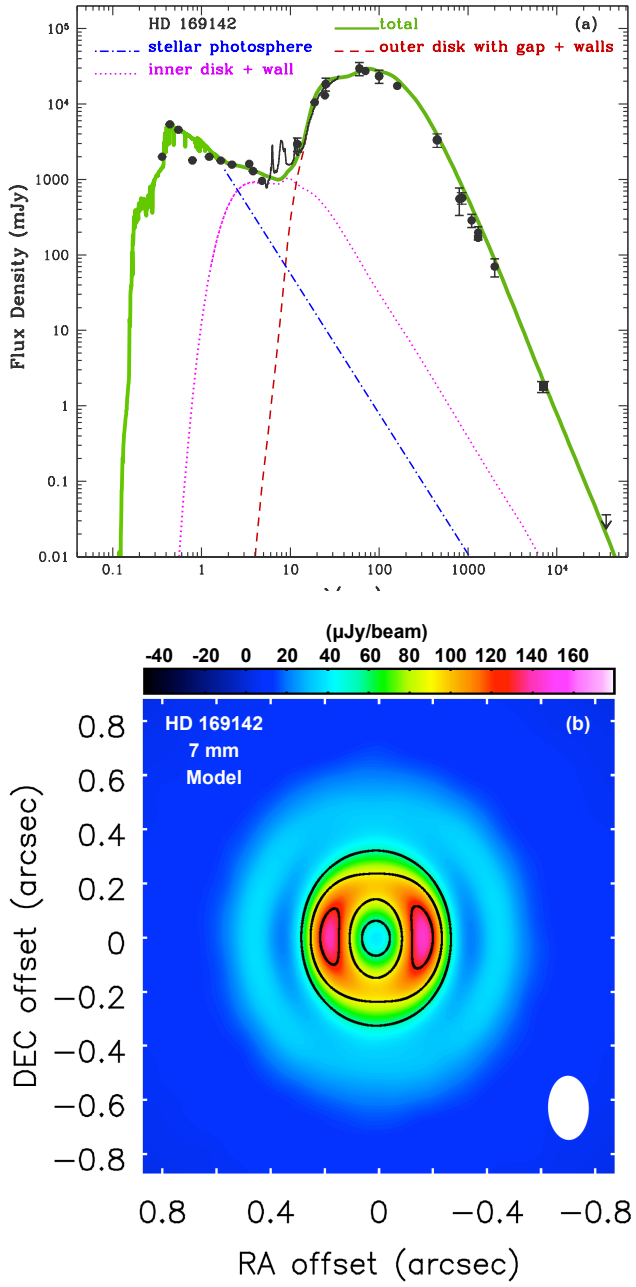

Figure 2.3 (a) Observed (points) and model (lines) SEDs of the HD 169142 protoplanetary disk. The thick solid line is the total SED, including the contribution of all the components. Data points are from the compilation of Dent et al. 2006, from Raman et al. 2006, Honda et al. 2012, Meeus et al. 2010, Sandell et al. 2011, Dempsey et al. 2013, and this paper. (b) CASA simulated image at 7 mm for the disk model, as it would be observed by combining the VLA CnB, B, and A configurations. Contours and color scale are as in Fig. 2.1c.

Table 2.2. Physical Parameters of HD 169142 and its Disk

Parameter	Value	Notes	Refs.
Stellar Properties			
Distance (pc)	145	Adopted	1
A_V (mag)	0.5	Adopted	2
Age (Myr)	5.4	Adopted	1
Effective Temperature (K)	8100	Adopted	1
Radius ($R_\odot$)	2.2	Adopted	1
Mass ($M_\odot$)	2	Adopted	1
Inner Disk[a]			
Inner Radius (au)	0.5	Fitted	
Outer Radius (au)	0.6	Fitted	
Mass ($M_\odot$)	2.6×10^{-5}	Calculated	
Wall of the Inner Disk			
Location (au)	0.2-0.5	Calculated	
Temperature (K)	1300-1000	Calculated	
Height (au)	0-0.05	Calculated	
Outer Disk			
Inclination Angle (deg)	13	Adopted	3
Position Angle (deg)	5	Adopted	3
Inner Radius (au)	28	Adopted/Refined	4, 5
Outer Radius (au)	240	Adopted	3
Gap Inner Radius (au)	42	Adopted/Refined	4, 5
Gap Outer Radius (au)	67	Adopted/Refined	4, 5
Mass Accretion Rate ($M_\odot$ yr^{-1})	3×10^{-9}	Adopted/Refined	6
Viscosity Coefficient	0.0005	Fitted	
Degree of Settling	0.5	Fitted	
Mass ($M_\odot$)	0.12	Calculated	

Table 2.2 (cont'd)

Parameter	Value	Notes	Refs.
Outer Wall of the Inner Gap			
Location (au)	28	Adopted/Refined	4, 5
Height (au)	9	Calculated	
Illuminated Fraction (%)	66	Calculated	
Temperature of Illuminated Part (K)	110	Calculated	
Outer Wall of the Outer Gap			
Location (au)	67	Adopted/Refined	4, 5
Height (au)	26	Calculated	
Illuminated Fraction (%)	10	Calculated	
Temperature of Illuminated Part (K)	70	Calculated	

[a]The mass accretion rate, viscosity coefficient, inclination, and grain properties are equal to those of the outer disk. The size is constrained by the 7 mm intensity upper limit towards the center.

References. — (1) Manoj et al. 2006; (2) Dent et al. 2006; (3) Raman et al. 2006; (4) Quanz et al. 2013; (5) This paper; (6) Grady et al. 2007.

The dust is assumed to consist of two populations of grains (each with an $n(a) \propto a^{-3.5}$ size distribution) that are vertically distributed as a function of the degree of settling of large grains from the upper layers (see Appendix A). The grain sizes are constrained mainly by the data at wavelengths >100 μm. Grains in the disk upper layers have radii ranging from 0.005 μm to 1 μm, while the radii of the grains settled in the disk mid-plane range from 5 μm to 1 mm. The dust-grain mixture assumed to compute the opacity consists of silicates and graphite, with mass fractional abundances relative to gas of 0.004 and 0.0025, respectively (e.g., McClure et al. 2013).

The inner disk sublimation wall has a curved shape that depends on density and grain settling, and is calculated following Nagel et al. (2013) and D'Alessio et al. (2006). For the gaps and their walls we use a simpler treatment (see, e.g., Jang-Condell & Turner 2012 for a more accurate treatment). The gaps are modeled as

annular regions completely devoid of dust with cylindrical walls whose scale height is predicted by the accretion disk model. The wall radii are obtained approximately from the observed images (Quanz et al. 2013; this paper) and refined (within $\sim \pm 1$ au) by fitting the SED and the 7 mm intensity profile.

The emission of the outer walls of the gaps is computed as a modified blackbody (D'Alessio et al. 2005), but taking into account the extinction by the disk. Thus, at short wavelengths, the disk will be optically thick and just half of the inner face of the wall will be visible. At 7 mm, however, the disk will be optically thin so we will be detecting the whole wall. Walls are assumed to be unresolved in the radial direction, with a width smaller than the pixel scale ($\sim$1 au). Because of shadowing, only the upper portion (composed of small dust grains) of these walls is frontally irradiated by the star, and is heated at a temperature close to the equilibrium temperature, which is calculated following Nagel et al. (2013). The contribution of the shadowed portion of the walls (at lower temperatures, defined by the disk structure) is relevant in the 7 mm intensity profile. This emission is dominated by the large dust grains (close to the disk mid-plane) that accumulate near the outer edges of the gaps because of dust filtration. To simulate this effect, in these walls we increased the dust-to-gas ratio by a factor of $\sim$3, and the scale height of the large dust grain population up to 60% of the local gas-pressure scale height. These two parameters are determined mainly by fitting the 7 mm intensity profile.

The main parameters of our favored model are given in Table 2. Figure 2.3a shows that the model reproduces the observed SED satisfactorily. Figure 2.3b shows a CASA simulated image of the 7 mm model emission that agrees in shape, size, and intensity with the observed image (Fig. 2.1c). Figures 2.2a and 2.2b show a quantitative comparison of the radial intensity profiles of both images, showing that model and observations are in good agreement. We note that the observed disk emission decreases beyond $\sim$ 100 au, falling below the predicted emission by our model. This difference is probably due to the radial migration of large dust grains in the disk. We have started to include this effect in our model (see Appendix A), although for this study we decided to use a simpler model. The contribution of the hot inner disk and its wall (dominant in the 2-10 μm range), remain below the detectability limits at 7 mm, as expected. Very sensitive high angular resolution observations at mm/submm wavelengths are necessary to directly confirm the presence of this disk component.

The simulated model image (Fig. 2.3b) appears symmetric with respect to the beam axis. Subtraction from the observed one shows a residual emission excess in the western side, indicating that the east-west asymmetry in the observed images (Fig. 2.1) cannot be attributed to opacity effects and should have a different origin, such as a dust trap.

As noted above, most of the physical structure of the HD 169142 disk is self-consistently modeled and constrained by the observations. However, the gaps and walls arising from the tidal interactions of the disk with companions, and the subsequent radial and azimuthal gradients of the gas-to-dust ratio, are not self-consistently integrated. Model improvements should come from including azimuthal asymmetries and dust migration.

2.5 Summary and conclusions

We performed Very Large Array observations at 7 mm that trace the thermal emission of large dust grains in the HD 169142 protoplanetary disk. In addition, we have modeled the broad-band spectral energy distribution and the 7 mm images to constrain the disk physical structure.

Our images show a ring of enhanced emission of radius ∼25-30 au, whose inner region is devoid of detectable 7 mm emission. We interpret this ring as tracing the rim of an inner cavity or gap, possibly created by a planet or a substellar companion. The ring appears asymmetric, with the western part significantly brighter than the eastern one. This azimuthal asymmetry is reminiscent of the lopsided structures that are expected to be produced as a consequence of trapping of large dust grains.

Our observations also reveal an outer annular gap at radii from ∼40 to ∼70 au. Unlike other sources, the radii of the inner cavity, the ring, and the outer gap observed in the 7 mm images, which trace preferentially the distribution of large (mm/cm sized) dust grains, coincide with those obtained from a previous near-infrared polarimetric image, which traces scattered light from small (micron-sized) dust grains.

From our modeling we infer the presence of a small (radius ∼0.6 au) residual disk inside the central cavity, indicating that the HD 169142 disk is a pre-transitional disk. The distribution of dust in three annuli with gaps in between them suggests that the disk in HD 169142 is being disrupted by at least two planets or substellar objects.

Actually, Reggiani et al. (2014) reported 3.8 μm observations revealing the presence of a low-mass companion in the inner gap of the disk, at a separation of $\sim$23 au.

3

Small scale structure in the inner and outer regions of the pre-transitional disk of HD 169142

3.1 Introduction

As mentioned above, transitional disks, which are protoplanetary disks with central gaps or cavities (Strom et al. 1989; Calvet et al. 2005; Espaillat et al. 2007), appear as great candidates to look for signs of ongoing planetary formation. Even though some of them might have cavities which are consistent with a photoevaporation origin (Alexander et al. 2014), observations seem to indicate that most cavities in transitional disks are created by dynamical interactions with low-mass orbiting companions such as planets or substellar objects (Andrews et al. 2011; Espaillat et al. 2014).

Until recent years, (sub-)mm observations lacked the sensitivity and angular resolution necessary to study the distribution of the emission up to distances very close to the central star. With the outstanding angular resolution provided by the most extended baselines of ALMA, as well as with the new capabilities of the Karl G. Jansky VLA, it is now possible to attempt this type of studies. In particular, recent ALMA observations have revealed the presence of very small central cavities, few au in size, in some transitional disks (e.g., TW Hya: Andrews et al. 2016; XZ Tau B:

Osorio et al. 2016; see Chapter 4). On the other hand, some studies have been able to detect compact central emission in transitional disks that has been associated with a residual inner disk of dust or with free-free emission from ionized gas (Isella et al. 2014; Rodríguez et al. 2014; Andrews et al. 2016).

Additionally, (sub-)mm ALMA observations have also revealed the presence of several gaps and rings up to distances of ~ 90 au from the star in the protoplanetary disk around HL Tau (ALMA Partnership et al. 2015a). These gaps, however, might have a different origin to those observed at the inner regions of transitional disks. The young age of HL Tau, as well as the fact that some gaps are very narrow and appear at very long distances from the star, have lead to question whether a planet could produce this type of gaps. This has resulted in a number of studies proposing new physical processes that could create similar gap structures – e.g. zonal flows in magnetized disks (Bai & Stone 2014), magneto-rotational instability at the dead zone outer edge (Flock et al. 2015), sintering-induced gaps and rings (Okuzumi et al. 2016), or grain growth close to snow lines in the disk (Ros & Johansen 2013; Zhang et al. 2015; see Chapter 1 for a more in detail explanation of all these processes). Gaps produced by these mechanisms could also be present in older transitional disks, but they would have remained unnoticed in previous (sub-)mm observations due to a lack of sensitivity and angular resolution. In fact, recent ALMA observations, with a similar angular resolution to the HL Tau observations, have revealed the presence of a similar ringed substructure in the transitional disk of TW Hya (Andrews et al. 2016). Therefore, more observations of protoplanetary disks are needed, firstly to find out whether multi-gap structures are ubiquitous in protoplanetary disks, and secondly to identify the physical mechanisms responsible for their creation.

As explained in Chapter 2, HD 169142 is a Herbig Ae/Be star ($M_\star \simeq 1.65$–2 $M_\odot$, age ~ 5–11 Myr, $d \simeq 145$ pc[1]; Blondel & Djie 2006; Manoj et al. 2006) surrounded by

[1]While writting this dissertation, the first data release of the Gaia mission (14-09-2016) provided an improved value of 117 ± 4 pc for the distance to the star HD 169142 (Gaia Collaboration et al. 2016). This is about 20% smaller than the value of 145 pc adopted in the present work. We note that this would result in a linear reduction in the same percentage of the sizes and radii provided here. The effect on the parameters obtained from the modeling is more difficult to estimate since the change in the distance will also affect the adopted stellar properties. Nevertheless, some parameters of the model would actually have opposite effects that could cancel each other. Therefore, we do not expect a significant impact on the results of our model presented in this chapter or in our main conclusions.

an almost face-on ($i \simeq 13°$; Raman et al. 2006) pre-transitional disk (see Chapter 2; Osorio et al. 2014). Our previous Very Large Array (VLA) observations at 7 mm (see Chapter 2; Osorio et al. 2014) detected a bright ring of emission at a radius of ∼25–30 au and a second gap from ∼ 40 to ∼ 70 au, coincident with the results from *H* band polarized scattered light images (Quanz et al. 2013; Momose et al. 2015). The ring of emission showed an azimuthally asymmetric morphology at 7 mm, reminiscent of the lopsided morphology produced as a consequence of dust trapping in planet-induced vortices (Birnstiel, Dullemond & Pinilla 2013). In addition, the fact that both gaps were detected at 7 mm as well as in the scattered light images indicates that they are tracing real decreases of the dust surface density in the disk. We reproduced the SED and 7 mm radial intensity profile of HD 169142 with a disk model that included the two observed gaps. Our results suggested that planet formation is the most likely origin for both detected gaps. In fact, a substellar or planetary companion candidate has been detected within the inner gap of the disk (Biller et al. 2014; Reggiani et al. 2014), which supports a planet-induced origin for this gap.

In this chapter we present new high angular resolution VLA observations at 7 mm, 9 mm, and 3 cm toward the pre-transitional disk around HD 169142, revealing the presence of a new third gap in the disk as well as a free-free thermal emission source inside the inner gap.

3.2 Observations

Our observations were performed using the VLA of the National Radio Astronomy Observatory (NRAO) in the A and BnA configurations at Q (∼7 mm), Ka (∼9 mm), and X (∼3 cm) bands. Archival observations at K (∼1.3 cm; C and DnC configurations) and C band (∼5 cm; A configuration) were also used (see Table 5.1). Amplitude calibration was performed by observing 3C286, with an expected uncertainty in the flux scale of ∼ 10%. 3C286 was also used as the bandpass and delay calibrator, whereas J1820-2528 was used as the complex gain calibrator.

The observations were reduced and calibrated with the reduction package Common Astronomy Software Applications (CASA; version 4.5.3)[2]. Each data set was processed through the VLA calibration pipeline integrated within CASA. After each

[2]https://science.nrao.edu/facilities/vla/data-processing

Table 3.1. VLA observations

Band	Central Frequency (GHz)	Bandwidth (GHz)	Array Conf.	Observation Date	Project Code	On-source time (min)
Q	44	8	A	2014-Mar-06	14A-496	63.9
				2014-Mar-04		63.9
				2014-Feb-27		63.9
Q	44	8	BnA	2014-Jan-25	13B-260	72.0
Q	44	8	B	2013-Sep-28[a]	13B-260	72.0
Ka	33	8	A	2014-Feb-25	14A-496	45.4
K	21	2	C	2012-Jan-29	AC982	6.0
			DnC	2010-Sep-30		6.0
X	8	4	A	2014-Mar-06	14A-496	15.3
				2014-Mar-04		15.3
				2014-Feb-27		46.0
				2014-Feb-25		15.3
X	8	4	BnA	2014-Jan-25	13B-260	7.3
X	8	4	B	2013-Sep-28[a]	13B-260	7.3
C	5.5	2	A	2012-Dec-23	12A-439	8.0
				2012-Nov-12[a]		8.0

[a] Data reported in Chapter 2 (Osorio et al. 2014).

run of the pipeline the calibrated data were inspected. Then, we performed additional data flagging and re-ran the pipeline as many times as needed.

Deconvolved images were produced with the CLEAN task of CASA. A multi-scale multi-frequency deconvolution algorithm was used to take into account the frequency dependence of the emission within each band (Rau & Cornwell 2011). Data from each observing session were first imaged independently to check for possible errors in the absolute position, without finding any significant shift. Then, for each band, we combined the data from the different epochs and configurations in order to obtain higher sensitivity images. A *uvtaper*, equivalent in the image domain to a convolution with a beam= $0\farcs1 \times 0\farcs01$ (PA= 90°), was used for the Ka band data in order to improve the quality of the image.

3.3 Results and discussion

A natural-weighted image of the 7 mm emission of HD 169142, obtained from the combination of A, BnA, and B configuration data, is shown in Figure 5.3. The image shows a narrow ring of emission of radius $\sim$ 32 au with significant substructure. In addition, the image shows a hint of a second ring of emission at $\sim$ 70 au tracing the rim of the second gap. A compact component of emission is detected inside the inner ring, with its peak of emission displaced a projected distance of $\sim$ 4 au from its center[3]. Our new data, with higher sensitivity and angular resolution, do not confirm the presence of the protoplanet candidate inside the second gap that was suggested by our previous images (see Chapter 2; Osorio et al. 2014). The total flux density of the 7 mm emission is 2.0 ± 0.4 mJy, which is consistent with our previous measurements. The flux density of the central component is 74 ± 15 μJy.

Figure 3.3a presents the 9 mm image of HD 169142. This image shows a similar morphology to the 7 mm image: a ring of emission with a central source inside its cavity. The ring of emission also seems to show some substructure, although the low signal to noise ratio makes it difficult to determine whether this substructure is real

[3]The central component of emission is only detected in the A configuration data, which have enough angular resolution and sensitivity to separate it from the ring of emission. We do not expect significant proper motions within the time span of the A configuration observations (one week). Thus, we expect that our images obtained combining the A, BnA and B configuration data will not be affected by these proper motions.

or due to rms fluctuations. The total flux density of the source is 850 ± 150 μJy, while the flux density of the central emission inside the cavity is 45 ± 14 μJy.

Figure 3.3b shows an image of the 3 cm emission of HD 169142, obtained by combining the A, BnA, and B configuration observations using natural weighting. The emission is only marginally resolved, with its peak of emission located inside the inner dust gap, very close to the central star. The total flux density at 3 cm is 50 ± 10 μJy. By using robust weighting, the emission is partially resolved into a compact component located close to the position of the star and some emission extending outside the inner gap. From the intensity peak of the central component we estimate that its flux density at 3 cm is $\sim 20 \pm 5$ μJy. The remaining emission at 3 cm would be consistent with the dust flux density of ~ 30 μJy predicted by our model at 3 cm (see Chapter 2; Osorio et al. 2014).

Finally, no emission was detected in the K and C band observations, with 3σ upper limits of 420 μJy beam^{-1} and 27 μJy beam^{-1}, respectively. The C band image was obtained by combining our new data with data reported in Chapter 2 in order to obtain a tighter upper limit. Both limits are consistent with our model.

3.3.1 Narrow ring

As can be seen in Figure 5.3, our 7 mm image shows a narrow ring of emission with a central radius of ~ 32 au. We estimate a deconvolved FWHM of ~ 10 au, measured along the E-W direction, where the synthesized beam size is smaller. The ring in our images coincides quite well with the ring detected in near-IR images (Quanz et al. 2013), and in our previous 7 mm observations (see Chapter 2; Osorio et al. 2014). The center of the ring in the 7 mm image (epoch ~ 2014.17) is located at α(J2000) = $18^{\rm h}24^{\rm m}29\overset{\rm s}{.}778$, δ(J2000) = $-29°46'49\overset{''}{.}87$, which coincides almost perfectly ($\lesssim 8$ mas) with the position of the star HD 169142 given in the Gaia catalog, after correcting for proper motions (Gaia Collaboration et al. 2016). The 9 mm emission shows a morphology consistent with the 7 mm image (see Fig. 3.3a).

As noted in Chapter 2, the intensity of the ring is significantly asymmetric in azimuth at 7 mm, showing a knot of emission ~ 4 σ above the average intensity of the ring at PA$\simeq -40°$. We think that this knot represents a real azimuthal asymmetry since an intensity enhancement appears both in the images made from the new A

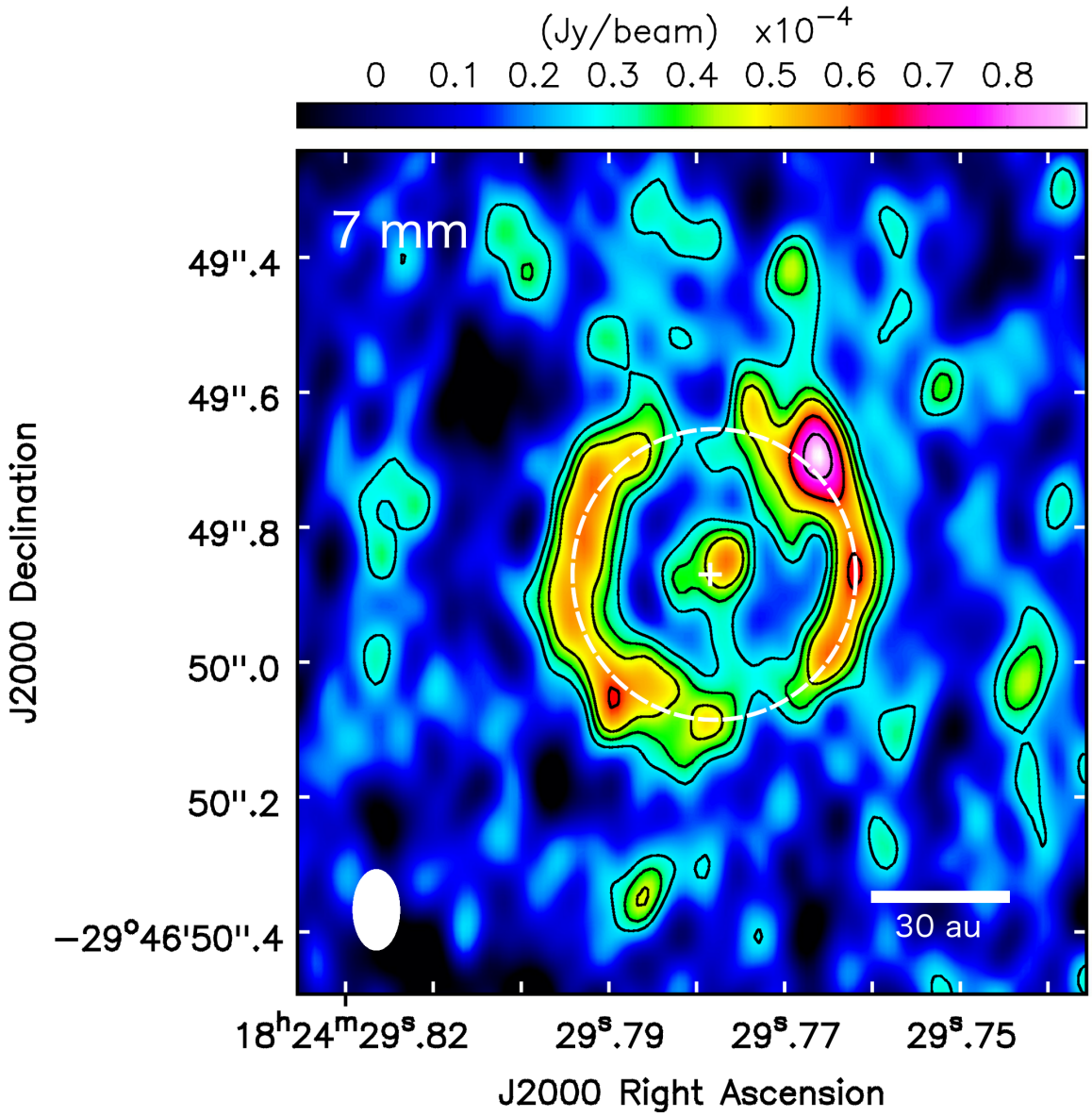

Figure 3.1 Natural-weighted VLA image at 7 mm of the transitional disk around HD 169142 (synthesized beam=0.″12 × 0.″07, PA=0°; shown in the lower-left corner). Contour levels are −3, 3, 4, 5, 7, and 9 times the rms of the map, 9.0 μJy beam^{-1}. A dashed circle is drawn for reference, indicating the position of the 7 mm dust ring. The white cross indicates the position of the center of the ring.

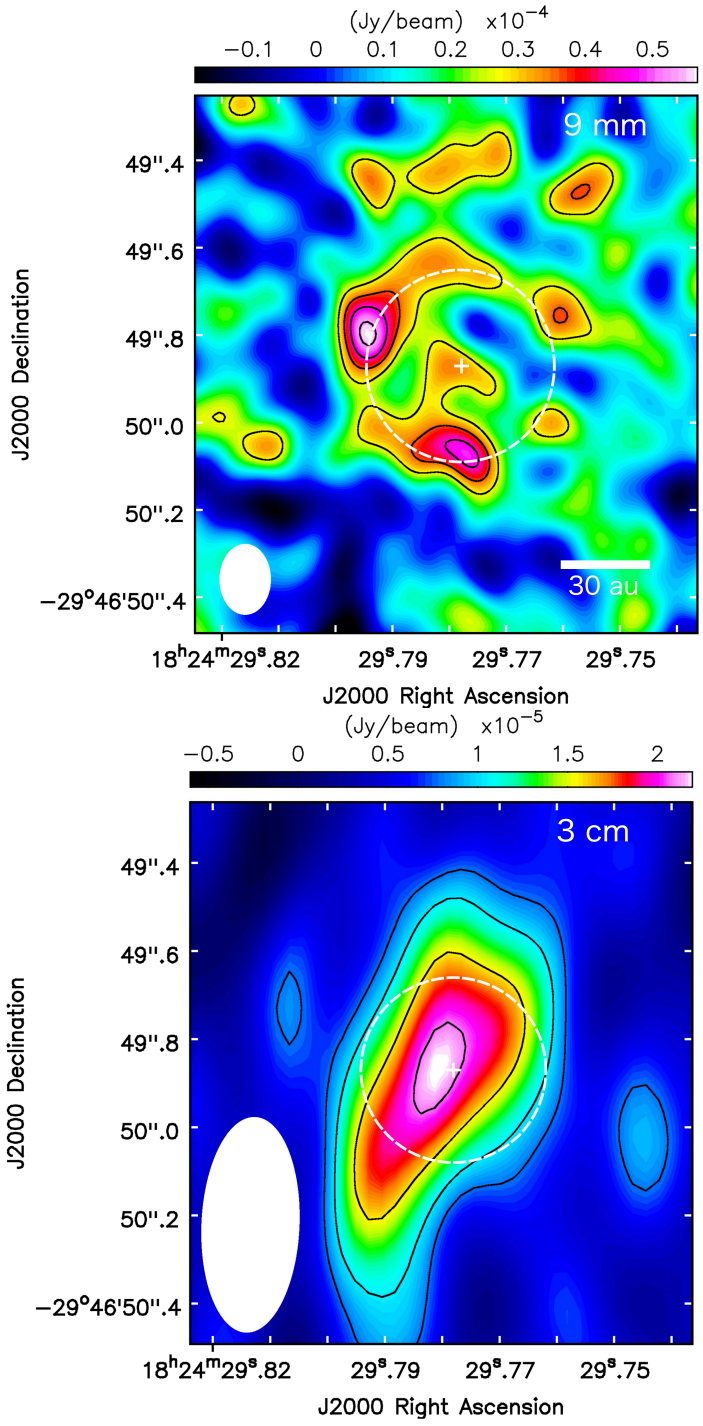

Figure 3.2 Top panel: Natural-weighted VLA image of the 9 mm emission (synthesized beam=0.″16 × 0.″12, PA=0°; shown in the lower-left corner). Contour levels are −3, 3, 4, 5, 7, and 9 times the rms of the map, 9.0 μJy beam^{-1}. Bottom panel: Natural-weighted VLA image of the 3 cm emission (synthesized beam=0.″49 × 0.″22, PA=−2.5°; shown in the lower-left corner). Contour levels are −3, 3, 4, 6, and 8 times the rms of the map, 2.6 μJy beam^{-1}. In both panels a dashed circle is drawn for reference, indicating the position of the 7 mm dust ring as shown in Figure 5.3. The white cross indicates the position of the center of this ring.

configuration data alone as well as in the lower angular resolution maps reported in Chapter 2. We note that a brightness increase is detected at similar PAs in the scattered light images presented by (Momose et al. 2015). On the other hand, our new 7 mm images also show significant decreases of intensity or dips in the ring at PA$\simeq 0°$ and PA$\simeq -170°$. Our previous 7 mm observations also showed a hint of the presence of dips in the ring (see Fig. 2.1), but the larger and elongated beam along the N-S direction impeded to distinguish between a real dip from an observational effect. Even though the synthesized beam of our new images is still elongated along the same direction, its much smaller size could not produce such a decrease of intensity in an axisymmetric ring.

Polarized scattered light images at H band show a nearly axisymmetric ring with only a possible dip at a PA$\simeq 80°$ (Quanz et al. 2013), where no significant drop of emission is seen in our images. The fact that neither the knot nor the dips of emission in the disk are present at near-IR wavelengths indicates that they are probably produced by azimuthal asymmetries in the disk mid-plane density, to which our 7 mm images are more sensitive, without affecting significantly the distribution of small dust grains in the disk atmosphere, which are traced by the scattered light images.

Azimuthal asymmetries in the large dust grains distribution are expected to be produced by tidal interactions between a forming planet and the disk (Baruteau et al. 2014). Hydrodynamic simulations show that planets can create relatively large cavities with vortexes at their outer edges. These vortexes, in turn, are able to trap the large dust grains in their pressure maxima, producing lopsided asymmetries at mm wavelengths (Birnstiel, Dullemond & Pinilla 2013; Zhu & Stone 2014) that could correspond to the non-axisymmetric morphology seen in our images.

However, at 7 mm the ring not only shows a knot of emission but also two dips, which suggests that the ring might be undergoing a fragmentation process. We speculate that the interaction between the disk of HD 169142 and the possible forming planets at the inner and second gaps may have resulted in a pile up of material in the ring, which may have produced a gravitationally unstable ring. Because of the ring fragmentation, a new protoplanet could end up being formed in the detected knot, in a similar process to what has been suggested by Carrasco-González et al. (2016) for a clump of emission detected in HL Tau.

3.3.2 Emission inside the inner gap

Our 7 mm, 9 mm, and 3 cm images have revealed the presence of compact emission located inside the inner dust gap. The emission at 7 mm is slightly extended along the E-W direction, with its intensity peak at a projected distance of ~ 4 au ($\sim 0\farcs03$) from the central star toward the W direction. The insufficient quality of the images at 9 mm and 3 cm makes it difficult to estimate the morphology of the emission at these wavelengths. This central emission could not be detected by our previous observations at 7 mm due to the lack of angular resolution (see Chapter 2; Osorio et al. 2014).

In principle, both dust and ionized gas could be contributing to the radio emission at the innermost regions of transitional disks. To our knowledge, very few transitional disks have been observed with high enough angular resolution to detect and resolve compact emission inside their central cavities or gaps. LkCa 15 (Isella et al. 2014) and AB Aur (Rodríguez et al. 2014) were imaged with the VLA at 7 mm and 3 cm, respectively, whereas TW Hya was observed with ALMA at 0.87 mm (Andrews et al. 2016). The emission in TW Hya is associated with inner residual dust located close to the star. The morphology and frequency dependence of the emission in AB Aur indicates that it is associated with free-free emission from an accretion-driven jet. In LkCa 15, however, the lack of observations at other wavelengths prevents from distinguishing between a dust or a free-free origin for the emission. In the following we discuss the origin of the observed compact central emission in HD 169142.

The near-IR excess in the SED of HD 169142 indicates that its disk is a pre-transitional disk, with a hot dust component located very close to the star. As discussed in Chapter 2, we modeled the broadband SED as well as 7 mm images of HD 169142 and found that an inner disk 0.6 au in radius, together with its inner wall at the dust sublimation radius (~ 0.2 au), could fit the near-IR emission of HD 169142. According to our model, this inner dust component would produce only ~ 9 μJy, ~ 5 μJy and < 1 μJy of emission at 7 mm, 9 mm, and 3 cm, respectively. These values are much lower than the observed 74 ± 15 μJy, 45 ± 14 μJy and $\sim 20 \pm 5$ μJy at these wavelengths for the central component. From a power-law fit to these observed values of the flux density ($S_\nu \propto \nu^\alpha$), we estimate a spectral index of $\alpha = 0.87 \pm 0.16$, which is too low to correspond to dust thermal emission (dust thermal emission

presents $\alpha > 2$). Therefore, both the flux density and spectral index of the central component indicate that its emission is mainly dominated by free-free emission from ionized gas.

Gas in young stellar objects can be ionized by two main mechanisms: shocks in accretion-driven jets (Anglada, Rodríguez & Carrasco-González 2015), and photoionization due to the high energy radiation from the central star (Alexander et al. 2014). Since accretion and ejection of material in jets are correlated (Cabrit 2007), low mass-accretion rate objects are expected to present relatively weak free-free emission from radio jets. However, recent studies with the VLA have shown that radio jets in this type of sources can produce free-free emission at levels that are detectable with the improved sensitivity of the VLA (Rodríguez et al. 2014). In particular, in Chapter 5 (Macías et al. 2016) we present VLA observations at 3 cm toward GM Aur revealing resolved free-free emission from a radio jet and from a photoevaporating disk, showing that both mechanisms can contribute at the same level to the total free-free emission.

Due to the low inclination of HD 169142 ($i \simeq 13°$), a possible radio jet would have a small projected size on the plane of the sky. Nevertheless, the central component detected at 7 mm shows a slight elongation with a PA$\simeq -80°$, which is consistent with the position angle of the disk rotation axis (PA$\simeq -85°$), as shown by molecular line observations (Raman et al. 2006). This suggests that the central component of emission observed in our images could be tracing an accretion-driven radio jet.

We can obtain a crude estimate of the free-free emission of an accretion-driven jet in HD 169142 with the empirical correlation between the radio luminosity, $S_\nu d^2$, of a source and its outflow momentum rate, $\dot{P}_{\rm out}$ (Anglada 1995; Anglada, Rodríguez & Carrasco-González 2015): $(S_\nu d^2/{\rm mJy\ kpc^2}) = 190(\dot{P}_{\rm out}/M_\odot\ {\rm yr^{-1}\ km\ s^{-1}})^{0.9}$. Wagner et al. (2015) measured a mass accretion rate onto the star $\dot{M}_{\rm acc} \simeq (1.5\text{–}2.7) \times 10^{-9}\ M_\odot\ {\rm yr^{-1}}$ in HD 169142. Assuming a ratio between mass loss rate in jets and mass accretion rate $\dot{M}_{\rm out}/\dot{M}_{\rm acc} \simeq 0.1$ (Cabrit 2007), we estimate that the outflow momentum rate should be $\dot{P}_{\rm out} \simeq 10^{-7}\ M_\odot\ {\rm yr^{-1}\ km\ s^{-1}}$. Therefore, the correlation would predict a flux density at 3 cm $S_\nu \simeq 5\ \mu$Jy, which is lower than our measured flux density of $20\pm5\ \mu$Jy for the central component. Even though this estimate might be subject to significant uncertainties, it suggests that an additional mechanism could contribute to the observed free-free emission.

As mentioned above, another possible mechanism contributing to the free-free emission is the gas photoionization due to high energy radiation from the central star. Extreme-UV (EUV) and, to a lesser extent, X-rays radiation impinging on the disk can ionize its surface (Clarke et al. 2001; Gorti, Dullemond & Hollenbach 2009; Owen et al. 2010). Part of the high energy radiation emitted by the central star could be photoionizing the inner disk, which would contribute to the free-free emission of HD 169142. An inhomogeneous inner disk could lead to an inhomogeneous irradiation of the disk surface, which could result in the asymmetric morphology of the central component observed at 7 mm.

According to Hollenbach & Gorti (2009), however, jets can significantly absorb the high-energy radiation emitted by the star, shielding the disk and photoionizing the ejected gas in the jet. For mass loss rates in the jet $\gtrsim 8 \times 10^{-10}\ M_\odot\ \mathrm{yr}^{-1}$, all the EUV radiation from the star should be absorbed by the jet. For lower values, the jet would be completely photoionized and high energy radiation from the star would be able to cross the jet and impinge on the disk surface. We expect a mass loss rate in the jet of HD 169142 of a few times $10^{-10}\ M_\odot\ \mathrm{yr}^{-1}$ assuming a ratio between mass loss and mass accretion rate $\dot{M}_{\mathrm{out}}/\dot{M}_{\mathrm{acc}} \simeq 0.1$ (Cabrit 2007). This suggests that the jet might be fully photoionized by the high energy radiation from the star. The free-free flux density of a completely photoionized jet should be much higher than the flux density of a shock-ionized jet with the same mass loss rate. As a consequence, a photoionized jet would be overluminous when compared to the empirical correlation between the radio luminosity and the outflow momentum rate, which was obtained for young protostars that have higher mass loss rates and, hence, cannot be significantly photoionized by high energy radiation (Anglada 1995; Anglada, Rodríguez & Carrasco-González 2015). Therefore, a photoionized jet could account for the observed central component of emission at radio wavelengths.

Finally, the peak of emission of the central component could be tracing the position of an independent object at a radius of ~ 4 au from the central star. We cannot discard this possibility with the current data. Given the proximity to the central star, the dynamical timescales are short. Thus, future observations should reveal detectable variations and/or proper motions in the observed emission that will allow to discriminate whether it traces material ejected from the central star (jet) or orbiting around it (disk or independent object).

3.3.3 Outer gaps

In order to improve the signal to noise ratio of the detected intensity, we have obtained the averaged radial intensity profiles of the 7 and 9 mm images (see Fig. 3.3.3). These profiles were produced by averaging the intensity within concentric elliptical rings, matching the inclination and position angle of the disk major axis determined by previous molecular line observations ($i = 13°$, and PA$= 5°$; Raman et al. 2006). The width of the concentric rings was set to the size of the beam, since the rms noise at spatial scales smaller than a beam is not independent.

Besides the inner gap (G1 from now on), two other gaps at radii $\sim 0.4''$ (~ 58 au; G2) and $\sim 0.7''$ (~ 102 au; G3) are revealed at both 7 mm and 9 mm. The inner (G1) and second gaps (G2) were already detected at near-IR wavelengths (Quanz et al. 2013; Momose et al. 2015) and in our previous observations at 7 mm (see Chapter 2; Osorio et al. 2014), confirming that G2 represents a real decrease in the dust density at these radii. G3 is reported here for the first time, and was not evident in previous observations since the signal to noise ratio was too low at these long distances from the central star. Nevertheless, the near-IR intensity profile presented in Fig. 2c of Momose et al. (2015) shows an irregularity that could correspond to the G3 gap.

As mentioned above, different studies have proposed that G1 and G2 are probably formed because of dynamical interactions between the disk and forming planets within each gap (Reggiani et al. 2014; Osorio et al. 2014; Momose et al. 2015; Wagner et al. 2015). However, the origin of the third gap (G3) is more difficult to understand. Detection of narrow gaps at such large distances, like G3, are very difficult. So far, similar gaps have only been detected up to distances ~ 90 au in the protoplanetary disks around HL Tau (ALMA Partnership et al. 2015a) and TW Hya (Andrews et al. 2016) through recent extremely high angular resolution ALMA observations. In comparison to these observations, G3 is the farthest detected gap at a distance ~ 100 au from the central star. The density in the disk mid-plane at such large distances is probably too low to create a planet responsible for clearing the observed gap. Alternatively, the magneto-rotational instability (MRI) in magnetized disks can create radial pressure variations, dubbed as zonal flows, which can in turn create gaps in the large dust grains distribution throughout protoplanetary disks (Bai & Stone 2014). These gaps, however, are expected to be narrow and shallow, which is not

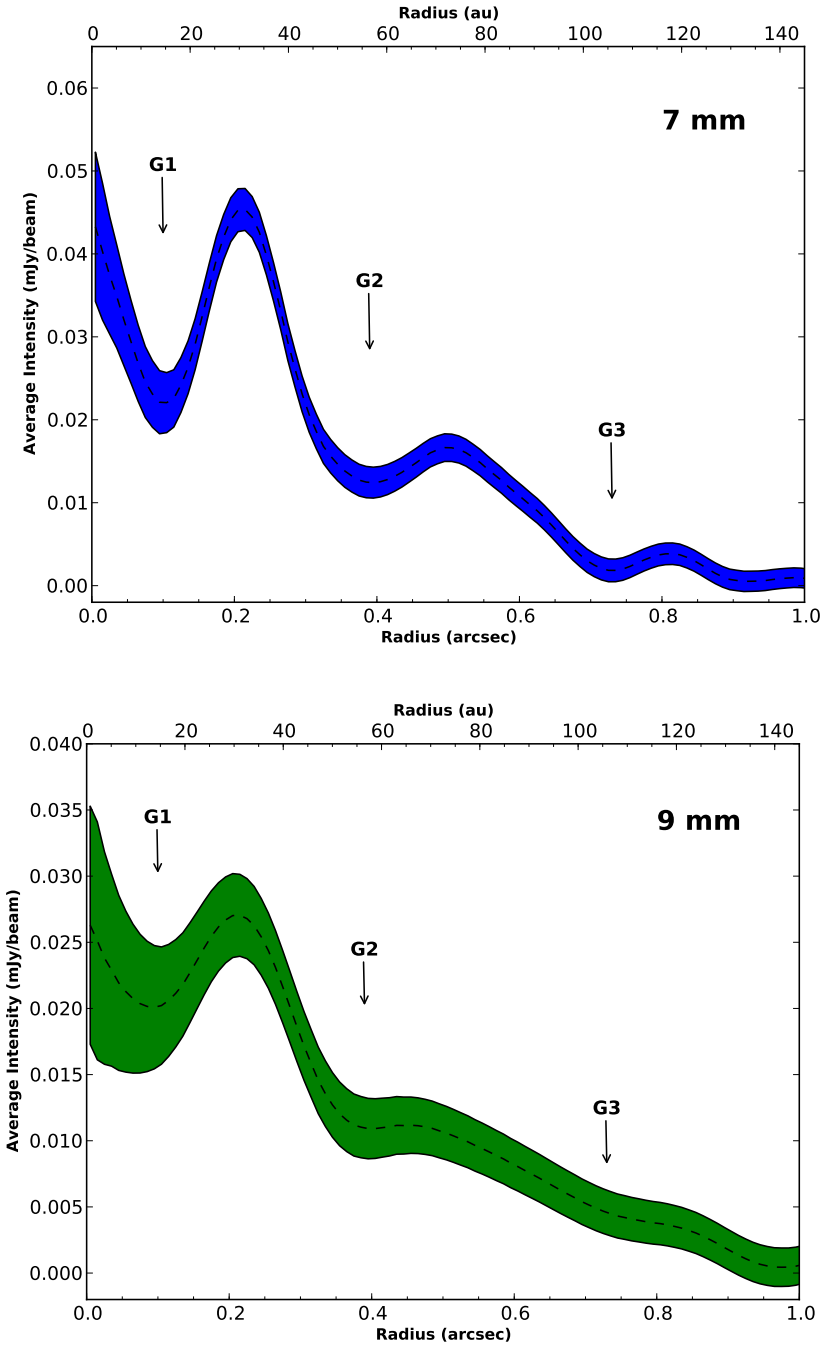

Figure 3.3 Averaged radial intensity profiles of the 7 mm (top panel) and 9 mm (bottom panel) images. The width of the lines indicates the 1σ uncertainty.

consistent with G3. MRI can also create pressure bumps at the outer edge of the dead zones in the disk (Flock et al. 2015). However, dead zones are expected to be closer to the central star, so models do not predict gaps as far as the observed G3 gap in HD 169142. Photoevaporation has also been claimed to be capable of opening gaps and cavities in disks (Owen et al. 2013). Nevertheless, models predict that these cavities should open at distances $\sim$ 1–10 au, where photoevaporation is most efficient in ejecting the gas from the disk in the form of a wind (Owen et al. 2013; Alexander et al. 2014). Therefore, even though we cannot completely discard a magnetic-induced or planet-induced origin for G3, both processes, together with photoevaporation, are unsuccessful explaining the observed G3 gap in HD 169142.

Another possible origin for G3 would be grain growth and trapping close to condensation fronts (i.e. snow lines) of volatiles in the disk. Models and laboratory experiments suggest that dust grains can grow significantly when surrounded by an icy mantle, which would form on the surface of the grains beyond these snow lines (Testi et al. 2014 and references therein). In addition, it has been predicted that the release of volatiles from the icy mantles of grains crossing the condensation fronts could create a local pressure bump at these radii. These pressure bumps would in turn trap the large dust grains, enhancing the dust-to-gas mass ratio and creating possible gaps and rings of emission (Ros & Johansen 2013).

Based on the composition of comets, the most abundant volatiles in protoplanetary disks are thought to be water, CO, and CO_2. These molecules have, for typical disk mid-plane densities, condensation temperatures of 128–155 K, 23–28 K, and 60–72 K, respectively (Zhang et al. 2015). Comparing these temperatures with the mid-plane temperatures obtained from our model (see Chapter 2; Osorio et al. 2014), we find that the water and CO_2 snow lines would fall within G1, while the CO snowline would be located at a distance $\sim$ 116 au. This is the distance of the outer edge of G3, which suggests that this gap could be produced by an accumulation of large dust grains close to the CO snowline. The large grains could be trapped in the pressure bump, creating a ring of emission at mm wavelengths next to a depletion of large grains at inner radii, resulting in the observed gap in the mm emission of the disk. This same physical mechanism has been suggested as the responsible for some of the rings and gaps that were detected by ALMA, close to the water, ammonia and CO_2 snowlines, in the disk around the younger T Tauri star HL Tau (ALMA Partnership

et al. 2015a; Zhang et al. 2015).

Therefore, we favor trapping and growth of dust grains close to the CO snow line as the most likely mechanism responsible for the gap G3 in HD 169142. Higher sensitivity and higher angular resolution observations at (sub-)mm wavelengths could be able to confirm the position of the CO snow line in the disk and compare it with the gap in the disk.

3.4 Summary and conclusions

We carried out additional high angular resolution VLA observations at 7 mm, 9 mm, and 3 cm toward the pre-transitional disk around HD 169142. These observations have significantly improved our previous observations and have allowed us to characterize the disk with a great degree of detail up to distances ~ 100 au.

Our 7 and 9 mm observations show a narrow ($\sim$ 15 au in width) azimuthally asymmetric ring of emission at a radius ~ 32 au tracing the rim of the inner gap. The size of the ring is consistent with our previous 7 mm observations (see Chapter 2; Osorio et al. 2014) as well as with near-IR polarized scattered light observations (Quanz et al. 2013; Momose et al. 2015). Significant substructure within the ring is revealed at 7 mm, with a knot of emission and two azimuthal dips. We interpret that these asymmetries are probably produced by tidal interactions between the disk and multiple forming planets. Additionally, we speculate that the ring could be undergoing a fragmentation process, resulting in the formation of a new protoplanet in the bright knot.

A central component of emission is detected inside the inner gap at 7 mm, 9 mm and 3 cm. The 7 mm emission shows a slightly elongated morphology along the E-W direction, with its peak of emission at a projected distance of ~ 4 au ($\sim 0\farcs03$) toward the W from the central star. The flux density and spectral index of this central component indicate that this emission is dominated by free-free emission from ionized gas, which could be associated with an inhomogeneous photoionization of the inner disk, with an independent object, or with an (asymmetric) ionized jet. We favor the latter scenario and speculate that this jet might be significantly photoionized by the high energy radiation emitted from the central star.

The radial intensity profiles of the 7 and 9 mm images reveal the presence of

multiple gaps in the disk of HD 169142. Our 7 and 9 mm observations not only confirm the presence of the inner (G1) and second (G2) gaps approximately at radii 0–30 au and 40–70 au, respectively, but also detect, for the first time, a new gap at radii 95–120 au (G3). This is one of the farthest gaps detected in a protoplanetary disk. We propose that dust grain growth close to the CO snowline, which seems to be located at the same radius, could be the mechanism responsible for this outer gap.

4

A dwarf transitional protoplanetary disk around XZ Tau B

4.1 Introduction

As discussed in Chapter 1, some accretion disks, known as transitional disks (Strom et al. 1989), present central cavities and annular gaps in their dust emission that have been attributed to the effects of tidal interactions of orbiting planetary or protoplanetary bodies (Papaloizou et al. 2007, Zhu et al. 2011, Andrews et al. 2011, Osorio et al. 2014) and are considered signposts of the planet formation process. Typical transitional disks imaged so far have radii of 50-100 au and masses of 10-100 M_J, with central cavities of 15-70 au in radius (Andrews et al. 2011, Espaillat et al. 2014, Andrews 2015). Nevertheless, some results, based on the spectral energy distribution (SED) modeling, suggest that significantly smaller disks should exist (McClure et al. 2008, Piétu et al. 2014), but direct imaging has not been possible yet.

XZ Tau B is a young M2 dwarf star (see stellar properties in Table 1) in the L1551 molecular cloud. It belongs to a triple system composed of the close pair XZ Tau A/C (separation $\sim 0.09''$) and XZ Tau B (currently located $\sim 0.3''$ to the NW; Carrasco-González et al. 2009). A sequence of expanding bubbles imaged by the HST (Krist et al. 2008) has been attributed to XZ Tau A/C (Carrasco-González et al. 2009, Zapata et al. 2015), while high velocity jets have been associated with both

XZ Tau A/C and XZ Tau B (Krist et al. 2008).

During the Long Baseline Campaign of the ALMA Science Verification process, a field centered on HL Tau was observed at 2.9 mm and 1.3 mm (ALMA Partnership et al. 2015a, 2015b; hereafter AP2015a, AP2015b). XZ Tau B was reported only as an unresolved continuum source at 2.9 mm. Here we present a detailed analysis of the 1.3 mm continuum observations that angularly resolve the source.

4.2 Observations

The observations were carried out between 2014 October 14 and November 14 using 42 antennas of ALMA, with baselines from 12 to 15,240 m. The phase center was at the position of HL Tau, α(J2000)=$4^{\rm h}31^{\rm m}38.4263^{\rm s}$, δ(J2000)=$18^\circ13'57.047''$. The 1.3 mm data were obtained from 2014 October 24 to 31 with the ALMA correlator configured in 4 spectral windows of 2000 MHz and 128 channels each. The 2.9 mm data were obtained using wide spectral windows for the continuum and narrow spectral windows centered on the HCO^+(1-0), HCN(1-0), CO(1-0), and CN(1-0) lines. A description of the observational setup and the calibration process is given in AP2015a, AP2015b.

The continuum emission at 2.9 mm was imaged by AP2015a (beam = $0.085'' \times 0.061''$, PA=-179°; rms = 24 μJy beam^{-1}). We obtained cleaned, continuum subtracted, channel maps (channel width = 0.25 km s^{-1}; beam = $0.10'' \times 0.06''$, PA=12°) for the observed line transitions. No line emission was detected towards XZ Tau.

Images at 1.3 mm were obtained with the task *clean* of CASA (version 4.2.2). XZ Tau falls $\sim 24''$ away from the phase center, where the response of the primary beam (FWHM $\simeq 27''$ at 1.3 mm) is only 1/19. However, the extraordinary sensitivity of ALMA allows a good signal-to-noise imaging. To avoid HL Tau sidelobes in the XZ Tau field, we first cleaned the HL Tau emission and subtracted it from the uv data. We tried several self-calibration strategies. Although self-calibration improves slightly the images of HL Tau, it blurs the XZ Tau images. We attribute these unfavorable effects on XZ Tau to the lack of a strong compact source in the field and to the large separation of XZ Tau from the phase center. Since we are interested in XZ Tau, we did not apply self-calibration in our final images. Given the narrow channel width and small integration time per visibility, the expected bandwidth and time smearing are negligible at the position of XZ Tau ($0.0016''$ and $0.0035''$, respectively).

Figure 4.1a shows our primary-beam corrected 1.3 mm image of XZ Tau B. The source is angularly resolved, with a size of $\sim 0.05''$ and a flux density of 7 ± 2 mJy[1]. At 2.9 mm it was reported as angularly unresolved (size $< 0.054''$) with a flux density of 1.83 ± 0.12 mJy (AP2015a; Zapata et al. 2015). Uncertainties in flux densities have been calculated as in AP2015a, but adding quadratically the absolute flux density calibration uncertainty (5%) and the primary beam response uncertainty due to pointing errors ($\sim 0.6''$), using the Dzib et al. (2014) prescription.

Since the 2.9 mm observations are less affected by the primary beam attenuation, they are much more sensitive. The fact that the source size upper limit set by these observations is similar to the observed size at 1.3 mm ($\sim 0.05'' \simeq 7$ au) indicates that the sensitivity of the 1.3 mm image is high enough to reveal the full structure of the source and not just the brightest part. Thus, we interpret the observed emission as tracing the dust of a very small (~ 3.5 au in radius) circumstellar disk.

Interestingly, the 1.3 mm ALMA image reveals substructure in the disk (Fig. 4.1a). Emission decreases towards the center, indicating a hole or cavity. Otherwise, the emission would peak towards the central position. We have plotted the real component of the visibility profile (Fig. 4.1b), which shows the characteristic null and negative region that confirm the presence of a central hole in the disk (e.g., Andrews et al. 2009). The null falls around 5-8 Mλ, corresponding to hole radii of 0.6-0.9 au to 1.4-2.2 au for the extreme cases of an infinite disk and a thin ring, respectively (Hughes et al. 2007)[2]. Since our small disk should be something intermediate, we estimate a radius of the hole $\sim$1 au, consistent with the value obtained from our modeling of the SED and image (§3). Thus, XZ Tau B appears to be a "transitional disk" (Calvet et al. 2005) with a small central cavity probably due to the tidal forces created by an orbiting substellar object or protoplanet (Andrews et al. 2011). In order to substantiate this interpretation we carried out a detailed modeling.

[1]Measured in a natural-weight image

[2]Visibilities have been recentered on XZ Tau B, but not deprojected to account for the disk inclination. So, these values are only rough estimates

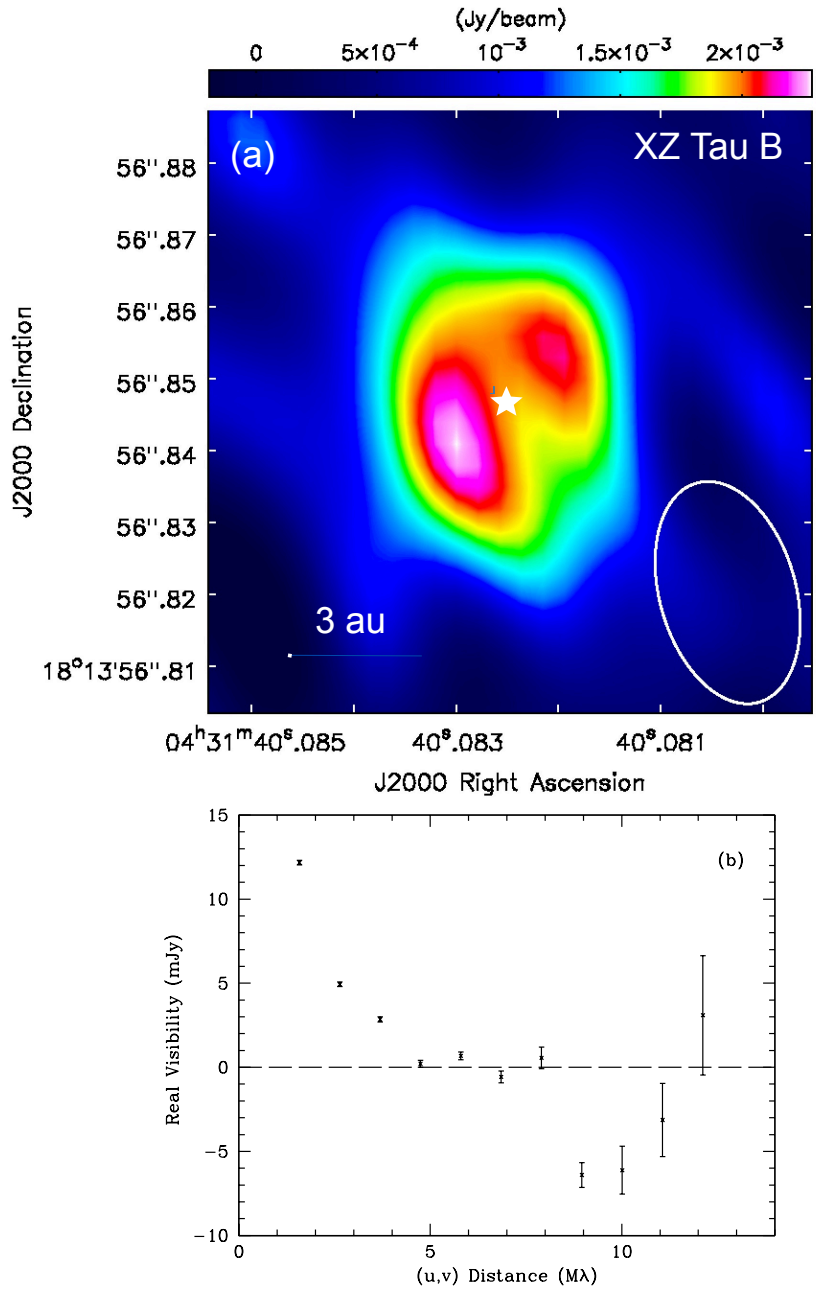

Figure 4.1 (a) ALMA image at 1.3 mm (robust=0, rms=0.28 mJy beam^{-1}) of the disk of dust around XZ Tau B (indicated by a star, at α(J2000)=4$^{\rm h}$31$^{\rm m}$40.0825$^{\rm s}$, δ(J2000)=18°13′56.847″). The synthesized beam (0.032″ × 0.019″, PA=16°) is shown in the lower-right corner. The intensity decrease in the northeast and southwest edges is an observational effect due to the beam elongation along this direction. (b) Azimuthally averaged visibility profile plotted in ∼1 Mλ bins.

4.3 Modeling

The disk parameters are determined by modeling and fitting the observed SED and the normalized radial intensity profile of the 1.3 mm image. To construct the observed SED we compiled photometric and spectroscopic data from the Spitzer, WISE, Akari, and IRAS databases, from the literature (Hartigan & Kenyon 2003, White & Ghez 2001, Carrasco-González et al. 2009, AP2015a, Forgan et al. 2014), and from this paper. Measurements that do not separate the A and B components have been taken as upper limits.

Our model includes the contributions from both the central star and the disk. Since the XZ Tau B star is known to be optically variable (Sandell & Aspin 1998), we reanalyzed the results of Hartigan & Kenyon (2003) but using the photometry of XZ Tau A from Coffey et al. (2004) to estimate the aperture correction. The stellar and accretion (veiling) luminosities of XZ Tau B were obtained following Pecaut & Mamajek (2013), Kenyon & Hartmann (1995), and Calvet & Gullbring (1998) assuming an M2 star and an 8000 K blackbody as the veiling source. Finally, using the Siess et al. (2000) tracks, the stellar parameters were derived (Table 1). The contribution of the central star to the SED (Fig. 4.3a) is calculated by using the reanalyzed fluxes and extrapolating to other wavelengths following Kenyon & Hartmann (1995) and Pecaut & Mamajek (2013).

The disk is modeled using an updated version of the irradiated α-accretion disk models with dust settling developed by D'Alessio et al. (2006). A dust grain population similar to the interstellar medium is used in the upper layers of the disk, while in the mid-plane a population of larger dust grains, with radii up to 1 mm, is assumed. The grain mixture composition is the same as in the model used in Chapter 2 (Osorio et al. 2014), but incorporating water ice with the abundance given by McClure et al. (2015), resulting in a dust-to-gas ratio of 0.0085. A central cavity is included in the model by emptying the innermost regions of the disk. The edge of this region, or wall, is directly irradiated by the star and the accretion shock and, thus, heated to a higher temperature (D'Alessio et al 2005).

The high H, K, and L band fluxes (Hioki et al. 2009, White & Ghez 2001) indicate that hot dust, that may correspond to a residual inner disk, is present inside the cavity, suggesting that XZ Tau B is at an earlier pre-transitional stage (Espaillat

et al. 2008). However, because of the variability of the star and the limited data in this wavelength range, we cannot determine the properties of this inner component, and thus we did not include it in our model.

The disk inclination (angle between the rotation axis and the line-of-sight) and PA were fitted by exploring different values, assuming as an initial guess that the disk lies in the B and A/C orbital plane ($i = 47°$; Carrasco-González et al. in preparation) and is perpendicular to the direction of the observed collimated jet (Krist et al. 2008).

Hence, the main free parameters are the viscosity parameter, α, the mass accretion rate in the disk, $\dot{M}_{\rm disk}$, and the degree of settling, ϵ. Planet-forming disks are expected to have dust populations highly settled onto the midplane (i.e., a low value of ϵ, defined as the dust-to-gas ratio in the atmosphere relative to the total of the disk), so that planetesimals can grow through the aggregation of large grains. Thus, we explored low values of ϵ, $0.001 \leq \epsilon \leq 0.1$.

To analyze how the viscosity affects the gas and dust evolution, we have carried out gas-dust two fluid hydrodynamical simulations as in Zhu et al. (2012). With a large viscosity (e.g., $\alpha = 10^{-2}$), such a small disk evolves very fast. As shown in the right panel of Figure 4.2, the disk gas surface density decreases by 4 orders of magnitude within 0.1 Myr and all the dust drifts to the central star. With a smaller viscosity (e.g., $\alpha = 10^{-3}$ as shown in the left panel of Fig. 4.2), $\sim$0.1 M_J mass planets are sufficient to produce a cavity which is almost two orders of magnitude deep. Thus, multiple planets could account for the observed cavity in XZ Tau B as long as the viscosity is small enough ($\alpha \leq 10^{-3}$).

Simulations also show that accretion onto the planet creating the gap can account for up to 90% of $\dot{M}_{\rm disk}$ (Zhu et al. 2011) and would reduce the mass accretion rate onto the star, $\dot{M}_*$. Therefore, we explored values of $\dot{M}_{\rm disk}$ in the range $\dot{M}_* < \dot{M}_{\rm disk} < 10\,\dot{M}_*$, where $\dot{M}_*$ is given in Table 1.

We have run a grid of 40 models with parameters in the above-mentioned ranges. Since we are interested in studying the capability of the disk to form planets, we have selected the model that fits the data with the highest allowed value for the viscosity parameter, which gives the lowest disk mass (9 M_J). As we show in §4, even this low-mass disk is capable to form a planetary system. The parameters of this disk are given in Table 1.

The resulting SED, showing the separate contributions of the main components,

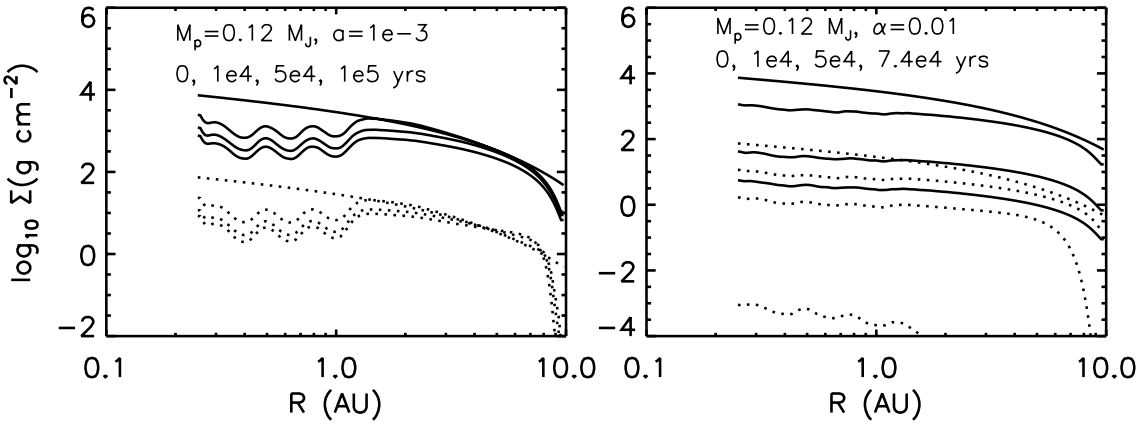

Figure 4.2 Hydrodynamical simulations of the surface density (solid line=gas; dotted line=1 mm dust) at different times for viscous disks (α=0.001, left; α=0.01, right) with three accreting 0.12 M_J planets, at radii 0.4, 0.63, and 1 au.

is plotted in Figure 4.3a. The free-free contribution from the ionized jet has also been taken into account in the fit, showing that it is negligible in the mm range. A comparison of the observed and model intensity profiles along the major axis of the disk is shown in Figure 4.3b. Figure 4.3c shows the surface density and temperature model profiles. Figure 4.3d shows a CASA simulated image of the model emission at 1.3 mm as it would be observed with the same ALMA configuration as Figure 4.1. These figures show that the model reproduces the observations reasonably well. Thus, our results support the interpretation that XZ Tau B is associated with a dwarf transitional disk.

4.4 Discussion

Modeling shows that the outer radius of the disk is 3.4 au and the radius of the central cavity is 1.3 au (Table 1). These radii are well constrained by the intensity profile and are much smaller than those of other transitional disks (typically ∼50-100 au for the disk and ∼15-70 au for the cavity; Andrews et al. 2011, Espaillat et al. 2014, Andrews 2015). Tidal interactions in a close binary are expected to truncate circumstellar disks to an outer radius ∼1/3 of the binary separation (Papaloizou & Pringle 1977). This has been observed in the L1551-IRS5 binary system of disks, each 10 au in radius (Rodríguez et al. 1998). Interestingly, the radius of the XZ Tau B disk

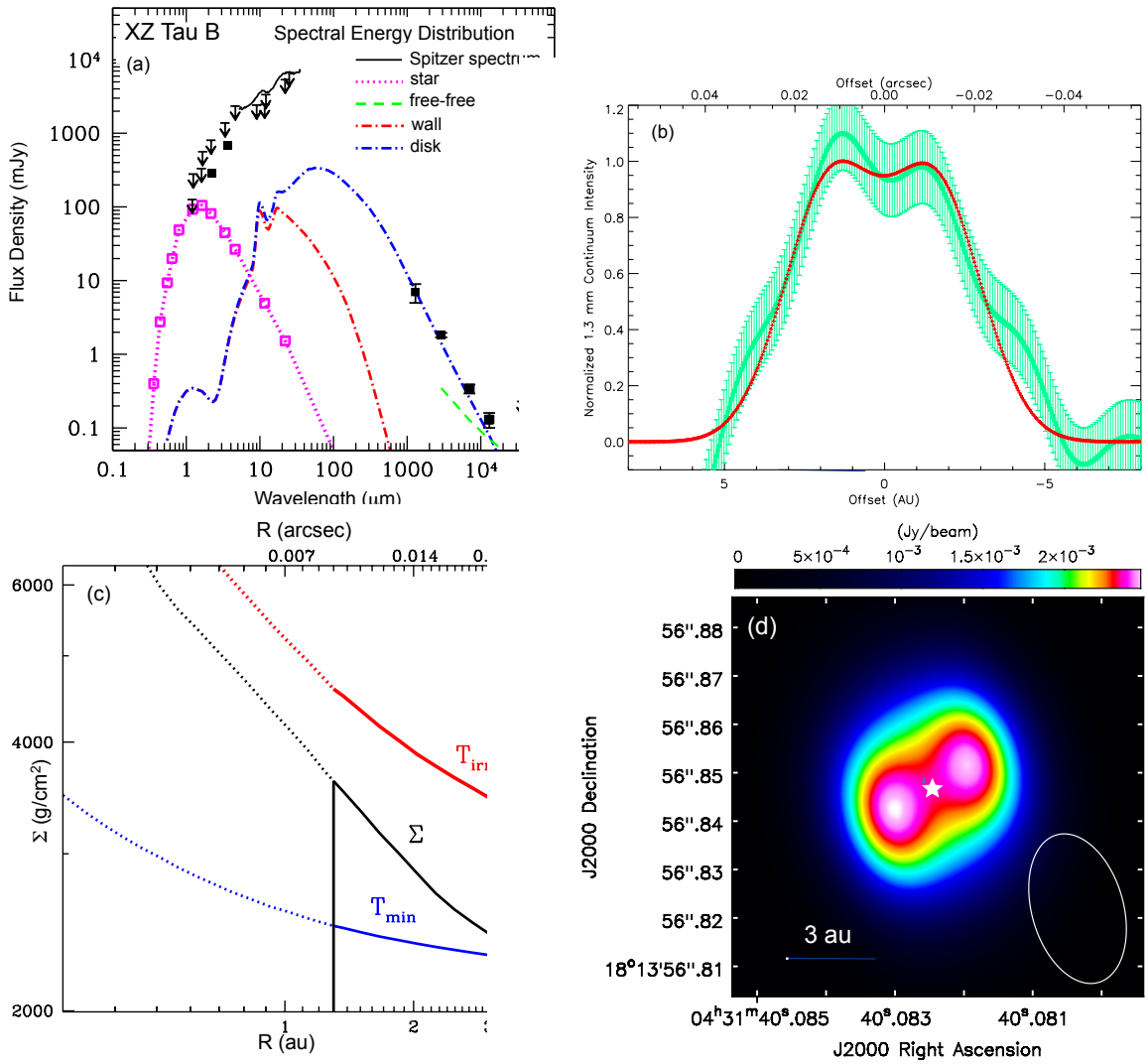

Figure 4.3 (a) Spectral energy distribution. Solid square symbols and continuous line are observational data. Arrows are upper limits, corresponding to data that do not separate XZ Tau B from A/C components. Open squares represent the calculated contribution of the star (see text). Discontinuous lines represent the model results. (b) Observed (green line with 1-σ error bars) and model (red line) normalized intensity profile along a line passing through the two maxima (PA=126°) of the disk (positive offsets to the east). (c) Model surface density (Σ), irradiation temperature ($T_{\rm irr}$), and minimum temperature ($T_{\rm min}$) radial distributions. (d) CASA simulated image of the 1.3 mm model emission, assuming the same antenna configuration as in Figure 4.1a.

Table 4.1. Parameters of the XZ Tau B Star and Disk

Parameter	Value	Notes	Refs.
	Star		
Distance (pc)	140	Adopted	1
Visual Extinction (mag)	1.4	Adopted	2
Spectral Type	M2	Adopted	2
Age (Myr)	4.6	Adopted	2
Effective Temperature (K)	3550	Adopted	2
Radius ($R_\odot$)	1.24	Calculated	
Mass ($M_\odot$)	0.37	Adopted	2
Mass Accretion Rate ($M_\odot$ yr^{-1})	1.4×10^{-8}	Calculated	
	Disk		
Inclination Angle (deg)	35±10	Adopted/Refined	3
Position Angle of Major Axis (deg)	140±10	Adopted/Refined	4
Inner Radius (au)	1.30±0.05	Fitted	
Outer Radius (au)	3.4±0.1	Fitted	
Viscosity Parameter	0.001	Adopted	
Mass Accretion Rate ($M_\odot$ yr^{-1})	7.0×10^{-8}	Fitted	
Degree of Settling	0.10	Fitted	
1.3 mm Optical Depth at 1 au	18	Calculated	
1.3 mm Optical Depth at 3.4 au	14	Calculated	
Mass Evacuated in Cavity (M_J)	3	Calculated	
Total Mass (M_J)	9	Calculated	
Dust Mass ($M_\oplus$)	25	Calculated	
	Cavity Wall		
Radius (au)	1.30±0.05	= Disk Inner Radius	
Temperature (K)	420	Calculated	
Height (au)	0.09	= Disk Hydrostatic Scale Height	

References. — (1) Torres et al. 2009; (2) Hartigan & Kenyon 2003; (3) Carrasco-González et al. in preparation (4) Krist et al. 2008

is significantly smaller than the value of ∼14 au expected from tidal truncation, given the separation of ∼42 au between XZ Tau B and the A/C pair. A highly eccentric orbit could truncate the disk at a smaller radius, but the analysis of the relative positions of the stars over >20 yr favors a nearly circular orbit (Carrasco-González et al. 2009, Carrasco-González et al. in preparation).

The reason for the small size of the XZ Tau B disk is uncertain. It is feasible that the disk was originally small; that simple tidal truncation models (Papaloizou & Pringle 1977) may not apply for the particular geometry of this disk and truncation occurs at a smaller scale; that the disk is outwardly truncated by a forming planet in an outer orbit (Osorio et al. 2014); or that the outer parts of the disk have been removed by other mechanisms (e.g., swept out by the sequence of expanding bubbles from the A/C stars; Krist et al. 2008). It is possible that the small dust grain and the gas components of the XZ Tau B disk are more extended than the mm-sized particle distribution traced by our observations, as it occurs in standard disks due to the radial migration of large dust grains (e.g., HD 163296; de Gregorio-Monsalvo et al. 2013). Unfortunately, the sensitivity of our line observations is insufficient to set a tight constraint to the gas disk size. We have started to include radial migration of dust grains in our model (see Appendix A in Chapter 2), so we expect that by modeling future sensitive observations we will be able to determine whether this effect is playing an important role in the disk. Anyhow, the disk of dust in XZ Tau B is much smaller than any other angularly resolved disk of dust imaged so far.

The observed image (Fig. 4.1a) is marginally asymmetric, with the flux density in the southeast region ∼ 30% higher than in the northwest one. Such an asymmetry could not result from opacity effects due to the disk inclination since our modeled image (Figs. 4.3b, 4.3d) is symmetric. Instead, this asymmetry is suggestive of a dust trap, where the largest dust grains accumulate (e.g., Birnstiel et al. 2013, van der Marel et al. 2013). However, this needs to be confirmed with higher sensitivity data.

These results suggest that XZ Tau B shows the features that characterize transitional disks, but on a much smaller scale (e.g., compare Fig. 4.1a with Fig. 2.1b in Chapter 2). Since the evolution of these features is determined by their orbital motions around the central star, a dwarf disk like XZ Tau B is expected to evolve ∼50-500 times faster than their bigger counterparts. Unfortunately, the current 1.3 mm ALMA observations, spanning just one week, are insufficient to search for disk

evolution, but significant changes can occur in observations separated by only a few months. Thus, we anticipate that the disk in XZ Tau B, and possibly other similar dwarf disks, may serve in the near future as valuable small-scale models for a fast and efficient study of the evolution of transitional disks.

The diversity of planetary systems observed in the exoplanet surveys suggests that an equivalent diversity should be found in their progenitors, the protoplanetary disks. In particular, the Kepler mission has identified a number of "low-mass compact multiple-planet systems", orbiting within < 1 au from the star and with planetary masses ranging from a fraction to a few times the Earth's mass (Lissauer et al. 2011, 2014, Jontof-Hutter et al. 2015). Dwarf disks similar to that found in XZ Tau B appear as the natural precursors of these systems.

To fit both the relatively high mm flux density of the disk and its small size, a high mass accretion rate was needed in our model. This, combined with the low viscosity of the disk, resulted in very high disk surface densities (Fig. 4.3c). These values are higher than those expected at the inner regions of larger disks around this type of stars (Williams & Cieza 2011, Andrews 2015) but they are still one order of magnitude smaller than the values of the "minimum mass protoplanetary nebula" estimated by Swift et al. (2013) to form "in situ" the Kepler-32 planetary system.

It is also interesting to compare with the compact system of five sub-Earth radius planets around the K0 star Kepler-444A, in a hierarchical triple stellar system. Dupuy et al. (2016) estimated a small radius of $\sim$2 au and a relatively large mass $\gtrsim 70\,M_J$ for the primordial protoplanetary disk around Kepler-444A. These authors propose that the outer regions of such a massive disk would have been unstable, leading to the formation of the triple star system through gravitational fragmentation. XZ Tau B could be similar to Kepler-444A. However, the disk of XZ Tau B presents a central gap, while the planets around Kepler-444A have masses well below the gap-opening mass (Dupuy et al. 2016). This implies that the planets recently formed in XZ Tau B are probably more massive than the planets around Kepler-444A. The reason of this could be the difference in the position of the snowline. Whereas the whole disk of Kepler-444A would have fallen within its snowline, our model of XZ Tau B shows that (for points slightly above the disk midplane, where the minimum temperature is reached) it could be located inside the cavity, at a radius of $\sim$0.5 au, where $T_{\rm min} = 180$ K (Fig. 4.3c). Therefore, giant planets, which form much more

easily beyond the snowline (e.g., Ros & Johansen 2013), could be forming in the XZ Tau B disk cavity.

Some theoretical studies already pointed to the possible existence of a relatively large population of very small disks (McClure et al. 2008, Piétu et al. 2014, Kraus et al. 2015, Furlan et al. 2016). However, none of these putative dwarf disks has been angularly resolved. In XZ Tau B we have been able, not only to angularly resolve the disk and determine its size, but also to observe and model its substructure at au-scales.

4.5 Summary and conclusions

We analyzed Atacama Large Millimeter/Submillimeter Array (ALMA) observations of the star XZ Tau B with the highest angular resolution ($\sim 0\farcs02$) obtained so far by this instrument.

We discovered a dwarf protoplanetary disk around the star XZ Tau B that shows all the features of a classical transitional disk but on a much smaller scale.

The dust emission of the disk has a very small radius of $\sim$3.4 au and presents a central cavity of $\sim$1.3 au in radius that we attribute to clearing by a compact system of orbiting (proto)planets. The image also shows a slight azimuthal asymmetry that could be associated with a dust trap. Given the very small radii involved, evolution is expected to be much faster in this disk (observable changes in a few months) than in classical disks (observable changes requiring decades) and easy to monitor with observations in the near future.

We have modeled the dust thermal emission of XZ Tau B, showing that its surface density is higher than the values expected at the inner regions of larger disks around similar stars. We speculate that this high densities could be related to the origin of the triple stellar system XZ Tau, where XZ Tau B is located. Additionally, we have performed hydrodynamical simulations that, together with our modeling results, indicate that the mass of the disk is large enough to form a compact planetary system, which could be already forming in the inner regions of the disk producing the observed inner dust cavity.

The Kepler mission raised a number of puzzling questions regarding the observed planetary systems at distances < 1 au from the star, such as the debate of migration

versus "in situ" planetary formation (Ogihara et al. 2015), or the abundance of super-Earths very close to the star (Lee et al. 2014). XZ Tau B opens a new window to investigate with ALMA observations the disk evolution and first stages of planet formation on time-scales and at radii that so far remained unexplored.

5

Imaging the photoevaporating disk and radio jet of GM Aur

5.1 Introduction

Photoevaporation, together with viscous accretion, is expected to play an important role in the dispersal of protoplanetary disks (Williams & Cieza 2011; Alexander et al. 2014). High energy radiation – i.e. far-UV (FUV), extreme-UV (EUV), and X-ray radiation – originating at the stellar chromosphere of low-mass stars can ionize and heat the disk surface (Clarke et al. 2001; Gorti, Dullemond & Hollenbach 2009; Owen et al. 2010). Beyond a critical radius, the thermal energy of the heated surface becomes higher than its binding gravitational energy and the gas escapes in the form of a wind. While EUV photons produce a fully-ionized wind, X-rays can penetrate into deeper, neutral regions of the disk, creating a denser, partially-ionized photoevaporative wind (Gorti, Dullemond & Hollenbach 2009; Owen et al. 2011).

As explained in Chapter 1, the early stages of disk evolution are dominated by viscous accretion, but as the accretion rate decreases, central star-driven photoevaporation should eventually dominate over disk accretion, clearing the gas and leading the disk into the debris disk phase (Alexander et al. 2014). The timescale of gas removal and, thus, the impact of photoevaporation in the disk evolution, will strongly depend on the ionization rate reaching the disk and the mass loss rate produced by

the photoevaporative winds.

So far, the primary diagnostic of disk photoevaporation has been optical and mid-IR forbidden line emission (e.g. [O I] 6300 Å and [Ne II] 12.81 μm) from the wind (Font et al. 2004). The redshifted side of the flow is blocked by the disk midplane, which is optically thick at these wavelengths. Therefore, the line profile is expected to be essentially narrow ($\sim$ 10 km s^{-1}) and blueshifted by 5–7 km s^{-1} (Font et al. 2004), although high disk inclinations and optically thin regions in the disk (like gaps or cavities) can produce broader lines centered at the systemic velocity (Alexander 2008). Blueshifted lines have been detected in a number of protoplanetary disks (Najita et al. 2009; Pascucci & Sterzik 2009; Sacco et al. 2012). However, similar line profiles and luminosities can be obtained with different models (Alexander et al. 2014). Therefore, these lines cannot be used to constrain the high energy radiation responsible for the photoevaporative wind or to infer the mass loss rate in the flow (Ercolano & Owen 2010).

Lugo et al. (2004), and more recently Avalos & Lizano (2012), proposed that free-free emission at cm wavelengths could be used as a diagnostic of disk photoevaporation in massive stars. Pascucci et al. (2012) and Owen et al. (2013) followed a similar approach focusing on central star-driven photoevaporation in low-mass stars, and proposed that cm observations could actually provide a better observational test than forbidden line observations. The free-free emission from the fully (EUV case) or partially (X-rays case) ionized disk surface is optically thin and, thus, directly proportional to the ionizing radiation reaching the disk. Since the X-ray luminosity of T Tauri stars can be directly measured, one can in principle estimate the free-free emission produced by the X-ray-ionized gas and, therefore, estimate the EUV photon luminosity impinging on the disk from the remaining observed emission. Following this idea, recent observational studies at cm wavelengths have focused on the free-free emission of protoplanetary disks in order to constrain photoevaporation models (Galván-Madrid et al. 2014; Pascucci et al. 2014). Due to their limited angular resolution, however, it is difficult to ascertain that these radio observations were not contaminated by free-free emission from an accretion-driven collimated jet. Since classical T Tauri stars present lower accretion rates than younger stellar objects, weak (or even absent) radio jet emission is expected in this type of sources. Nevertheless, thanks to the improved sensitivity of the Karl G. Jansky Very Large Array

(VLA), Rodríguez et al. (2014) were recently able to resolve the emission at 3.3 cm of a relatively weak radio jet in AB Aur, a Herbig Ae star surrounded by a transitional disk.

GM Auriga is a well-known T Tauri star ($d \simeq$140 pc, K5 spectral type, $L_\star \simeq 0.9$ $L_\odot$, $M_\star \simeq 1.1$ $M_\odot$; Kenyon & Hartmann 1995) surrounded by a transitional disk with a dust cavity of radius ~ 24 au ($\sim 0.17''$; Calvet et al. 2005; Hughes et al. 2009; Espaillat et al. 2010). [O I] and [Ne II] lines have been detected towards GM Aur, indicating the presence of high energy radiation reaching the disk. However, the [OI] spectrum has a very poor spectral resolution and the [NeII] spectrum shows no clear evidence of a blueshifted line peak that would confirm the presence of photoevaporation in GM Aur (Hartigan et al. 1995; Najita et al. 2009). This could indicate that the lines are tracing a bounded ionized layer of the disk (Najita et al. 2009). Alternatively, the lack of an observed blueshifted line peak could actually be due to the disk cavity, which could allow the redshifted component of the wind to be visible (Owen et al. 2013), or due to an insufficient signal-to-noise ratio in the [Ne II] spectrum. Therefore, even though observations indicate that high energy radiation is impinging on the disk surface, the presence of photoevaporation in GM Aur is still uncertain.

Here we report new sensitive high angular resolution VLA observations at 7 mm, 3 cm, and 5 cm towards the transitional disk of GM Aur, showing evidence of the presence of free-free emission from both photoevaporative winds and a radio jet.

5.2 Observations

Our new observations were carried out with the VLA of the National Radio Astronomy Observatory (NRAO)[1] using three different configurations (A, B, and C) at Q (7 mm), X (3 cm), and C (5 cm) bands. We also reduced VLA archival data at Ka, K, and C bands (see Table 5.1). For all the observations, 3C147 and J0438+3004 were used as the amplitude and complex gain calibrators, respectively. 3C84 was observed at Q band in order to calibrate the bandpass and delays. For the rest of the bands 3C147 was used as the bandpass calibrator. The expected uncertainty in the absolute flux calibration is $\sim 10\%$.

[1]The NRAO is a facility of the National Science Foundation operated under cooperative agreement by Associated Universities, Inc.

Table 5.1. VLA observations

Project Code	Observing Date	Conf.	Band	Central Frequency (GHz)	Bandwidth (GHz)	On-source time (min)
15B-352	2015-Sep-28	A	C	6	4	39.6
	2015-Sep-10					39.6
15B-352	2015-Sep-26	A	X	10	4	38.6
	2015-Sep-11					38.6
14B-285	2015-May-09	B	X	10	4	41.8
14B-285	2014-Oct-16	C	Q	44	8	24.2
14B-285	2014-Oct-16	C	X	10	4	8.6
AC982	2011-Jul-25	A	C	6	2	22.3
BL175	2011-May-22	BnA	C	6	2	3.6
BL175	2011-Apr-25	B	C	6	2	3.5
	2011-Mar-06					3.6
AC982	2010-Nov-14	C	Ka	30.5, 37.5	2×2	94.5
AC982	2010-Sep-13	D	Ka	32.7	2	3.0
	2010-Sep-10					2.3
AC982	2010-Sep-11	D	K	21	2	24.0
	2010-Aug-24					4.8

Note. — Observations from projects AC982 and BL175 were taken from the VLA archive.

Data calibration was performed using the VLA pipeline integrated in the data reduction package Common Astronomy Software Applications (CASA; version 4.3.1)[2]. After running the pipeline, we inspected the calibrated data, performed additional data flagging and re-ran the pipeline as many times as needed. Cleaned images were obtained with the CLEAN task of CASA by using the multi-scale multi-frequency deconvolution algorithm described in Rau & Cornwell (2011). In order to get a better frequency coverage we also split in frequency the observations at Q and X bands, obtaining images at 6.5 mm, 7.1 mm, 2.7 cm, and 3.3 cm.

5.3 Results

We have compiled the flux densities (S_ν) of GM Aur at different (sub-)mm and cm wavelengths, both from our new data and from the literature (Table 5.2), and have constructed the spectral energy distribution (SED) shown in Fig. 5.1. As can be seen, the emission at cm wavelengths is above the expected contribution from the dust. The flat spectral index ($\alpha < 2$, where $S_\nu \propto \nu^\alpha$) between 5 and 2 cm cannot be explained with only dust emission, even assuming large (cm-sized) dust grains. By fitting the sum of two power laws to the SED from 0.89 mm to 5 cm, the emission can be explained as a combination of dust thermal ($\alpha_d = 3.05 \pm 0.14$) and free-free emission from ionized gas ($\alpha_{\rm ff} = 0.75 \pm 0.13$). The positive spectral index of the spectrum between 5 and 3 cm, as well as the fact that the source at 3 cm appears to be extended, indicate that the contribution of possible non-thermal emission is negligible.

The measured flux density at 7 mm, obtained using the full bandwidth of 8 GHz, is $\sim 1.25 \pm 0.14$ mJy, consistent with previous VLA observations (Rodmann et al. 2006). From our SED fit at cm wavelengths, we expect a free-free contribution at 7 mm of ~ 0.2 mJy, which represents only a $\sim 16\%$ of the emission at this wavelength. Thus, at 7 mm we are mainly detecting the dust emission. Our 7 mm map shows a resolved disk structure (Fig. 5.3a), although the angular resolution is not enough to reveal the inner cavity of radius ~ 24 au (Calvet et al. 2005; Hughes et al. 2009). From a Gaussian fit to the 7 mm image, we obtained a deconvolved disk size of ~ 220 au $\times$ 110 au (measured at the 3σ level), with its major axis oriented in the NE-SW

[2]https://science.nrao.edu/facilities/vla/data-processing

Table 5.2. GM Aur Flux Densities

Frequency (GHz)	Wavelength (mm)	Flux[a] (mJy)	Ref.
480	0.623	1300±300	2
390	0.769	850 ± 90	2
375	0.800	730 ± 70	1
350	0.856	640 ± 70	6
337	0.89	550 ± 70	7
230	1.3	170 ± 17	3
230	1.3	180 ± 30	6
230	1.3	173 ± 19	7
141	2.13	37 ± 4	5
110	2.72	21 ± 3	6
108	2.77	19 ± 3	4
46.0	6.52	1.42 ± 0.18[b]	8
42.0	7.14	1.12 ± 0.13[b]	8
37.5	8.0	0.80 ± 0.09	8
32.7	9.17	0.66 ± 0.13	8
30.5	9.8	0.48 ± 0.06	8
21.0	14.3	0.25 ± 0.05	8
11.0	27.25	0.098 ± 0.014	8
9.0	33.3	0.069 ± 0.011	8
6.0	50.0	0.040 ± 0.009	8

[a] The uncertainties include the absolute flux calibration uncertainty.

[b] Previous measurements of the flux density at 7 mm, consistent within the uncertainties with our measurements, were obtained by Rodmann et al. (2006). We adopted the values obtained from our observations because they have a higher sensitivity.

References. — (1) Weintraub et al. (1989); (2) Beckwith & Sargent (1991); (3) Dutrey et al. (1998); (4) Looney et al. (2000); (5) Kitamura et al. (2002); (6) Hughes et al. (2009); (7) Andrews et al. (2013); (8) This paper.

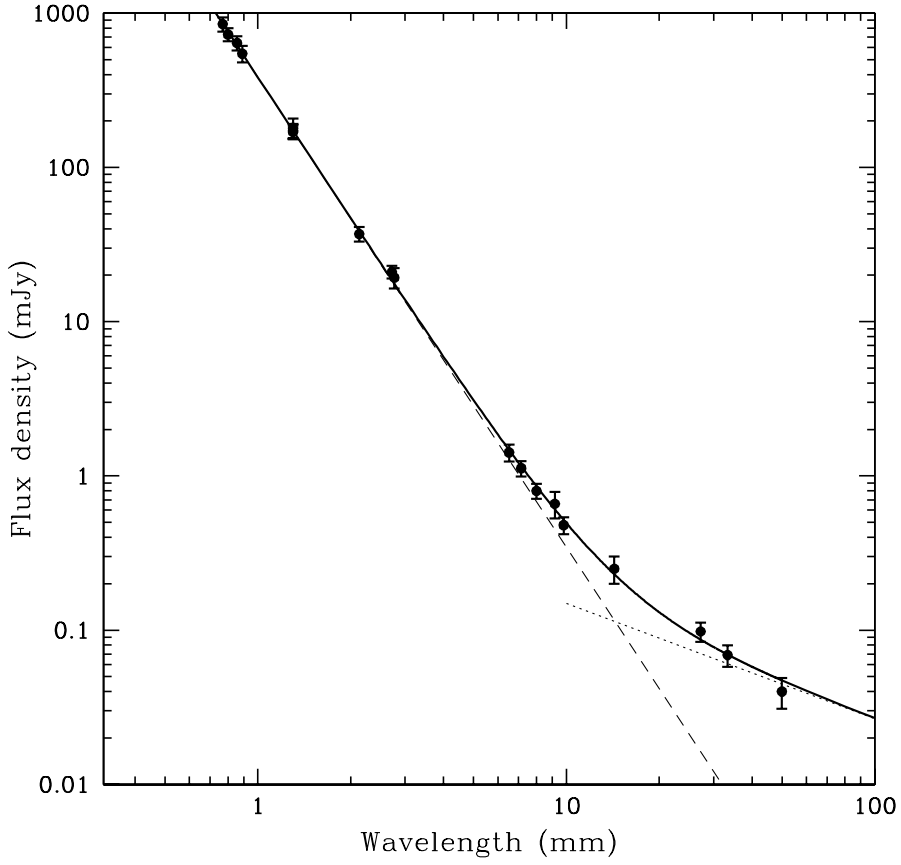

Figure 5.1 Spectral energy distribution (SED) of the radio emission of GM Aur. The data points and error bars are listed in Table 5.2. The lines indicate the fit to the SED (dashed: dust thermal emission; dotted: free free emission; solid: total).

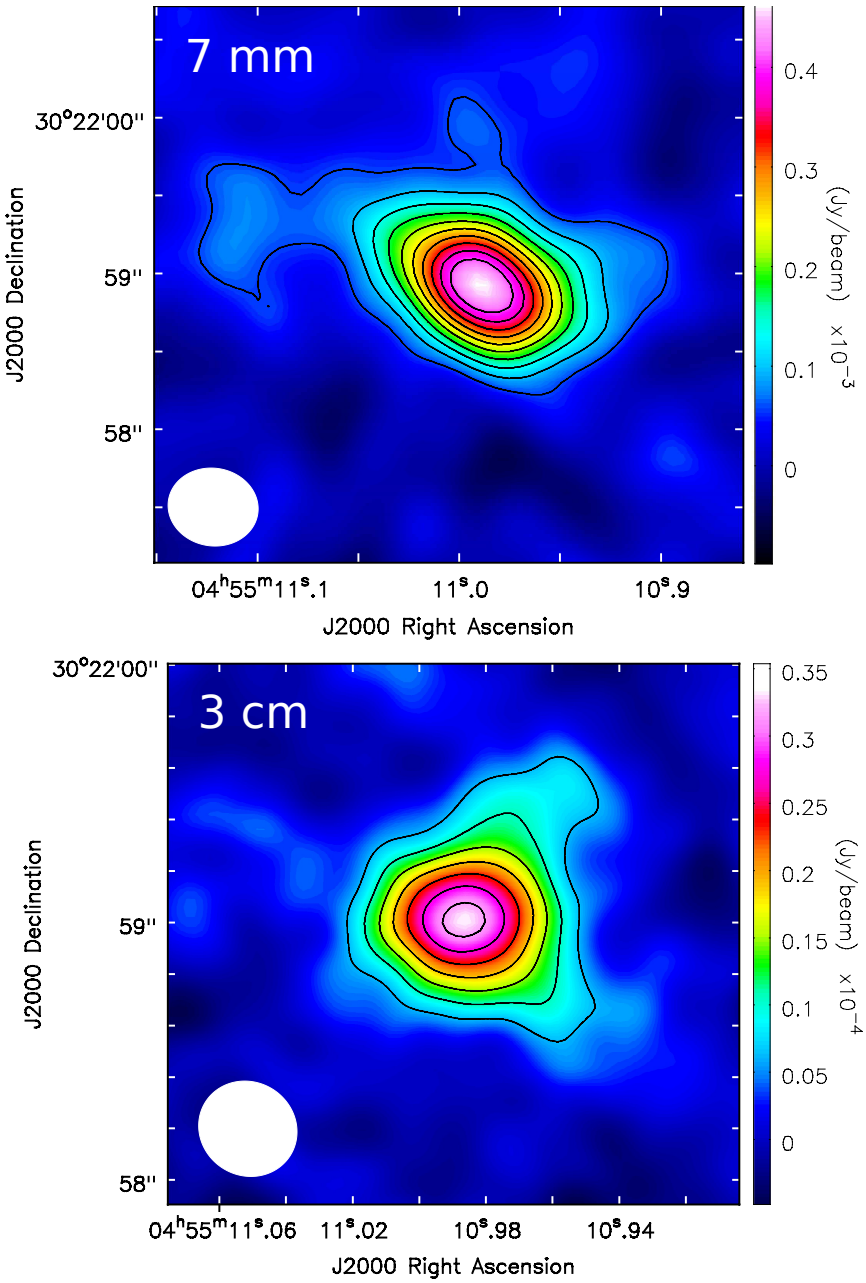

Figure 5.2 Top: Naturally weighted VLA image at 7 mm of the transitional disk around GM Aur (synthesized beam=0.″58 × 0.″50, PA=81°; shown in the lower-left corner). Contour levels are −3, 3, 5, 7, 9, 11, 13, 15, 17, 19, and 21 times the rms of the map, 19.3 μJy beam^{-1}. Bottom: Naturally weighted VLA image of the 3.0 cm emission obtained by combining data from A and B configurations (synthesized beam=0.″35 × 0.″32, PA=56°; shown in the lower-left corner). Contour levels are −3, 3, 5, 7, 9, 11, 13 and 15 times the rms of the map, 2.1 μJy beam^{-1}.

direction (PA$\simeq 60°$), similar to previous studies at (sub-)mm wavelengths (Rodmann et al. 2006; Hughes et al. 2009).

An image of the 3.0 cm emission is presented in Figure 5.3b. The emission shows a tripolar structure, suggesting a combination of dust emission from a disk and free-free emission from a monopolar (one-sided) radio jet perpendicular to it. This kind of morphology, with two perpendicular structures, has already been observed in other sources, such as HH 111 (Rodríguez et al. 2008) and HH 80-81 (Carrasco-González et al. 2012). In both cases, the emission was separated into two components by fitting two Gaussians to it. In the case of GM Aur, we estimate from the SED fit a dust contribution at 3.0 cm of ~ 11 μJy, which represents only 1/8 of the detected emission at 3.0 cm. In order to check whether this flux density can account for the disk emission of GM Aur at 3.0 cm, we obtained an image of the estimated dust emission at 3.0 cm by scaling the 7 mm image with the dust spectral index obtained from the SED fit. We then subtracted this scaled image to the 3.0 cm image, which was previously convolved to have the same angular resolution as the 7 mm observations. The resulting image still showed significant emission from the disk. By fitting two Gaussians to the remaining 3.0 cm emission, we separated the source into a component with the same PA as the GM Aur disk ($S_\nu = 31 \pm 3$ μJy), and another one perpendicular to it ($S_\nu = 45 \pm 3$ μJy)[3] (Fig. 5.3). We interpret these two components to be tracing the free-free emission from a photoevaporating disk and a radio jet, respectively (see §4).

We also combined our new 5 cm observations with archival data (Table 5.1) to get a sensitive image (rms$\simeq 2.5$ μJy; beam=$0\farcs53 \times 0\farcs36$, PA=$-74°$). The image shows a compact source at the position of the star, although its size is sensitivity limited. Hence, we were not able to constrain the size of the source at this wavelength. The rest of the archival observations, at Ka and K bands, were obtained with relatively low angular resolution, so they showed an unresolved source at the position of GM Aur.

[3]We note that none of the fit parameters were fixed and yet two perpendicular components were obtained.

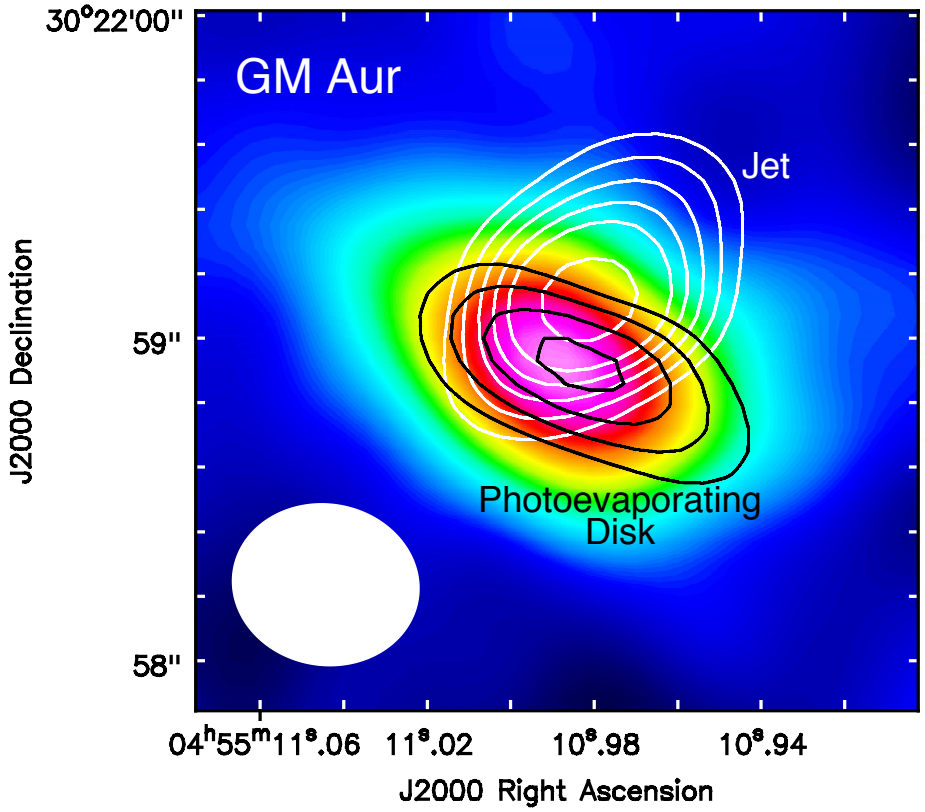

Figure 5.3 Superposition of the two components of the free-free emission at 3.0 cm obtained from our two-Gaussian fit (black and white contours) over the 7 mm emission of the transitional disk of GM Aur shown in Fig. 5.3a (color scale). We propose that the disk component (black contours) is produced by the photoevaporative winds arising from the disk, while the perpendicular component (white contours) is tracing the free-free emission from an accretion driven radio jet. The 3.0 cm image was previously convolved to the same angular resolution ($0\farcs58 \times 0\farcs50$, PA=81°; shown in the lower-left corner) as the 7 mm image. Contour levels are −3, 3, 4, 5, 6, 7, and 9 times the rms of the convolved 3.0 cm image, 2.8 μJy beam^{-1}.

5.4 Discussion

The excess of free-free emission at cm wavelengths in GM Aur has been previously attributed, as well as in other transitional disks, to photoevaporative winds arising from the disk (Pascucci et al. 2012; Owen et al. 2013). Our 3.0 cm observations spatially resolve the emission, indicating the presence of two different components of free-free emission, one with the same PA as the GM Aur disk and another one perpendicular to it. The morphology of the disk component, as well as its flat spectral index between 5 and 2 cm, indeed suggests the presence of photoevaporative winds in GM Aur. However, our results indicate that a similar fraction of the free-free emission is arising from the perpendicular component, whose morphology, position and spectral index suggest that it is tracing an accretion-driven radio jet. In the following we discuss in more detail the nature of both free-free components.

5.4.1 Accretion-driven radio jet

As mentioned above, our 3.0 cm observations indicate the presence of a radio jet in GM Aur. A similar result was recently found in AB Aur (Rodríguez et al. 2014). Even though AB Aur is associated with a transitional disk, it has a relatively high mass accretion rate of $\dot{M}_{\rm acc} \simeq 1.4 \times 10^{-7}$ $M_\odot$ yr^{-1} (Salyk et al. 2013). GM Aur, on the other hand, presents a much lower $\dot{M}_{\rm acc} \simeq$ (0.4-1) $\times 10^{-8}$ $M_\odot$ yr^{-1} (Ingleby et al. 2015). Despite this difference of more than one order of magnitude, our high sensitivity observations have allowed us to detect a radio jet in GM Aur. Therefore, our results indicate that transitional disks, even those with very low mass accretion rates, may be associated with ionized jets.

From our two-Gaussian fit we estimated a flux density of ~ 45 μJy at 3.0 cm for the radio jet of GM Aur. Following a similar analysis to that of Rodríguez et al. (2014), we can test whether this jet follows the empirical correlation obtained by Anglada (1995) and Anglada, Rodríguez & Carrasco-González (2015) between the radio luminosity ($S_\nu d^2$) at 3.6 cm and the bolometric luminosity (L_{bol}). Using $L_{bol} \simeq 0.9$ $L_\odot$ for GM Aur as well as the free-free spectral index obtained in §3, the correlation predicts a flux density at 3.0 cm of ~ 440 μJy, which is a factor of ~ 10 higher than our measured value. A similar result was found by Rodríguez et al. (2014) in AB Aur, where the flux density obtained with the correlation was a factor

~ 20 higher than the measured value. The reason for this discrepancy is attributed to the fact that the correlation was obtained for younger sources (class 0 and I), where the bolometric luminosity is dominated by the accretion luminosity. On the contrary, in sources with transitional disks, which have much lower mass accretion rates, the luminosity is dominated by the stellar component. These results suggest that the previous correlation actually relates the accretion luminosity, traced by L_{bol} in very young objects, and the ejection of material, traced by the free-free emission of the radio jet.

The accretion and outflow rates can be compared applying the empirical correlation between the momentum rate of the outflow ($\dot{P}_{\rm out}$) and the radio luminosity (Anglada 1995; Anglada, Rodríguez & Carrasco-González 2015):

$$\left(\frac{S_\nu d^2}{\rm mJy\ kpc^2}\right) = 190 \left(\frac{\dot{P}_{\rm out}}{M_\odot\ {\rm yr^{-1}\ km\ s^{-1}}}\right)^{0.9}. \quad (5.1)$$

Using our estimated flux density of ~ 45 μJy for the radio jet at 3.0 cm we obtain $\dot{P}_{\rm out} \simeq 1.0 \times 10^{-6}$ $M_\odot$ yr^{-1} km s^{-1}. Assuming a jet terminal velocity of $\sim$ 200–300 km s^{-1} (Cabrit 2007), we estimate a mass loss rate $\dot{M}_{\rm out} \simeq 3$–$5 \times 10^{-9}$ $M_\odot$ yr^{-1} for the jet of GM Aur, one of the lowest mass loss rates ever obtained for a jet. Ingleby et al. (2015) measured a variable mass accretion rate in GM Aur of $\dot{M}_{\rm acc} = 0.4$–1.1×10^{-8} $M_\odot$ yr^{-1} within a time span of ~ 3.5 months. Taking into account this variability in the accretion rate, as well as the observed dispersion in the empirical correlation derived by Anglada (1995) and Anglada, Rodríguez & Carrasco-González (2015), we conclude that our estimated mass loss rate for the jet of GM Aur is consistent with a ratio $\dot{M}_{\rm out}/\dot{M}_{\rm acc} \simeq 0.1$, typical of younger objects (Cabrit 2007). A similar result was obtained by Rodríguez et al. (2014) for the transitional disk of AB Aur. Thus, our results indicate that, even though accretion decreases as a star evolves, the ratio between accretion rate and outflow rate in the jet remains similar, suggesting that a similar ejection mechanism persists during the whole process of star formation.

5.4.2 Photoevaporating disk

Pascucci et al. (2012) studied the free-free emission at cm wavelengths produced by a

photoevaporating disk assuming that the disk is heated by EUV or X-ray radiation. They obtained the following relations:

$$\left(\frac{S_\nu}{\mu\mathrm{Jy}}\right) = 2.9 \times 10^{-39} \left(\frac{51\ \mathrm{pc}}{d}\right)^2 \left(\frac{\Phi_{\mathrm{EUV}}}{\mathrm{s}^{-1}}\right), \tag{5.2}$$

$$\left(\frac{S_\nu}{\mu\mathrm{Jy}}\right) = 2.4 \times 10^{-29} \left(\frac{51\ \mathrm{pc}}{d}\right)^2 \left(\frac{L_X}{\mathrm{erg\ s}^{-1}}\right). \tag{5.3}$$

where S_ν is the flux density at 3.5 cm, Φ_{EUV} is the EUV photon luminosity, and L_X is the X-ray luminosity (Pascucci et al. 2012). Owen et al. (2013) extended this analysis with numerical calculations and obtained similar results. From equation (3), one can estimate the free-free emission produced by the X-ray-heated gas if the stellar X-ray luminosity (L_X) is known. The measured L_X for GM Aur is $\sim 1.6 \times 10^{30}$ erg s^{-1} (Güdel et al. 2010), which would produce a flux density of only ~ 5.7 μJy at 3.0 cm. This value is much lower than our estimated flux density of $\sim 31 \pm 3$ μJy at 3.0 cm for the free-free emission of the photoevaporating disk, which indicates that in GM Aur the photoionization of the gas cannot be only produced by X-rays, and should be mainly due to EUV radiation. Following equation (2), we obtain that a $\Phi_{\mathrm{EUV}} \simeq 5.8 \times 10^{40}$ s^{-1} is required to account for the remaining ~ 25 μJy of the observed free-free emission from the photoevaporative wind in GM Aur.

Since EUV photons are highly absorbed by H, only indirect measurements of Φ_{EUV} from T Tauri stars can be performed. Using forbidden line observations, EUV photon luminosities $\sim 10^{41}$-10^{44} s^{-1} have been inferred (Alexander et al. 2005; Espaillat et al. 2013). Recently, following Pascucci et al. (2012) prescriptions, Galván-Madrid et al. (2014) and Pascucci et al. (2014) estimated $2 \times 10^{40} \lesssim \Phi_{\mathrm{EUV}} \lesssim 10^{42}$ s^{-1} using radio observations of different transitional disks. Our estimated EUV photon luminosity for GM Aur is close to the lower limit of these latter measurements. However, none of the previous studies took into account the possible contribution of a radio jet. Our observations have allowed us to separate both components of the free-free emission, resulting in a lower but probably more accurate estimate of Φ_{EUV}.

In particular, Owen et al. (2013) and Pascucci et al. (2014) estimated a higher value of $\Phi_{\mathrm{EUV}} \simeq 2 \times 10^{41}$ s^{-1} for GM Aur based mostly on Arcminute Microkelvin Imager Large Array (AMI-LA) observations. Due to the low angular resolution of

their observations (beam=39.″4 × 25.″0), these authors were not able to separate the radio jet emission reported in this paper or the contribution of nearby sources that could fall within the large beam of AMI-LA from the free-free emission from the photoevaporative winds. Our 3.0 cm observations show, in fact, a nearby source ($\sim 28''$ away) with almost the same flux density as GM Aur that was not separated by the AMI-LA observations.

It is worth noting that the $\Phi_{\rm EUV}$ estimated from the observed photoionized gas actually represents the EUV radiation impinging on the disk, which could differ from the EUV radiation produced by the star. Hollenbach & Gorti (2009) showed that accretion flows and jets could significantly shield the disk from EUV and soft (~ 0.1 keV) X-ray radiation. According to their model, EUV and soft X-ray photons can completely cross a jet only if its mass loss rate is $\dot{M}_{out} \lesssim 8{\times}10^{-10}\ M_\odot\ {\rm yr}^{-1}$. In the case of GM Aur, our estimated $\dot{M}_{\rm out} \simeq$ (3-5) $\times 10^{-9}\ M_\odot\ {\rm yr}^{-1}$in the jet is above this value. This implies that the $\Phi_{\rm EUV}$ reaching the disk and, therefore, our estimated values, could be significantly lower than the $\Phi_{\rm EUV}$ produced by the star. As the accretion rate and, thus, the ejection rate of the jet decrease, the high-energy radiation impinging on the disk could increase, accelerating the photoevaporation of the disk. A larger sample of protoplanetary disks with a good determination of both $\Phi_{\rm EUV}$ and $\dot{M}_{\rm out}$ of the jet would be needed to test this scenario and its impact on the timescale of disk dispersal.

In any case, the low $\Phi_{\rm EUV}$ estimated from radio observations indicates that EUV radiation alone is probably not enough to disperse the disk in the timescale required by observations (Pascucci et al. 2014). Equation (4) in Alexander et al. (2014) can be used to estimate the mass loss rate in a fully-ionized photoevaporative wind launched purely by EUV radiation:

$$\left(\frac{\dot{M}_{\rm w,EUV}}{M_\odot\ {\rm yr}^{-1}}\right) \simeq 1.6\times10^{-10}\left(\frac{\Phi_{\rm EUV}}{10^{41}\ {\rm s}^{-1}}\right)^{1/2}\left(\frac{M_*}{M_\odot}\right)^{1/2}. \quad (5.4)$$

From this equation we obtain that the estimated $\Phi_{\rm EUV}$ for GM Aur would launch a photoevaporative wind with a mass loss rate of only $\dot{M}_{\rm w,EUV} \simeq 1.3\times10^{-10}\ M_\odot\ {\rm yr}^{-1}$. This value is much lower than the measured mass accretion rate of $\dot{M}_{\rm acc} = (0.4\text{–}1.1)\times10^{-8}\ M_\odot\ {\rm yr}^{-1}$ (Ingleby et al. 2015), suggesting that EUV photons are currently

not able to release a significant amount of gas from the disk. Alternatively, X-rays can penetrate much deeper into the disk than EUV radiation and, thus, they can launch a denser, but only partially ionized, photoevaporative wind (Gorti, Dullemond & Hollenbach 2009; Owen et al. 2011). A quantitative estimate of the mass loss rate from X-ray photoevaporation ($\dot{M}_{w,X}$) is still subject to significant uncertainties, since several input parameters and discrepancies between the models are not yet well understood (Alexander et al. 2014). Nonetheless, theoretical models predict mass loss rates between 1 and 2 orders of magnitude higher than those produced by EUV radiation for a star like GM Aur. Therefore, even though our results indicate that X-rays are not contributing significantly to the ionization of the photoevaporative wind, according to the models they could be responsible for most of the mass loss rate of the photoevaporating disk (Pascucci et al. 2014).

5.5 Summary and conclusions

We analyzed the results of multi-configuration VLA observations at Q, Ka, K, X, and C bands towards the transitional disk of GM Aur, revealing the presence of dust thermal and free-free emission at cm wavelengths.

At 3 cm the emission presents an angularly resolved tripolar morphology that we separate into three components: the dust emission from the GM Aur disk, the free-free emission from a radio jet perpendicular to it, and the free-free emission from a photoevaporative wind arising from the disk. This is the first time that free-free emission from disk photoevaporation in a low mass star has been spatially resolved and separated from other components.

We conclude that extreme-UV (EUV) radiation is the main agent responsible for the ionization of the photoevaporative wind in GM Aur, although requiring a low photon luminosity of $\Phi_{\rm EUV} \simeq 6 \times 10^{40}$ s^{-1}. This low EUV photon luminosity produces a mass loss rate of only $\dot{M}_{w,EUV} \simeq 1.3 \times 10^{-10}$ $M_\odot$ yr^{-1}. Therefore, other mechanisms, such as X-ray photoevaporation, are required to disperse the disk in the timescale imposed by observations.

On the other hand, we estimate a mass loss rate in the radio jet in GM Aur of $\dot{M}_{\rm out} \simeq$ (3-5) $\times 10^{-9}$ $M_\odot$ yr^{-1}, which represents one of the lowest mass ejection rates in a jet estimated so far. Nevertheless, the ratio $\dot{M}_{out}/\dot{M}_{acc} \simeq 0.1$, typical of younger

protostars, seems to be valid as well for GM Aur. Therefore, our results suggest that disks with very low mass accretion rates still present collimated ejections of material, apparently following the same physical mechanisms as much younger protostars

At least in GM Aur, the cm free-free emission of the jet and the photoevaporative wind seem to be of the same order. Future radio observations aiming to study photoevaporation in the last stages of disk evolution should be cautious and try to disentangle the contribution to the observed radio emission of the dust, the jet, and the photoevaporative winds.

6

Conclusions

In this thesis we have presented the results of an observational and modeling study of accretion disks around young stellar objects (YSOs) that are in the first stages of planetary formation. We have reported high angular resolution observations at mm and cm wavelengths toward three different transitional disks (HD 169142, XZ Tau B, and GM Aur) obtained with the Very Large Array (VLA) and the Atacama Large Millimeter/Submillimeter Array (ALMA). These observations have allowed us to study the thermal emission of the large dust grains in the disks as well as the thermal free-free emission from ionized gas. In addition, we have complemented these observations with the modeling of the dust thermal emission using self-consistent radiative transfer codes that calculate the temperature and density distribution, as well as the observable dust emission, of irradiated accretion disks. Our main conclusions can be summarized as follows:

- Our VLA observations at 7 and 9 mm of the transitional disk of HD 169142 have revealed the presence of a system of at least three gaps, each $\sim 0\farcs20$ in width ($\sim$ 30 au at 145 pc), with outer radii of $\sim 0\farcs20$, $\sim 0\farcs48$, and $\sim 0\farcs83$ ($\sim$ 30, $\sim$ 70, and $\sim$ 120 au, respectively). A bright and narrow clumpy ring of emission is observed at a radius of $\sim$ 32 au, which we interpret to be tracing the rim of the inner gap. Unlike other sources, the radii of this structure of gaps and rings are similar to those obtained from near-infrared polarimetric images, suggesting that the radial distribution of micron-sized dust grains in the disk

atmosphere (traced by the IR images) is similar to that of the large dust grains (mm-cm sized).

- We speculate that the clumpy ring of emission of the HD 169142 disk could have become gravitationally unstable due to a pile-up of material produced by the dynamical interaction with the forming planets. As a consequence, the ring could be fragmenting into clumps that may end up forming new planets.

- We have modeled the broadband SED as well as the 7 mm images of the disk. From this modeling we estimate that the disk has a mass of $\sim 120\ M_J$ and a relatively low degree of settling. Furthermore, we have inferred the presence of a small ($\sim$ 0.6 au in radius) residual inner disk located very close to the star, implying that the disk is actually a pre-transitional disk. We also infer an accumulation of large dust grains at the outer edges of the gaps in the disk.

- Our highest angular resolution VLA observations toward HD 169142 have revealed a compact component of emission whose peak is located at a projected distance of $\sim$ 4 au from the center. The flux density of this component is higher than our estimated dust emission for the residual inner disk. This, together with the low value of the spectral index of this component, indicates that this emission is dominated by free-free emission from ionized gas, which could be associated with an inhomogeneous photoionization of the inner disk, with an independent object, or with an (asymmetric) ionized jet. We favor the latter scenario and speculate that this jet might be significantly photoionized by the high energy radiation emitted from the central star.

- Based on our observational and modeling results, we suggest that the two inner gaps in the disk of HD 169142 could be created by dynamical interactions between the disk and forming planets, while the outer and shallower gap might be associated with dust growth and trapping close to the CO snowline. This is the third case (the second transitional disk) in which a well-defined multiple-gap structure has been observed. This type of structures are probably frequent in protoplanetary disks and could indicate the presence of multiple planet formation. We expect that the number of detections of these structures, as well as

the understanding of their role in the planetary formation process, will increase significantly in the next few years.

- We have analyzed ALMA observations at 1.3 mm toward the pre-main sequence star XZ Tau B. The dust thermal emission shows the presence of a dwarf transitional disk $\sim$ 3.4 au in radius with an inner cavity of radius $\sim$ 1.3 au. The image shows a slight azimuthal asymmetry that could be associated with a dust trap.

- We model the dust emission of the disk around XZ Tau B and show that its surface density is higher than the values expected at the inner regions of larger disks around similar stars. We suggest that this high densities might be related to the origin of the triple stellar system XZ Tau, where XZ Tau B is located. In this scenario, a massive primordial disk could have been gravitationally unstable and could have fragmented into the three stars of the system.

- We performed hydrodynamical simulations to study the survivability and capability to form planets of such a small disk as XZ Tau B. These simulations, together with our modeling and observational results, suggest that XZ Tau B could be undergoing the formation of a planetary system, which could in turn be the responsible for the observed gap. We suggest that dwarf disks similar to that of XZ Tau B could be the progenitors of compact planetary systems such as those detected in the exoplanet surveys.

- Due to the very small sizes involved in the XZ Tau B transitional disk, the dynamical evolution of the system is expected to be much faster than in classical larger disks. We expect changes in the morphology of the mm emission in timescales of a few months, compared to the timescales of decades expected for larger disks. This opens up the possibility of monitoring the evolution of the system with new observations in the near future.

- We have reported the results of a multi-frequency study performed with the VLA toward the transitional disk of GM Aur. Our radio continuum observations have allowed us to spatially resolve and separate, for the first time, the three main components at work in this stage of the disk evolution: the disk of

dust, the ionized radio jet perpendicular to it, and the photoevaporative wind arising from the surface of the disk.

- The estimated mass loss rate of the radio jet in GM Aur is consistent with the ratio between ejection and accretion rates found in younger objects, which supports the idea that transitional disks can still power collimated ejections of material apparently following the same physical mechanisms as much younger protostars.

- Our results indicate that extreme-UV (EUV) radiation is the main ionizing mechanism of the photoevaporative wind traced by the free-free emission observed at cm wavelengths in GM Aur. The EUV photon luminosity inferred from the observed free-free emission is too low to produce the mass loss rates needed to disperse the disk in the timescales imposed by observations ($\lesssim$ 10 Myr). Therefore, we conclude that other additional mechanisms, such as X-ray-driven photoevaporation (which can launch a denser but only partially ionized wind), are required.

6.1 Future work

The work presented in this thesis has opened several research lines that will be pursued in the near future. On the modeling perspective, we plan to keep improving the self-consistent radiative transfer codes initially developed by D'Alessio et al. (1999; 1999; 2001) that have been used in this thesis to model the dust emission of accretion disks. In particular, we have started to adapt the codes to include several physical mechanisms, such as radial migration or dust grain trapping, that are signatures of planet formation and can be playing an important role during the last stages of disk evolution. In addition to the dust component, we plan to include in the code the gas component, whose treatment is more complex but can provide a more complete information. We plan to calculate the spectral line emission for several relevant molecular species, which can provide us with important information about the physical and chemical conditions in the disk. The line emission of these molecules strongly depends on the physical properties of the gas, which in turn affect the disk chemistry and produce important variations of the abundance of the molecular species. Thus,

we plan to calculate the temperature and density of the gas independently from the calculation of the dust, taking into account the high energy irradiation and chemistry in the disk. In this way we will be able to obtain the abundance distribution of several molecules and then calculate its observable line emission. All these improvements should be very useful to analyze and study the complex observational data resulting from the great capabilities of the VLA and ALMA.

On the observational perspective, ALMA is currently pushing for a very rapid evolution of the field as it moves toward its full capabilities. Observations making use of the extremely high sensitivity and angular resolution provided by ALMA will certainly produce very important results in the very near future. Dust continuum observations with ALMA will be able to determine whether ringed substructures and annular gaps are ubiquitous in protoplanetary disks. Combining continuum observations with molecular line observations will help us understand the importance of snow lines in the creation of these gaps. The detection of circumplanetary material associated with forming planets has still been elusive, but it will be of crucial importance in order to understand the planetary formation process. The extremely high sensitivity of ALMA will probably be able to detect this emission in the near future. Additionally, the great sensitivity of ALMA offers the oportunity to perform large unbiased surveys that will uncover the true diversity of protoplanetary disks and their relationship with the final architecture of the resulting planetary systems. In particular, our study of the disk of XZ Tau B has proven that the properties of accretion disks around YSOs can reach values much more extreme than previously thought. In the near future, these surveys will be very important to expand the sample of observed protoplanetary disks in general, and transitional disks in particular. Finally, the combination of dust continuum observations with ALMA and VLA at multiple optically thin wavelengths will allow us to map the spectral index and to infer the dust grain size distribution throughout the disk. This type of studies have been performed in a few cases, but a much larger sample will be needed to improve our understanding of dust grain growth and transport processes in protoplanetary disks, which are very relevant to understand the planetary formation process. We have obtained ALMA observing time to perform a similar study in the transitional disk around HD 169142 combining ALMA and VLA data. In addition, we have also been granted with ALMA observing time to obtain very sensitive follow-up observa-

tions of XZ Tau B that will allow us to study in detail the properties of its dwarf transitional disk and to discern the cause of its small size.

In this thesis we have presented pioneering results on the detailed structure of transitional disks at 7 mm and 3 cm with the VLA. These studies have shown the distribution of mm-sized dust grains and have started to reveal the impact of the ionized gas in the evolution of these disks. We plan to extend this kind of studies to a larger sample of sources in the near future. In the longer term, the advent of the Square Kilometre Array (SKA) will prompt a huge improvement of our understanding of these issues. Its foreseen extremely high sensitivity and angular resolution at cm wavelengths will allow us to study the emission from very large dust grains (pebbles), revealing the very last stages in grain growth previous to the formation of planetary bodies. SKA will also allow us to study the ionized component associated with these disks with the highest degree of detail ever achieved (e.g., Anglada et al. 2015). Our first results on GM Aur with the VLA have shown that it is feasible to separate at cm wavelengths the dust emission of the disk, the free-free emission of the ionized jet, and that of the photoevaporating disk. SKA should be able to obtain more accurate images, allowing us to better understand the role of these components in ending the accretion process, dispersing the gas in protoplanetary disks, and shaping the resulting planetary system.

A

Appendix: Dust settling and radial migration

Large dust grains in accretion protoplanetary disks suffer a drag force that tends to move them toward pressure maxima in the disk. This results in a vertical settling toward the midplane and an inward migration of the mm-sized dust particles. Small grains, on the other hand, are coupled to the gas and can, therefore, distribute homogeneously with the gas. As a consequence, the large dust grains are expected to be more concentrated in the midplane and inner regions of the disk in comparison to the small dust grains.

In order to take into account dust settling, our model includes two populations of grains: a population of small dust grains in the upper layers of the disk and a population of larger dust grains in the midplane (D'Alessio et al. 2006). The size distribution of both of these populations is a power law $n(a) \propto a^{-p}$, where p is usually assumed to be 3.5, as in the interstellar medium (ISM). The minimum and maximum sizes of the dust grains in both populations are parameters that can be adjusted to fit the observational data, although usual values are $a_{\rm min} = 0.005$ μm and $a_{\rm max} = 0.25$–1 μm (similar to the ISM) in the upper layers of the disk, and $a_{\rm min} = 0.005$–1 μm and $a_{\rm max} = 1$–10 mm in the disk midplane.

The dust surface density of the large grains population located in the midplane,

Σ^d_{down}, at a certain radius, r, is given by:

$$\Sigma^d_{\rm down}(r) = 2\,\zeta_{\rm big} \int_0^{z_{\rm big}} \rho(r,z)\,dz, \tag{A.1}$$

where $\zeta_{\rm big}$ is the dust-to-gas mass ratio of the large dust grains population, $\rho(r,z)$ is the volumetric density of the gas, and $z_{\rm big}$ is the height above the midplane of the transition between the two dust populations. Following the same idea, the dust surface density that has been lost or transfered from the upper layers of the disk to the midplane because of dust settling is:

$$\Sigma^d_{\rm up,lost}(r) = 2\,\zeta_{\rm tot} \int_{z_{\rm big}}^{\infty} \rho(r,z)\,dz - 2\,\zeta_{\rm small} \int_{z_{\rm big}}^{\infty} \rho(r,z)\,dz, \tag{A.2}$$

where $\zeta_{\rm tot}$ is the total dust-to-gas mass ratio in the disk and $\zeta_{\rm small}$ is the dust-to-gas mass ratio of the small grains population in the disk upper layers.

We can now apply a simple conservation equation such as:

$$\Sigma^d_{\rm down}(r) = 2\,\zeta_{\rm tot} \int_0^{z_{\rm big}} \rho(r,z)\,dz + \Sigma^d_{\rm up,lost}(r), \tag{A.3}$$

i.e., all the dust mass that has been lost in the upper layers of the disk has to be in the large dust grain population in the disk midplane.

Combining equations A.1, A.2, and A.3 we get:

$$\zeta_{\rm big} = \zeta_{\rm tot} + \left(\zeta_{\rm tot} - \zeta_{\rm small}\right) \frac{\int_{z_{\rm big}}^{\infty} \rho(r,z)\,dz}{\int_0^{z_{\rm big}} \rho(r,z)\,dz}. \tag{A.4}$$

In the proximity of the disk midplane, the temperature distribution is isothermal in height, so the gas volumetric density can be approximated as (Hartmann 2009):

$$\rho(r,z) = \rho_0 \exp\!\left(-\frac{z^2}{2H^2}\right), \tag{A.5}$$

where

$$H(r) = \left(\frac{r^3 c_s^2}{G\,M_*}\right)^{1/2} \tag{A.6}$$

is the local gas scale height of the disk, r is the radial coordinate, c_s is the sound

speed, G is the universal gravitation constant, and M_* is the stellar mass. Thus, assuming that $z_{\rm big}$ is a small fraction of the gas scale height ($z_{\rm big} = \delta H$), we obtain:

$$\int_0^{\delta H} \rho(z)\, dz = \sqrt{2}\, \rho_0\, H \int_0^{\delta/\sqrt{2}} \exp(-s^2) ds = \rho_0\, H \sqrt{\frac{\pi}{2}}\, \mathrm{erf}\left(\frac{\delta}{\sqrt{2}}\right), \tag{A.7}$$

where $\mathrm{erf}(x)$ is the error function, defined as:

$$\mathrm{erf}(x) = \frac{2}{\sqrt{\pi}} \int_0^x \exp(-s^2) ds, \tag{A.8}$$

where $\mathrm{erf}(\infty) = 1$.

Therefore, considering that $\int_{z_{\rm big}}^{\infty} \rho\, dz = \int_0^{\infty} \rho\, dz - \int_0^{z_{\rm big}} \rho\, dz$, we obtain:

$$\zeta_{\rm big} = \zeta_{\rm tot} + \left(\zeta_{\rm tot} - \zeta_{\rm small}\right)\left(\frac{1}{\mathrm{erf}\left(\frac{\delta}{\sqrt{2}}\right)} - 1\right). \tag{A.9}$$

Equation A.9 gives us the relation between the dust-to-gas mass ratio in the midplane ($\zeta_{\rm big}$) and in the upper layers of the disk ($\zeta_{\rm small}$) for a given radius. This equation can be also written in terms of the degree of settling, defined as the quantity $\epsilon = \zeta_{\rm small}/\zeta_{\rm tot}$:

$$\frac{\zeta_{\rm big}}{\zeta_{\rm tot}} = 1 + \left(1 - \epsilon\right)\left(\frac{1}{\mathrm{erf}\left(\frac{\delta}{\sqrt{2}}\right)} - 1\right). \tag{A.10}$$

If we want to include radial migration of large dust grains, we can include a radial dependency of the total dust-to-gas mass ratio. Since small grains are coupled to the gas, one could in principle set $\zeta_{\rm small}$ as constant with radius, so that equation A.9 gives the value of $\zeta_{\rm big}$ as a function of radius.

Bibliography

Adams, F. C., Lada, C. J., & Shu, F. H. 1987, ApJ, 312, 788

Alexander, R. 2008, MNRAS, 391, L64

Alexander, R. D., Clarke, C. J., & Pringle, J. E. 2005, MNRAS, 358, 283

Alexander, R. D., Clarke, C. J., & Pringle, J. E. 2006, MNRAS, 369, 216

Alexander, R., Pascucci, I., Andrews, S., Armitage, P., & Cieza, L. 2014, in Protostars and Planets VI, ed. H. Beuther et al. (Tucson, AZ: Univ. Arizona Press), 475

ALMA Partnership, Brogan, C. L., Pérez, L. M., et al. 2015, ApJ, 808, L3

ALMA Partnership, Fomalont, E. B., Vlahakis, C., et al. 2015, ApJ, 808, L1 (AP2015b)

Andre, P., Ward-Thompson, D., Barsony, M. 1993, ApJ, 406, 122

Andrews, S. M. 2015, PASP, 127, 961

Andrews, S. M., Rosenfeld, K. A., Kraus, A. L, Wilner, D. J. 2013, ApJ, 771, 129

Andrews, S. M., Wilner, D. J., Espaillat, C., et al. 2011, ApJ, 732, 42

Andrews, S. M., Wilner, D. J., Hughes, A. M., Qi, C., & Dullemond, C. P. 2009, ApJ, 700, 1502

Andrews, S. M., Wilner, D. J., Zhu, Z., et al. 2016, ApJ, 820, L40

Anglada, G. 1989, PhD thesis, Universitat de Barcelona

Anglada, G. 1995, RMxAC, 1, 67

Anglada, G. 1996, Radio Emission from the Stars and the Sun, ASP Conf. Ser., 93, 3

Anglada, G., Rodríguez, L. F., & Carrasco-González, C. 2015, in Advancing Astrophysics with the Square Kilometre Array (AASKA14), 121

Anglada, G., Tafalla, M., Carrasco-González, C., et al. 2015, in Spanish SKA White Book, ed. M. Pérez-Torres et al., 169

Ardila, D. R., Golimowski, D. A., Krist, J. E., et al. 2007, ApJ, 665, 512

Avalos, M., Lizano, S. 2012, ApJ, 751, 63

Avenhaus, H., Quanz, S. P., Schmid, H. M., et al. 2014, ApJ, 781, 87

Bai, X.-N. 2013, ApJ, 772, 96

Bai, X.-N., & Stone, J. M. 2014, ApJ, 796, 31

Baruteau, C., Cirda, A., Paardekooper, S.-J., et al. 2014, in Protostars and Planets VI, ed. H. Beuther et al. (Tucson, AZ: Univ. Arizona Press), 667

Beckwith, S. V. W., Sargent, A. I. 1991, ApJ, 381, 250

Biller, B. A., Males, J., Rodigas, T., et al. 2014, ApJ, 792, L22

Birnstiel, T., Andrews, S. M., & Ercolano, B. 2012, A&A, 544, A79

Birnstiel, T., Dullemond, C. P., & Brauer, F. 2009, A&A, 503, L5

Birnstiel, T., Dullemond, C. P., & Brauer, F. 2010, A&A, 513, A79

Birnstiel, T., Dullemond, C. P., & Pinilla, P. 2013, A&A, 550, L8

Blaes, O. M., & Balbus, S. A. 1994, ApJ, 421, 163

Blondel, P. F. C., Djie, H. R. E. T. A. 2006, A&A, 456, 1045

Blum, J., & Wurm, G. 2008, ARA&A, 46, 21

Brauer, F., Dullemond, C. P., & Henning, T. 2008, A&A, 480, 859

Brittain, S. D., Carr, J. S., Najita, J. R., et al. 2014, ApJ, 791, 136

Brittain, S. D., Najita, J. R., Carr, J. S., Ádámkovics, M., Reynolds, N. 2016, arXiv:1608.00986

Brown, J. M., Blake, G. A., Qi, C., et al. 2009, ApJ, 704, 496

Brown, J. M., Rosenfeld, K. A., Andrews, S. M., Wilner, D. J., & van Dishoeck, E. F. 2012, ApJ, 758, L30

Burrows, C. J., Stapelfeldt, K. R., Watson, A. M., et al. 1996, ApJ, 473, 437

Cabrit, S. 2007, in IAU Symp. 243, Star-Disk Interaction in Young Stars, ed. J. Bouvier & I. Appenzeller (Cambridge: Cambridge Univ. Press), 203

Calvet, N., D'Alessio, P., Hartmann, L., et al. 2002, ApJ, 568, 1008

Calvet, N., D'Alessio, P., Watson, D. M., et al. 2005, ApJ, 630, L185

Calvet, N., & Gullbring, E. 1998, ApJ, 509, 802

Carrasco-González, C., Galván-Madrid, R., Anglada, G., et al. 2012, ApJ, 752, L29

Carrasco-González, C., Henning, T., Chandler, C. J., et al. 2016, ApJ, 821, L16

Carrasco-González, C., Rodríguez, L. F., Anglada, G., & Curiel, S. 2009, ApJ, 693, L86

Clarke, C. J., Gendrin, A., & Sotomayor, M. 2001, MNRAS, 328, 485

Casassus, S., van der Plas, G., M, S. P., et al. 2013, Nature, 493, 191

Coffey, D., Downes, T. P., & Ray, T. P. 2004, A&A, 419, 593

Cohen, M., Kuhi, L. V. 1979, ApJS, 41, 743

D'Alessio, P. 1996, PhD thesis, Univ. Nacional Autónoma de México

D'Alessio, P., Calvet, N., & Hartmann, L. 2001, ApJ, 553, 321

D'Alessio, P., Calvet, N., Hartmann, L., Franco-Hernández, R., & Servín, H. 2006, ApJ, 638, 314

D'Alessio, P., Calvet, N., Hartmann, L., Lizano, S., & Cantó, J. 1999, ApJ, 527, 893

D'Alessio, P., Cantó, J., Calvet, N., & Lizano, S. 1998, ApJ, 500, 411

D'Alessio, P., Hartmann, L., Calvet, N., et al. 2005, ApJ, 621, 461

de Gregorio-Monsalvo I., Ménard, F., Dent, W., et al. 2013, A&A, 557, A133

Dempsey, J. T., Friberg, P., Jenness, T., et al. 2013, MNRAS, 430, 2534

Dent, W. R. F., Torrelles, J. M., Osorio, M., Calvet, N., & Anglada, G. 2006, MNRAS, 365, 1283

Dong, R., Zhu, Z., & Whitney, B. 2015, ApJ, 809, 93

Draine, B. T. 2006, ApJ, 636, 1114

Draine, B. T., & Lee, H. M. 1984, ApJ, 285, 89

Drążkowska, J., & Dullemond, C. P. 2014, A&A, 572, A78

Dubrulle, B., Morfill, G., & Sterzik, M. 1995, Icar, 114, 237

Dullemond, C. P., & Dominik, C. 2004, A&A, 421, 1075

Dullemond, C. P., & Dominik, C. 2005, A&A, 434, 971

Dupuy, T. J., Kratter, K. M., Kraus, A. L., et al. 2016, ApJ, 817, 80

Dutrey, A., Guilloteau, S., Prato, L., et al. 1998, A&A, 338, L63

Dzib, S. A., Loinard, L., Rodríguez, L. F., Galli, P. 2014, ApJ, 788, 162

Ercolano, B., Owen, J. E. 2010, MNRAS, 406, 1553

Espaillat, C., Calvet, N., D'Alessio, P., et al. 2007, ApJ, 670, L135

Espaillat, C., D'Alessio, P., Hernández, J., et al. 2010, 717, 441

Espaillat, C., Ingleby, L., Furlan, E., et al. 2013, ApJ, 762, 62

Espaillat, C., Calvet, N., Luhman, K. L., Muzerolle, J., & D'Alessio, P. 2008, ApJ, 682, L125

Espaillat, C., Muzerolle, J., Najita, J., et al. 2014, in Protostars and Planets VI, ed. H. Beuther et al. (Tucson, AZ: Univ. Arizona Press), 497

Flock, M., Ruge, J. P., Dzyurkevich, N., et al. 2015, A&A, 574, A68

Font, A., McCarthy, I., Johnstone, D., Ballantyne, D. R. 2004, ApJ, 607, 890

Forgan, D., Ivison, R. J., Sibthorpe, B., Greaves, J. S., & Ibar, E. 2014, MNRAS, 439, 4057

Fromang, S., & Nelson, R. P. 2009, A&A, 496, 597

Furlan, E., Fischer, W. J., Ali, B., et al. 2016, ApJS, 224, 5

Gaia Collaboration, Brown, A. G. A., Vallenari, A., et al. 2016, arXiv:160904172

Galván-Madrid, R., Liu, H. B., Manara, C. F. 2014, A&A, 570, L9

Garufi, A., Quanz, S. P., Avenhaus, H., et al. 2013, A&A, 560, A105

Gorti, U., Dullemond, C. P., & Hollenbach, D. 2009, ApJ, 705, 1237

Gorti, U., & Hollenbach, D. 2009, ApJ, 690, 1539

Grady, C. A., Devine, D., Woodgate, B., et al. 2000, ApJ, 544, 895

Grady, C. A., Schneider, G., Hamaguchi, K., et al. 2007, ApJ, 665, 1391

Güdel, M., Lahuis, F., Briggs, K. R., Carr, J., et al. 2010, A&A, 519, 113

Gundlach, B., Kilias, S., Beitz, E., , & Blum, J. 2011, Icar, 214, 717

Hartigan, P., Edwards, S., & Ghandour, L. 1995, ApJ, 452, 736

Hartigan, P., & Kenyon, S. J. 2003, ApJ, 583, 334

Hartmann, L. 2009, Accretion Processes in Star Formation, 2nd ed. (Cambridge, UK: Cambridge University Press)

Hartmann, L., Calvet, N., Gullbring, E., & D'Alessio, P. 1998, ApJ, 495, 385

Hartmann, L., Herczeg, G., & Calvet, N. 2016, ARA&A, 54, 135

Hashimoto, J., Dong, R., Kudo, T., et al. 2012, ApJ, 758, L19

Henney, W. J., & O'Dell, C. R. 1999, AJ, 118, 2350

Hioki, T., Itoh, Y., Oasa, Y., et al. 2009, PASJ, 61, 1271

Hollenbach, D., Gorti, U. 2009, ApJ, 703, 1203

Honda, M., Maaskant, K., Okamoto, Y. K., et al. 2012, ApJ, 752, 143

Hughes, A. M., Andrews, S. M., Espaillat, C., et al. 2009, ApJ, 698, 131

Hughes, A. M., Wilner, D. J., Andrews, S. M., Qi, C., & Hogerheijde, M. R. 2011, ApJ, 727, 85

Hughes, A. M., Wilner, D. J., Calvet, N., et al. 2007, ApJ, 664, 536

Ingleby, L., Calvet, N., Herczeg, G., & Briceño, C. 2012, ApJ, 752, L20

Ingleby, L., Espaillat, C., Calvet, N., et al. 2015, ApJ, 805, 149

Isella, A., Chandler, C., Carpenter, J. M., Pérez, L. M., & Ricci, L. 2014, ApJ, 788, 129

Isella, A., Pérez, L. M., & Carpenter, J. M. 2012, ApJ, 747, 136

Isella, A., Pérez, L. M., Carpenter, J. M., et al. 2013, ApJ, 775, 30

Jang-Condell, H., & Turner, N. J. 2012, ApJ, 749, 153

Jontof-Hutter, D., Rowe, J. F., Lissauer, J. J., Fabrycky, D. C., & Ford, E. B. 2015, Nature, 522, 321

Kenyon, S. J., Hartmann, L. 1987, ApJ, 323, 714

Kenyon, S. J., Hartmann, L. 1995, ApJS, 101, 117

Kitamura, Y., Momose, M., Yokogawa, S., et al. 2002, ApJ, 581, 357

Kraus, A. L., Andrews, S. M., Bowler, B. P., et al. 2015, ApJ, 798, L23

Kretke, K. A., Lin, D. N. C. 2007, ApJ, 664, L55

Krist, J. E., Stapelfeldt, K. R., Hester, J. J., et al. 2008, AJ, 136, 1980

Kuhn, J. R., Potter, D., & Parise, B. 2001, ApJ, 553, L189

Lee, E. J., Chiang, E., & Ormel, C. W. 2014, ApJ, 797, 95

Lissauer, J. J., Dawson, R. I., & Tremaine, S. 2014, Nature, 513, 336

Lissauer, J. J., Fabrycky, D. C., Ford, E. B., et al. 2011, Nature, 470, 53

Lizano, S., Torrelles, J. M. 1995, eds., RMACS, 1

Looney, L. W., Mundy, G., & Welch, W. J. 2000, ApJ, 529, 477

Lugo, J., Lizano, S., & Garay, G. 2004, ApJ, 614, 807

Lynden-Bell, D., & Pringle, J. E. 1974, MNRAS, 168, 603

Maaskant, K. M., Honda, M., Waters, L. B. F. M., et al. 2013, A&A, 555, A64

Macías, E., Anglada, G., Osorio, M., et al. 2016, ApJ, 829, 1

Mann, R. K., Di Francesco, J., Johnstone, D., et al. 2014, ApJ, 784, 82

Manoj, P., Bhatt, H. C., Maheswar, G., & Muneer, S. 2006, ApJ, 653, 657

Mathis, J. S., Rumpl, W., & Nordsieck, K. H. 1977, ApJ, 217, 425

McClure, M. K., D'Alessio, P., Calvet, N., et al. 2013, ApJ, 775, 114

McClure, M. K., Espaillat, C., Calvet, N., et al. 2015, ApJ, 799, 162

McClure, M. K., Forrest, W. J., Sargent, B. A., et al. 2008, ApJ, 683, L187

Meeus, G., Pinte, C., Woitke, P., et al. 2010, A&A, 518, L124

Mendoza V., E. E. 1966, ApJ, 143, 1010

Miyake, K., & Nakagawa, Y. 1993, Icarus, 106, 20

Momose, M., Morita, A., Fukagawa, M., et al. 2015, PASJ, 67, 83

Mumma, M. J., & Charnley, S. B. 2011, ARA&A, 49, 471

Nagel, E., D'Alessio, P., Calvet, N., Espaillat, C., Trinidad, M.A. 2013, RMAA, 49, 43

Najita, J. R., Doppmann, G. W., Bitner, M. A., Richter, M. J., et al. 2009, ApJ, 697, 957

Ogihara, M., Morbidelli, A., & Guillot, T. 2015, A&A, 578, A36

Okuzumi, S., Momose, M., Sirono, S., Kobayashi, H., & Tanaka, H. 2016, ApJ, 821, 82

Ormel, C. W., Paszun, D., Dominik, C., & Tielens, G. G. M. 2009, A&A, 502, 845

Osorio, M., Anglada, G., Carrasco-González, C., et al. 2014, IAU Symposium, 299, 145

Osorio, M., Anglada, G., Carrasco-González, C., et al. 2014, ApJ, 791, L36

Osorio, M., Fuente, A., Anglada, G., et al. 2015, in Spanish SKA White Book, ed. M. Pérez-Torres et al., 153

Osorio, M., Macías, E., Anglada, G., et al. 2016, ApJ, 825, L10

Owen, J. E., Clarke, C. J., & Ercolano, B. 2012, MNRAS, 422, 1880

Owen, J. E., & Clarke, C. J. 2012, MNRAS, 426, L96

Owen, J. E., Ercolano, B., Clarke, C. J. 2011, MNRAS, 412, 13

Owen, J. E., Ercolano, B., Clarke, C. J., & Alexander, R. D. 2010, MNRAS, 401, 1415

Owen, J. E., Scaife, A. M. M., Ercolano, B. 2013, MNRAS, 434, 3378

Papaloizou, J. C. B., Nelson, R. P., Kley, W., Masset, F. S., & Artymowicz, P. 2007, in Protostars and Planets V, ed. B. Reipurth, D. Jewitt, & K. Keil (Tucson, AZ: Univ. Arizona Press), 655

Papaloizou, J., & Pringle, J. E. 1977, MNRAS, 181, 441

Pascucci, I., Gorti, U., & Hollenbach, D. 2012 ApJ, 751, L42

Pascucci, I., Ricci, L., Gorti, U., et al. 2014 ApJ, 795, 1

Pascucci, I., & Sterzik, M. 2009 ApJ, 702, 724

Patel, N. A., Curiel, S., Sridharan, T. K., et al. 2005, Nature, 437, 109

Pecaut, M. J., & Mamajek, E. E. 2013, ApJS, 208, 9

Pérez, L. M., Carpenter, J. M., Chandler, C. J., et al. 2012, ApJ, 760, L17

Pérez, L. M., Chandler, C. J., Isella, A., et al. 2015, ApJ, 813, 41

Pérez, L. M., Isella, A., Carpenter, J. M., & Chandler, C. J. 2014, ApJ, 783, L13

Picogna, G., & Kley, W. 2015 A&A, 584, A110

Piétu, V., Guilloteau, S., Di Folco, E., Dutrey, A., & Boehler, Y. 2014, A&A, 564, A95

Pineda, J. ÊE., Quanz, S. P., Meru, F., et al. 2014, ApJ, 788, L34

Pinilla, P., Benisty, M., & Birnstiel, T. 2012, A&A, 545, A81

Pinilla, P., Birnstiel, T., Ricci, L., et al. 2012, A&A, 538, A114

Quanz, S. P., Avenhaus, H.,Buenzli, E., et al. 2013, ApJ,766, L2

Quanz, S. P., Schmid, H. M, Geissler, K., et al. 2011, ApJ,738, 23

Raman, A., Lisanti, m:, Wilner, D. J., et al. 2006, AJ, 131, 2290

Rau, U., Cornwell, T. J. 2011, A&A, 532, 71

Reggiani, M., Quanz, S. P., Meyer, M. R., et al. 2014, ApJ, 792, L23

Rodmann, J., Henning, T., Chandler, C. J., et al. 2006, A&A, 446, 211

Rodríguez, L. F., Cantó, J., Torrelles, J. M., Gómez, J. F., Ho, P. T. P. 1992, ApJ, 393, 29

Rodríguez, L. F., D'Alessio, P., Wilner, D. J., et al. 1998, Nature, 395, 355

Rodríguez, L. F., Torrelles, J. M., Anglada, G., Reipurth, B. 2014, AJ, 136, 1852

Rodríguez, L. F., Zapata, L. A., Dzib, S. A., et al. 2014, ApJ, 793, L21

Ros, K., & Johansen, A. 2013, A&A, 552, A137

Sacco, G. G., Flaccomio, E., Pascucci, I., et al. 2012, ApJ, 747, 142

Sallum, S., Follette, K. B., Eisner, J. A., et al. 2015, Nature, 527, 342

Salyk, C., Herczeg, G. J., Brown, J. M., et al. 2013, ApJ, 769, 21

Sandell, G., & Aspin, C. 1998, A&A, 333, 1016

Sandell, G., Weintraub, D. A., & Hamidouche, M. 2011, ApJ, 727, 26

Sargent, A. L., Beckwith, S V. W. 1991, ApJ, 382, L31

Shakura, N. I., & Sunyaev, R. A. 1973, A&A, 24, 337

Siess, L., Dufour, E., & Forestini, M. 2000, A&A, 358, 593

Strom, S. E. 1985, in Protostars and Planets II, ed. D. C. Black & M. S. Matthews (Tucson, AZ: Univ. Arizona Press), 17

Strom, K. M., Strom, S. E., Edwards, S., Cabrit, S., & Skrutskie, M. F. 1989, AJ, 97, 1451

Suzuki, T. K., & Inutsuka, S.-i. 2014, ApJ, 784, 121

Suzuki, T. K., Muto, T., & Inutsuka, S.-i. 2010, ApJ, 718, 1289

Swift, J. J., Johnson, J. A., Morton, T. D., et al. 2013, ApJ, 764, 105

Testi, L., Birnstiel, T., Ricci, L., et al. 2014, in Protostars and Planets VI, ed. H. Beuther et al. (Tucson, AZ: Univ. Arizona Press), 339

Thalmann, C., Mulders, G. D., Janson, M., et al. 2015, ApJ, 808, L41

Torrelles, J M., Rodríguez, L. F., Canto, J., et al. 1983, ApJ, 274, 214

Torres, R. M., Loinard, L., Mioduszewski, A. J., & Rodríguez, L. F. 2009, ApJ, 698, 242

Turner, N. J., Carballido, A., & Sano, T. 2010, ApJ, 708, 188

van der Marel, N., van Dishoeck, E. F., Bruderer, S., et al. 2016, A&A, 585, A58

van der Marel, N., van Dishoeck, E. F., Bruderer, S., et al. 2013, Science, 340, 1199

van der Marel, N., van Dishoeck, E. F., Bruderer, S., Pérez, L., & Isella, A. 2015, A&A, 579, A106

Wagner, K. R., Sitko, M. L., Grady, C. A., et al. 2015, ApJ, 798, 94

Weidenschilling, S. J. 1977, MNRAS, 180, 57

Weintraub, D. A., Sandell, G., Duncan, W. D. 1989, ApJ, 340, L69

Whipple, F. L. 1972 in From Plasma to Planet, ed. A. Evlius (New York, NY: Wiley), 211

White, R. J., & Ghez, A. M. 2001, ApJ, 556, 265

Williams, J. P., Cieza, L. A. 2011, A&A, 49, 67

Wuchterl, G., Guillot, T., & Lissauer, J. J. 2000, in Protostars and Planets IV, ed. V. Mannings, A. P. Boss, & S. S. Russell (Tucson, AZ: Univ. Arizona Press), 1081

Zapata, L. A., Galván-Madrid, R., Carrasco-González, C., et al. 2015, ApJ, 811, L4

Zhang, K., Blake, G. A., & Bergin, E. A. 2015, ApJ, 806, L7

Zhu, Z., Nelson, R. P., Dong, R., Espaillat, C., & Hartmann, L. 2012, ApJ, 755, 6

Zhu, Z., Nelson, R. P., Hartmann, L., Espaillat, C., & Calvet, N. 2011, ApJ, 729, 47

Zhu, Z., & Stone, J. M. 2014, ApJ, 795, 53